ISSN 1688-2784

UNIVERSIDAD DE LA REPÚBLICA
FACULTAD DE INGENIERÍA

Wearable Estimation of Central Aortic Blood Pressure

TESIS PRESENTADA A LA FACULTAD DE INGENIERÍA DE LA UNIVERSIDAD DE LA REPÚBLICA POR

Germán Andrés Fierro Musso

EN CUMPLIMIENTO PARCIAL DE LOS REQUERIMIENTOS
PARA LA OBTENCIÓN DEL TÍTULO DE
DOCTOR EN INGENIERÍA ELÉCTRICA.

DIRECTORES DE TESIS

Fernando Silveira	Universidad de la República
Ricardo Armentano	Universidad de la República

TRIBUNAL

Hamilton Klimach	Universidade Federal do Rio Grande do Sul, Brasil
Esteban Pino	Universidad de Concepción, Chile
Agustín Ramírez	Universidad Favaloro, Argentina

DIRECTOR ACADÉMICO

Fernando Silveira	Universidad de la República

Montevideo
23 de Marzo de 2020

Wearable Estimation of Central Aortic Blood Pressure , Germán Andrés Fierro Musso.

ISSN 1688-2784

Esta tesis fue preparada en LaTeX usando la clase iietesis (v1.1).
Contiene un total de 173 páginas.
Tesis defendida el 23 de Marzo de 2020.
`http://iie.fing.edu.uy/`

Summary

Arterial hypertension affects a third of the world's population and is a significant risk factor for cardiovascular disease. Blood pressure (BP) is one of the most relevant parameters used for monitoring of possible hypertension states in patients at risk of cardiovascular disease. Hence, there exists a need for new monitoring solutions, which allow to increase the frequency between BP assessments, but also allow to reduce the level of occlusion in the attempts. Moens-Korteweg equation is among the main principles to estimate BP by dispensing of any inflatable cuff. This principle might lead to an indirect estimation of BP by measuring the time it takes the pressure pulse to propagate between two pre-established vascular points, accordingly the pulse transit time (PTT) method. This thesis proposes a wearable PTT-based method to estimate central aortic BP (CABP) and, the main milestones of this work included: proof of concept of the proposed method (pilot work), the development of a wearable device (including two stages of validation), the proposition of a miniaturized version (integrated circuit) of the analog front-end of the wearable hardware, and, the development of a novel PTT-based model (PTTBM, i.e., the mathematical relationship between measured variables and estimated BP) suitable for the proposed wearable methodology to estimate BP. The main contributions found at each milestone are presented.

One of the contributions of this thesis is the use of the PTT-principle for estimating CABP instead of the peripheral BP (PBP) (as typically used in the literature). The pilot work showed the feasibility of CABP estimation from the PTT principle by using electrocardiogram (ECG) and ballistocardiogram (BCG) recordings from off-the-shelf equipment. Results showed that CABP was more correlated with the proposed methodology in comparison to all PBP variables assessed; confirming our hypothesis that the CABP is the most suitable parameter to collate through the time elapsed from ECG R-wave to the BCG J-wave. That is, considered featured time (RJ-interval) includes the time of a pulse pressure propagating at an aortic district. Bland-Altman plots showed an almost zero mean error ($|\mu| < 0.02$mmHg) and bounded standard deviation $\sigma < 5$mmHg for all systolic and mean central BP readings.

Pilot work provided a landmark in order to develop a compact device that allows the integration of wireless blood pressure monitoring into a wearable system. Another contribution of this thesis is the proposition of a wearable device for PTT-computing by also including design considerations for the signal conditioning chains for ECG and BCG signals. The proposed design procedure takes

care of minimizing the impact of spurious delays between physiological signals, which eventually degrade the PTT computation. Further, such a procedure could be suitable for any PTT-acquisition. Filtering with low and controlled delay is required for this biomedical application, and proposed conditioning chains provide less than 2ms group-delay, showing the effectiveness of the proposed approach. In order to provide the methodology with higher autonomy and integration, a highly miniaturized implementation of the filtering approach was also proposed. It includes the design of proposed architectures in CMOS technology to implement the particular low-delay filtering at reduced bandwidth featuring ultra-low-power characteristics. Results show that less than 2ms delay for the ECG QRS-complex can be achieved with a total current consumption of $I_{DD} = 2.1nA$ at $V_{DD} = 1.2V$ of power supply. Such development meant another significant contribution of this work in the conception of highly autonomous wearable devices for PTT acquisition.

The first stage of validations on the wearable CABP estimation showed that, when considering data from one volunteer, results achieved with off-the-shelf equipment could be replicated by using a proposed wearable device, and the method could be further validated by using the wearable version. Additionally, CABP estimation from the proposed wearable device could be feasible by using three feature times (FTs) as CABP surrogates; that is, RI, RJ, and IJ intervals (from ECG and BCG wearable recordings). The first validation of the method also showed that CABP could be accurately predicted by the proposed methodology when in the order of daily calibrations are performed. The second stage of validations involved a study with a group of volunteers, and new alternatives were explored (twenty-seven: nine PTTBMs along the three FTs) for the CABP estimation. We found that CABP could be accurately estimated (inside AAMI requirements) through the presented methodology by using four of the explored alternatives, whereas the RI interval, an FT lacking any PTT assessment, emerged as the best surrogate for the CABP estimation. Hence, a principle different from the traditional PTT-based method arises as a more advantageous method for the CABP estimation in the light of evidence reported in this validation, and, to our knowledge, this is the first time that CABP has been successfully estimated from a wearable device.

The final significant contribution of this thesis meant the last chain-link in the process to achieve an utterly original method to estimate CABP. A novel PTTBM to estimate CABP is proposed, which uses a flow-driven two-element Windkesel network constructed from FTs extracted from the wearable recordings. When classic PTTBMs are applied, the fitting of parameters often leads to values without a physiological basis. Opposite to that in the proposed PTTBM, the parameters have a clear physiological meaning, and the parameter fitting led to values that are consistent with this meaning and more stable throughout calibrations.

In conclusion, this thesis introduces a novel device that exploits an alternative and indirect method for CABP estimation. Variants of the principle used, accordingly, PTT method, have been previously explored to estimate PBP but not for central aortic BP. Additionally, the device was designed to be wearable; that is, it is attached to the clothes, causing low discomfort for the user during the measurement, thus, allowing continuous and ambulatory monitoring of aor-

tic pressure. The developed wearable system, validated in a series of volunteers, showed promising results towards the continuous CABP monitoring.

This page was intentionally left blank.

Resumen

Se estima que casi un tercio de la población adulta mundial sufre de algún grado de hipertensión, siendo esto un factor de riesgo significativo para la enfermedad cardiovascular. La presión arterial (PA) es el parámetro utilizado para evaluar estos posibles estados de hipertensión; actualmente existe una necesidad de generación de nuevas tecnologías que permitan aumentar la frecuencia entre medidas de PA, pero al mismo tiempo de reducir el nivel de oclusión de éstas (técnicas aceptadas están mayoritariamente basadas en la oclusión y son de acceso limitado). El modelo Moens-Korteweg podría proveer los argumentos para la creación de nuevas técnicas para estimar la PA prescindiendo de cualquier brazalete inflable. Más específicamente, podría obtenerse una estimación indirecta de la PA a través de la medición del tiempo que tarda el pulso de presión en propagarse entre dos puntos vasculares predefinidos, método conocido como tiempo de tránsito del pulso (PTT). En la presente tesis se desarrolló un dispositivo vestible que explota este método alternativo e indirecto para la estimación de la PA pero a nivel central, es decir, busca estimar la PA en la aorta (CABP), la principal arteria de la red vascular. Para ello, los principales desarrollos de este trabajo incluyeron: prueba de concepto del método propuesto basado en PTT para estimar CABP, el desarrollo de un dispositivo vestible (incluyendo dos etapas de validaciones para la estimación de la PA), la propuesta de un circuito integrado para el hardware vestible y el desarrollo de un nuevo modelo para la estimación de la PA (PTTBM, es decir, la relación matemática que vincula las variables medidas con el hardware diseñado y la estimación de la PA). A continuación se presentan las principales contribuciones resultantes de cada frente de trabajo.

Una de las contribuciones de esta tesis es el uso del principio PTT para estimar CABP en lugar de la BP periférica (PBP) (como se usa típicamente en la literatura). La prueba de concepto mostró la viabilidad de la estimación de CABP a partir del principio PTT mediante la adquisición de señales electrocardiograma (ECG) y balistocardiograma (BCG) utilizando equipos comerciales. Los resultados mostraron que CABP estaba más correlacionado con la metodología propuesta en comparación con todas las variables de PBP evaluadas; confirmando nuestra hipótesis de que la CABP sería la variable más adecuada para estimar a partir del tiempo transcurrido desde la onda R del ECG hasta la onda J del BCG. Es decir, el tiempo considerado (intervalo RJ) incluye un tiempo de propagación del pulso de presión a través de un segmento aórtico. Las gráficas de Bland-Altman mostraron un error medio casi nulo ($|\mu| < 0.02$mmHg) y una precisión $\sigma < 5$mmHg para las variables de presión sistólica y media centrales.

La prueba de concepto proporcionó un hito para desarrollar un dispositivo vestible apuntando a la monitorización inalámbrica de la presión arterial en un sistema imperceptible para el usuario. Otra contribución de esta tesis es la propuesta de este dispositivo vestible para la adquisición de la PTT. El desarrollo incluye consideraciones de instrumentación necesarias para el correcto acondicionamiento de las señales ECG y BCG, de las cuales se obtiene la PTT. En particular, el procedimiento de diseño propuesto busca minimizar el impacto de los retrasos espurios entre las señales fisiológicas, que eventualmente degradan la computación de la PTT. Además, dicho procedimiento podría ser aprovechado por otros desarrolladores del método sin importar las definiciones de PTT que éstos usen. La limitación de banda con bajo retardo es necesario para esta aplicación biomédica, y el hardware de acondicionamiento propuesto proporciona menos de 2 ms de retraso en las señales (ECG y BCG) mientras consigue limitar sus bandas a decenas de Hz, lo que muestra la efectividad de la metodología propuesta. Adicionalmente, con el fin de proporcionar a la metodología de una mayor autonomía e integración, se propone una implementación altamente miniaturizada de la sección de filtrado con bajo retraso. Se incluye el diseño de nuevas topologías propuestas en tecnología *CMOS* para implementar el particular filtro de bajo retraso con reducido ancho de banda, y con características de ultra bajo consumo de potencia. El diseño integrado consigue obtener resultados similares al obtenido anteriormente (con componentes discretos) alcanzando un retraso de menos de 2 ms para el complejo QRS del ECG, pero con un consumo de $I_{DD} = 2.1\ nA$ a un $V_{DD} = 1.2\ V$. Tal desarrollo significó otra contribución de este trabajo en el área de circuitos altamente autónomos para instrumentación biomédica.

La primera etapa de validaciones en la estimación vestible de la CABP se basó en experimentaciones con un voluntario, mostrando que, la estimación vestible podría alcanzar los mismos resultados que los alcanzados utilizando equipos de investigación, permitiendo así avanzar en la validación del método propuesto utilizando el equipamiento vestible diseñado. Además de esto, se encontró que la estimación de CABP a partir del dispositivo vestible podría ser factible utilizando varios tiempos característicos (FT) extraídos de las señales vestibles ECG y BCG (intervalos RI, RJ e IJ) junto con un popular PTTBM. La primera validación del método también arrojó que la metodología propuesta podría estimar con precisión la CABP cuando el tiempo entre calibraciones es del orden de un día. La segunda etapa de validación implicó un estudio con un grupo de voluntarios, nuevas alternativas se exploraron esta vez (veintisiete: nueve PTTBM con tres FT) para la estimación de CABP. Descubrimos que CABP podría estimarse con precisión (dentro de los requisitos de AAMI) a través de la metodología presentada mediante el uso de cuatro de las alternativas exploradas, mientras que el intervalo RI, siendo un FT que a priori no tiene ninguna vinculación con un PTT, surge como el mejor estimador de la CABP. Se concluye entonces, que un principio diferente del método tradicional basado en PTT podría ser más ventajoso para la estimación de CABP a la luz de la evidencia encontrada en esta validación y, adicionalmente, a nuestro entender, esta es la primera vez que CABP se estima con éxito a partir de un dispositivo vestible.

La contribución final de esta tesis significó el último eslabón de la cadena en el proceso de lograr un método completamente original para estimar CABP de punta a punta. Se propone un nuevo PTTBM para estimar CABP, éste es basado en una red Windkesel de dos elementos bajo una excitación de flujo. Estos elementos del PTTBM son construidos a partir de cantidades extraídas a través de procesamiento de las señales vestibles ECG y BCG. Cuando se aplican los PTTBM clásicos, el ajuste de sus parámetros (en calibración) a menudo conducen a valores sin base fisiológica, mostrando a su vez, una dispersión en sus valores a lo largo de distintas calibraciones que podrían ser inaceptables en la práctica. En contraposición, los parámetros del PTTBM propuesto convergen a cantidades con significado fisiológico claro y estable a lo largo de las calibraciones.

En conclusión, esta tesis presenta un dispositivo novedoso que explota un método alternativo e indirecto para la estimación de CABP. El método propuesto es basado en la metodología de PTT, que si bien ha sido previamente explotado para estimar PBP, no se ha dirigido éste hacia el monitoreo vestible de la PA aórtica central. En este marco se desarrolla un dispositivo vestible, causando baja molestia en el usuario durante las mediciones, lo que permitiría un monitoreo continuo y ambulatorio real de la presión aórtica central. El sistema vestible desarrollado, validado en una serie de voluntarios, ha mostrado resultados prometedores hacia el monitoreo continuo de CABP.

Contents

This page was intentionally left blank.

Chapter 1

Introduction

"Mi vecino se tomaba la presión a diario en la emergencia del barrio, sus valores de presión (perférica) siempre estaban controlados por la medicación. Esa mañana, mientras se peinaba frente al espejo, con el pelo mojado y escuchando al mago, fue la última vez que se vio. Tuvo una muerte súbita."

Hypertension, the clinical term for elevated blood pressure (BP), it is also commonly referred to as the silent killer. It seldom causes symptoms in the early stages, making hypertensive people often unaware that they are until it is too late. It is estimated that almost a third of the world's adult population suffers from some degree of hypertension [1], and the battle against it is one of the main challenges facing health systems today. While it is a significant risk factor for cardiovascular or kidney disease, which ends up being among the leading causes of death around the world; hypertension is a risk factor that can be reasonably modifiable with changes in lifestyle and medication. However, the problem is that hypertension rarely causes initial symptoms, and chances of early stages of treatment for the disease are often lost. The efforts of medicine are increasingly focused on the prevention, early detection, and treatment of this disease. In this context, BP is one of the most relevant parameters used for continuous monitoring of possible hypertension states. Thus, the emergence of new technologies that allow continuous and ambulatory BP monitoring are absolutely valuable.

Another issue to be addressed is the monitoring of cardiovascular health at home with inexpensive and connected technologies, this would provide better control in the management of hypertension by providing instant feedback-controlled therapies, which in turn may reduce the burden on the healthcare system. The critical research and development in this area arise through the so-called m-health, which harnesses the potential and broad penetration in the society of mobile devices with high computing power (smartphones and tablets). In order to make this possible, it is necessary to contribute to the generation of technology to make ambulatory health monitoring using wearable devices.

Current techniques for non-invasive BP monitoring are based on the use of an inflatable cuff around a limb, typically the upper arm. While the health community widely uses these cuff-based techniques, they have some drawbacks: require medical assistance, cause discomfort/injury, they are intermittent, and only allow obtaining peripheral BP (PBP), that is, where the cuff is placed. On the one hand, these reasons evidence the incapability of current BP monitoring techniques for ambulatory and continuous monitoring on a generalized basis. Hence impeding, the proper monitoring during daily life activities, and the possibility of the launching of short-term BP regulation mechanisms. On the other hand, obtaining the central blood pressure (at the level of the aorta), could allow us to better estimate the incidence on the organs most vulnerable to hypertension (brain, heart, kidneys). Consequently, it is expected that central aortic blood pressure (CABP) and PBP predict cardiovascular events and mortality differently [2] [3] [4].

Some current limitations of BP home monitoring must be addressed in order to defeat hypertension. Mainly, there is a need for devices with high portability, capable of being used throughout the day (wearables); and, provided with the highest capability for predicting cardiovascular events (access to central hemodynamic variables represents a significant contribution to this aspect). Additionally, such devices should be implemented with inexpensive and connected technologies that lead to better control in the management of hypertension. This thesis contributes to the generation of new technologies for monitoring BP at home by taking into account the concerns above.

1.1 Scope

The scope of the thesis is the creation of a electronic system able to monitor the arterial blood pressure. Variants of the principle used (the measurement of the transit time of pressure pulse in the arterial network) have been explored to estimate peripheral BP but not for central BP. The proposed approach implies reconsidering whether the PTT-based models available in the literature (ie, the mathematical relationship between measured variables and estimated BP) are appropriate or not. Additionally, the device was designed to be wearable, that is, that allows it to be attached to clothing, being comfortable during measurements, thus allowing continuous and ambulatory monitoring. The developed wearable system showed that the proposed methodology might lead to the ambulatory and continuous BP monitoring at aortic districts. This thesis thus involved in overcoming different obstacles which lead in the following significant contributions:

- Proposal of a methodology, validated with tests with volunteers, for the estimation of central BP from the ballistocardiogram and electrocardiogram waveforms.
- Exploration of the state-of-the-art for blood pressure PTT-based models, derived from the pulse transit time method, and, its adaptation to the proposed methodology.

- Proposal for a new PTT-based model for the wearable estimation of the central BP based firmly on the physical modeling of the central circulatory system.
- Creation of a wearable platform, including the design of its hardware and software, for the acquisition of physiological signals, proposing new design criteria for better measurement of pulse transit time.
- Design of an integrated circuit that implements a miniaturized version of core blocks of the analog interface suitable for the wearable system which implements the proposed criteria but at an integrated level.

1.2 Architecture

Chapter 2

Introduces some previous information needed for the understanding of this document. The chapter begins with basic concepts about the blood pressure (BP) and some physiological mechanisms used for the development of this work, such as the pulse wave velocity and the pre-ejection. Then, conventional (mainly cuff-based) techniques used for the non-invasive assessment of the (peripheral) blood pressure and central aortic blood pressure are presented. Finally, the pulse transit time (PTT) method is introduced as a promising approach for estimating BP from an ambulatory perspective, particularly towards the creation of a truly wearable device, which is the primary goal of this thesis.

Chapter 3

The feasibility of the central aortic blood pressure estimation from the transit time method is studied. The scope of the chapter is to show the initial validation of a proposed cuff-less method to estimate CABP. Validation of the proposed method was performed with a small sample of healthy volunteers during strength maneuvers, and, by using off-the-shelf equipment. Experimental data showed promissory results for monitoring CABP via PTT, which might lead to the creation of a continuous BP monitoring device. Part of the material presented in this chapter was published in G. Fierro, F. Silveira, and R. Armentano. *Central blood pressure monitoring method oriented to wearable devices.* Health and Technology, vol 6, pages 197–204, 2016. Springer.

Chapter 4

The chapter presents the proposed approach for signal conditioning of a PTT-based monitoring device. The method is suitable for a low power wearable implementation, which also takes into consideration the phase-shifting impact. The concepts shown in the chapter include design considerations for hardware and software sections of the proposed wearable platform, which can be applied in the conception of any PTT-based wearable device. A summary of the material presented in this chapter was published in G. Fierro, F. Silveira, and R. Armentano. *Low group delay signal conditioning for wearable central blood pressure monitoring device.* In 2017 39th AnnualInternational Conference of the IEEE Engineering in Medicine and Biology Society (EMBC), pages 3285–3288, July 2017.

Chapter 5

Presents a miniaturized version of an analog front-end suitable for a PTT-based wearable device. The chapter reviews the top level of the proposed architecture, while the filtering section is further detailed. Notably, the ultra-low-power integrated filter design is shown. The proposed filter features a low phase shift at the QRS band and presents tuning capabilities. Part of the material presented in this chapter was published in G. Fierro and F. Silveira, *Ultra Low Power Tunable Filter for a Low Phase Shift on Electrocardiogram QRS-Complex Acquisition.* In 2018 31st Symposium on Integrated Circuits and Systems Design (SBCCI), Bento Goncalves, pages 1-5, August 2018.

Chapter 6

Includes the first set of validations of the proposed method to estimate CABP by using the designed wearable device. The chapter content aims to evaluate whether a proposed wearable device is capable of achieving similar feasibility results on CABP estimation as obtained with off-the-shelf equipment (Chapter 2). The study also aims to characterize the scope of this method to estimate CABP regarding to calibration interval (i.e., the period after a calibration procedure in which the method is capable of accurately tracking CABP) and prediction capability (two degree of validations) perspectives. The material presented in this chapter was accepted after the revision in a peer-reviewed conference. G. Fierro, R. Armentano and F. Silveira. *Wearable Estimation of Central Aortic Blood Pressure: Feasibility Study.* In XXII CONGRESO ARGENTINO DE BIOINGENIERÍA - SABI 2020.

Chapter 7

Presents the final validation in volunteers of the proposed system and methodology. Twenty-seven alternatives (nine blood pressure PTT-based models along three feature times) are explored for the aortic blood pressure estimation from the proposed wearable device. To our knowledge, this is the first time that central aortic blood pressure has been successfully estimated from a wearable device. Part of the material presented in this chapter was published in G. Fierro, R. Armentano. and F. Silveira. *Evaluation of transit time-based models in wearable central aortic blood pressure estimation.* Biomedical Physics & Engineering Express, Volume 6, Number 3. IOP Publishing.

Chapter 8

Proposes an original PTT-based model (PTTBM) that uses Windkessel modeling, particularly by using a flow-driven two-element network constructed from features extracted by the proposed wearable device. The initial validations of the proposed PTT-based model are presented, showing that the proposed PTTBM is promising to resolve some issues observed during the CABP estimation when classic PTTBMs were used. For instance, being the calibration of these PTT-based models, a mathematical process (regressions) between data and PTTBM, fitted parameters in PTTBM might lose their physical meaning (numerically) in order to improve the fitting accuracy. Moreover, such issues might also lead to unacceptable variability in their fitting parameters, even considering within-person and very frequent calibrations (chapter 6). These issues worsen even more because of the expected fluctuations in PTT due to the within-person variability [5]. Increasing the physical constraints (at the calibration stage or for the particular PTTBM) might help to improve the fitting quality. Proposed physical-constrained PTTBM showed promissory results in mentioned calibration issues. This final contribution meant the last chain-link in order to come by an utterly original method to estimate CABP.

Chapter 9

Draws the conclusions of this thesis.

Chapter 2

Background

Summary

This chapter introduces some previous information needed for the understanding of this document. The chapter begins with some basic concepts about the blood pressure (BP) and, being among the main physiological mechanisms used in this document, the pulse wave propagation phenomena, and the heart (pre-) ejection are presented in section 2.1. Noteworthy, far from being a self-contained document, the thesis still requires the reader a basic comprehension of the circulatory system physiology. Then in section 2.3, some of the conventional cuff-based techniques used for assessing (the peripheral) blood pressure are presented. The importance of the assessment of central aortic blood pressure (CABP) along with some of the techniques available for its non-invasive assessment are included, notably, AtCor Medical - SphygmoCor XCEL is highlighted as the cuff-based device used for providing CABP assessments along the experiments included in this thesis. Then, the pulse transit time method, which is the principal cuff-less approach used for estimating CABP in this thesis, along with the ballistocardiogram signal, which re-emerges as a valuable physiological signal for the method, are presented in section 2.4. Finally, the conception of a wearable device for estimating CABP from the PTT-method is presented in section 2.5.

2.1 Blood Pressure

Blood pressure (BP) is the force per unit of area exerted against the internal surface of the arterial vessels. Heart work over the blood generates a longitudinal pressure gradient along the blood vessel network, which is responsible for the conduction of the bloodstream. Additionally, the pulsating nature of heart-pumping is responsible for the also pulsating blood pressure waveform at a particular vascular point. Typically, BP is measured in millimetres of mercury (mmHg), and it is characterized by its maximum and minimum values (considering at least a heart-beat), such variables are known as systolic BP and diastolic BP, respectively. Thus, the blood pressure waveform (at a particular point of the arterial network) is ranging between these two variables.

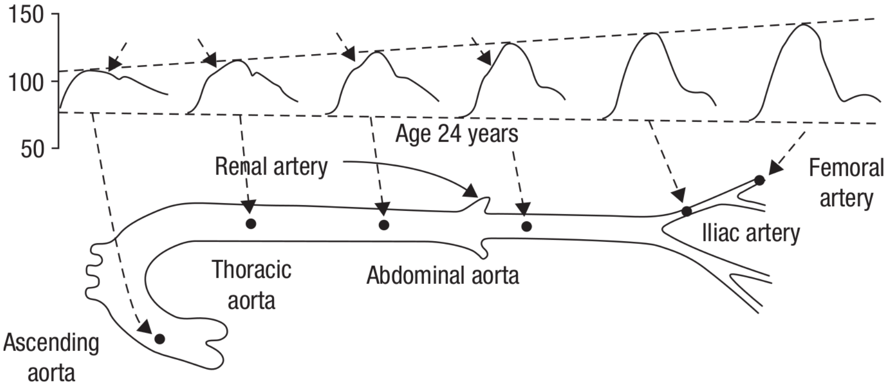

Figure 2.1: Propagation and amplification of pulse pressure pulses along the aorta [6].

On the other hand, being the blood an in-compressible fluid confined at a non-rigid tube (arteries), blood volume displacement is based on the propagation of the pulse pressure waveform across the arterial three. The pulse pressure traveling wave pushes the blood at each heartbeat leading to a circulatory system, local pulse propagation is further showed in section 2.1.2. Otherwise, the propagated BP waveform, in turn, suffers a distortion and amplification effect [7] as the traveling wave reaches peripheral districts at the vascular network (fig. 2.1). Such effect occurs mainly due to the increase of the arterial impedance (arterial section decreases), increased stiffness, and the eventual pulse wave reflections superimposed near the systolic section of the BP waveform [7]. In the order of 75% of amplification could be expected between the ascending aorta to the femoral arteries in young, healthy adults [6]. Even though systolic BP is more affected by wave reflection effect than diastolic reading [6], it is expected a discrepancy between both BP variables when assessed at central aortic or at the peripheral arteries, the latter, where BP is typically assessed (brachial, humeral, radial). This thesis faces the problem of the central aortic BP estimation (i.e., the BP at the aortic root, that is, where the aorta, the main arterial vessel begins near the heart). Therefore, when discrimination is needed, this document uses the central aortic BP from the peripheral BP by using the notation CABP and PBP, respectively.

2.1.1 Expected ranges and values

Figure 2.2 shows a simultaneous assessment of the CABP and PBP (at brachial artery) waveforms. Real pulses confirm the fact that both pulses range differently at each particular section of the vascular tree. That is, CABP ranges between systolic = 108 mmHg and diastolic = 77 mmHg whereas PBP between systolic = 125 mmHg and diastolic = 76 mmHg. Leading to 58% of pulse amplification between the aoric root to the brachial artery in this example. Noteworthy, reference values for screening hypertension at variables systolic and diastolic may be different if referring CABP or PBP.

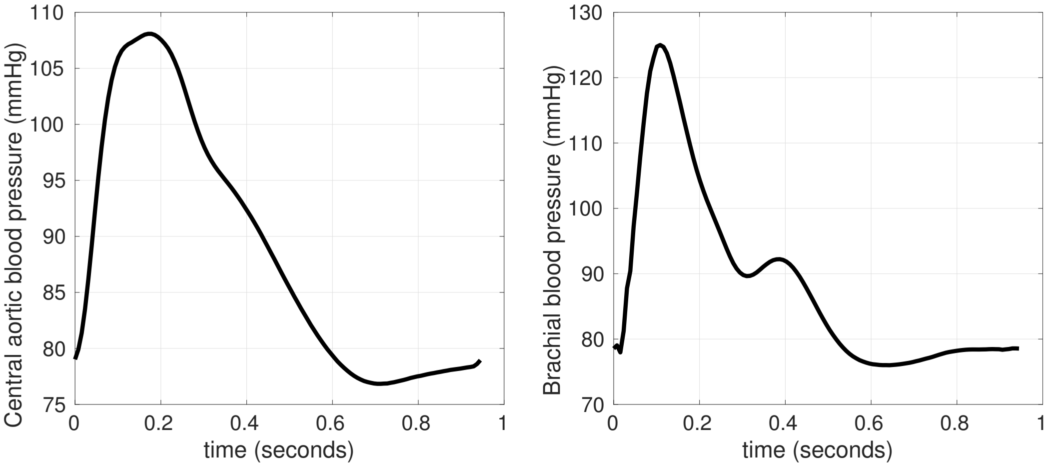

(a) CABP

(b) PBP

Figure 2.2: Central aortic blood pressure (CABP) and peripheral blood pressure (PBP) waveform acquired simultaneously on the same subject. Amplification and distortion effects are noticeable for the pulse pressures from the aortic root to the brachial artery.

Other standard variables that can be found for characterizing the blood pressure waveform are the mean BP and the pulse pressure (PP). Mean blood pressure refers to the average value of the pressure waveform considering a cardiac cycle interval, and PP is the peak-to-peak value of the waveform, that is, PP = systolic-diastolic.

2.1.2 Pressure wave propagation

Pulse propagation phenomena is among the central physiological effects exploited for the development of this thesis, some related elements are presented here.

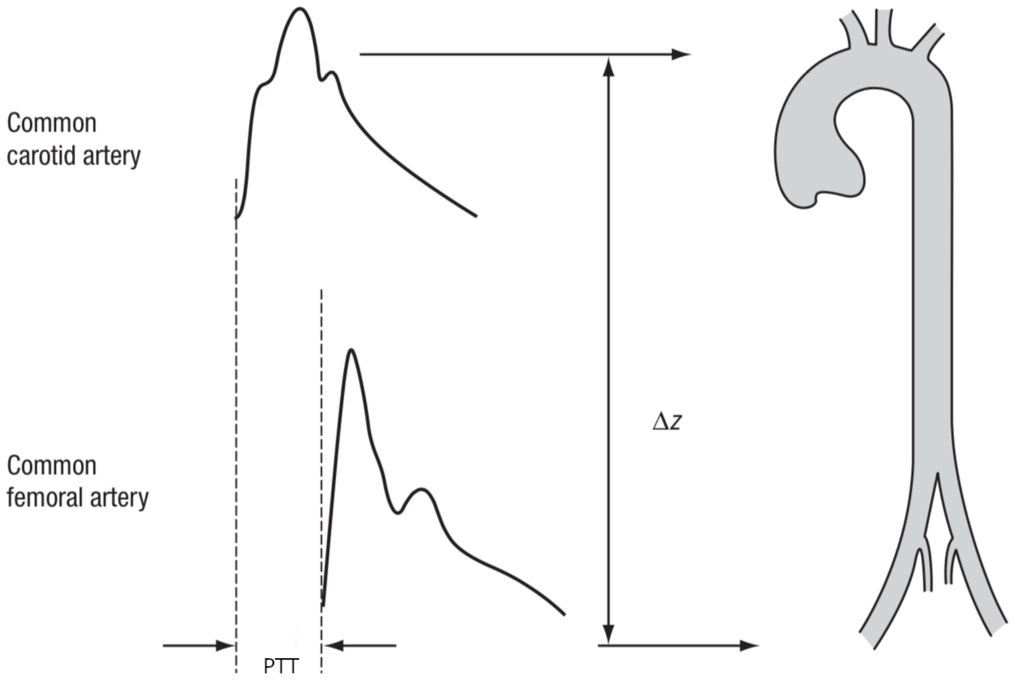

Figure 2.3: Pulse pressure propagation along the aorta. Delay between two pulses at different arterial locations is known as pulse transit time (PTT). The figure summarizes the method used clinically for assessing non-invasively to the pulse wave velocity (PWV) through $PWV \approx \Delta Z/PTT$ by measuring the pulse pressures at carotid and femoral arteries. PWV is considered the gold standard for the assessment of arterial elastance. Image adapted from [6].

A (new) pressure pulse appears in the aortic root at each cardiac cycle when aortic valve opens at each left ventricular ejection. In the order of 75 mL of blood are pushed out from the ventricle into the aorta at each heart-beat (considering of a healthy adult at normal conditions). Considering a simple description for the propagation phenomena, such entering blood volume rises the pressure at the aorta inlet which is absorbed by the aortic walls due to its distensibility properties. Being the blood an in-compressible fluid confined at such compliant tube, the ejected blood mass pushes in turn the portion at the side, and so on, inducing thus a travelling blood flow along the artery. Such a blood volume displacement undergoes to a local augmented pressure, also travelling, which defines the propagation phenomena of the pulse pressures along the arteries. The pressure exerted of volume displacement can be tangible externally, and many approaches for assessing BP are based on sensing such pulses thought different techniques (see sections 2.2 and 2.3). Additionally, the velocity that pulse pressure travels along the arterial tree is known as the pulse wave velocity (PWV). Fig. 2.3 shows an sketch of two volume displacements wave acquired in two aortic locations, given that pulse propagates at velocity PWV, the foot of the pressure pulse is acquired before the respective foot at a distal aortic location. The time it takes the pressure pulse to propagate along a particular distance in the vascular tree is referred as pulse transit time (PTT). The conception of PTT is central for the development of this thesis, since as it will be shown latter, PTT provides a path for measuring BP.

Pulse propagation model

A simplified model for the pulse pressure propagation described as a travelling wave (eq. 2.1) can be derived by applying classical mechanics over a small volume of blood modelled as a mass [8]. The mass of blood is confined in a elastic tube of cross-sectional area A, and characterized by the (cross-sectional) compliance C_{as} defined as the change in tube cross-sectional area A divided by the change in pressure in the tube pressure P(x,t), or equivalently $C_{as} = \partial A/\partial P$ (Fig. 2.4b) ρ refers to the density of the filling blood.

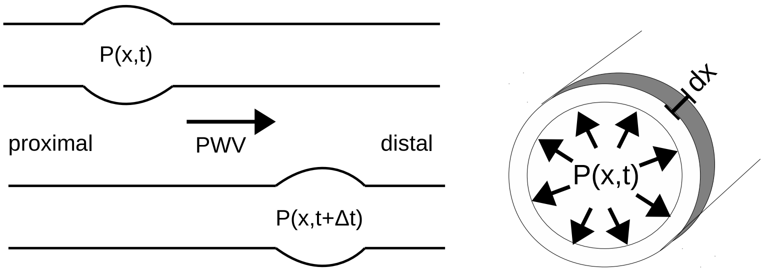

(a) Sketch of the pulse wave velocity (b) Cross-sectional

Figure 2.4: Sketch of the volume displacement propagating at PWV velocity along an elastic artery, and registered at two different time instants. Sketch of the cross-sectional vessel deformation (along radial direction) due to the increased local pressure, illustrating the distensibility effect of the vessel.

$$\frac{\partial^2 P(x,t)}{\partial t^2} = \frac{A}{\rho C_{as}} \frac{\partial^2 P(x,t)}{\partial x^2} \tag{2.1}$$

Therefore

$$PWV = \sqrt{\frac{A}{\rho C_{as}}} \tag{2.2}$$

Equation 2.2 is known as the Bramwell-Hill equation; it describes how the velocity of the pressure pulses propagating along arteries depends on the wall distensibility of the arterial (compliance) segment considered. The more distensible the arterial segment is, the more capable of absorbing the pressure energy by the elastic walls, and consequently, the slower the pressure pulse propagates.

Otherwise, since compliance depends on the artery size, sometimes elastic modulus (E) is preferred to characterize the arterial stiffness of the arteries. Eventually, Laplace's law for a cylindrical tube with a radius r and a thin and incompressible wall thickness h may lead to a relationship between both quantities [9].

$$C_{as} = 2\pi r^3/(Eh), \tag{2.3}$$

Then, by combining 2.2 and 2.3 is found 2.4

$$PWV = \sqrt{\frac{hE}{2r\rho}} \tag{2.4}$$

Equation 2.4 is the well-known Moens-Korteweg equation, which gives an insight into the effect that pulse pressures propagate at high velocity along the artery as it stiffens. The positive relationship between arterial stiffness and pulse wave velocity has been well known since the early 20th century.

2.1.3 Pre-Ejection

Even though the PWV phenomena occur within the arteries, it is essential to show some events that occur (shortly) before the pulse pressure gets the aorta. Figure 2.5 shows some relevant mechanical and electrical quantities within a typical cardiac cycle. These are, left-atrial (LA) and left-ventricular (LV) pressures, aortic pressure (CABP), and electrocardiogram (ECG) superimposed in a temporal diagram. As mentioned previously, pulse pressure onset in the aorta coincides with the onset of the left ventricle ejection, which starts at the aortic valve opening; such an event is thus further investigated.

The principal function of the heart valves is to provide a conduction path for the blood flow only in the direct direction and block the reverse direction flow; when a pressure gradient is established in the direct flow direction, the valves open and the blood flow is established. Therefore, aortic valve activity is found (in Fig. 2.5) when LV pressure exceeds the CABP (opening), or conversely, it closes when LV pressure falls behind CABP. Similarly goes for the mitral valve, LA pressure, and LV, respectively, as can be observed in Fig. 2.5.

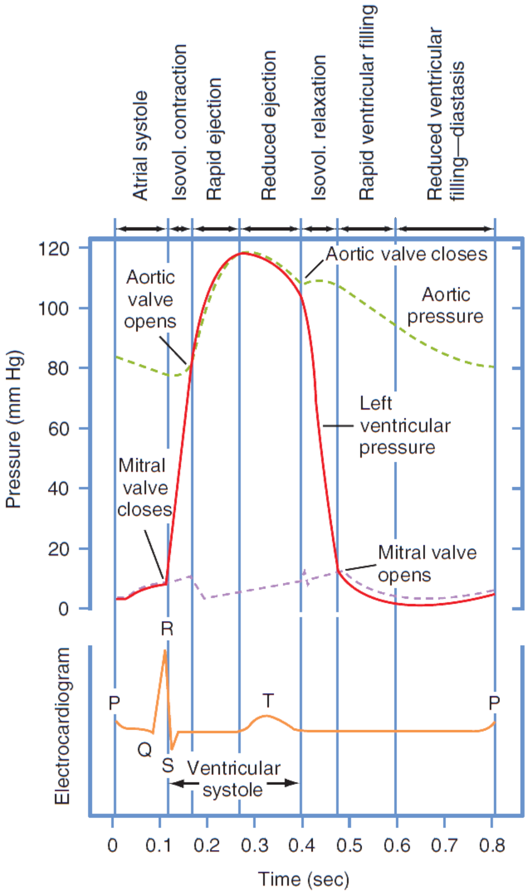

Figure 2.5: Some mechanical and electrical quantities on the heart within a typical cardiac cycle. Left atrial pressure (dashed-pink), left ventricle pressure (continuous-red), central aortic blood pressure (dashed-green) and electrocardiogram (continuous orange) are included. Figure adapted from [10]

Going a little further back in time at diagram, the onset of LV contraction (at constant blood filling volume, i.e., iso-volumetric contraction), which is responsible for the abruptly pressure rising at LV, coincides with the peak of the R-wave of the ECG [10]; since the QRS complex on ECG represents ventricular depolarization. The time elapsed between the start of the isovolumetric contraction and the onset of the LV ejection is known as the pre-ejection period (PEP). PEP is a non-constant delay, which changes rapidly in response to stress, emotion, and physical effort, and also increases with age. Nevertheless, as will be shown, PEP is a very relevant quantity that will be revisited along this thesis.

2.2 Non-invasive peripheral blood pressure assessment

Blood pressure assessment is crucial in order to follow up on possible hypertension states, which constitute a crucial risk factor for health. There exist groups in the society that BP home monitoring is a must-have (rather than a should), and eventually, they would be hugely benefited from new technologies that improve hypertension screening.

It is widely acknowledged that the elderly require more resources from caregivers, and the increased life expectancy change (due to life sciences, health knowledge, and awareness) impacts directly on health care systems. Moreover, the effect would be more pronounced in developing countries than in developed ones since a steeper growth rate of the elderly population is expected in the coming decades, and they are less prepared to cope with aging [11]. Thus, finding mechanisms to reduce this immediate effect is probably one of the most overlooked issues in the current health field around the world. Establishing a suitable home monitoring policy for the elderly attenuates the demand reasonably, mainly by increasing patient independence since, for example, doctor visits are reduced in a continuous monitoring environment, so patient care costs for the family and the state are also reduced.

Figure 2.6: Elder assessing the blood pressure at home with an oscillometric-based device. Image from https://www.microlife.com/technologies/blood-pressure/afib-technology

On the other hand, pregnant women are another group worthy of attention in this context. Hypertensive states in pregnancy are a common complication which affects around 10% of pregnancies [12], [13]. In turn, about half of these cases evolve into pre-eclampsia, a condition of risk that can lead to eclampsia, which is the leading cause of maternal mortality in Latin America and the Caribbean, as well as in developed countries, with an incidence of 25.7% of cases in Latin America according to the latest figures available [14]. There are multiple studies [12], [15], [16] indicating that control of blood pressure at home or on an outpatient basis would allow early detection of pre-eclampsia as well as discrimination from those cases related to the so-called white coat hypertension [16].

Different techniques for the non-invasive BP assessment can be found in the literature [17]. Due to the relevance of this work, some of them are discussed in this section.

2.2.1 Occlusive techniques

Figure 2.7 schematizes the process of occlusion and restoring blood flow in the brachial (peripheral) artery. Conventional BP assessment is based on the occlusion, which takes advantage of the phenomena behind the artery occlusion.

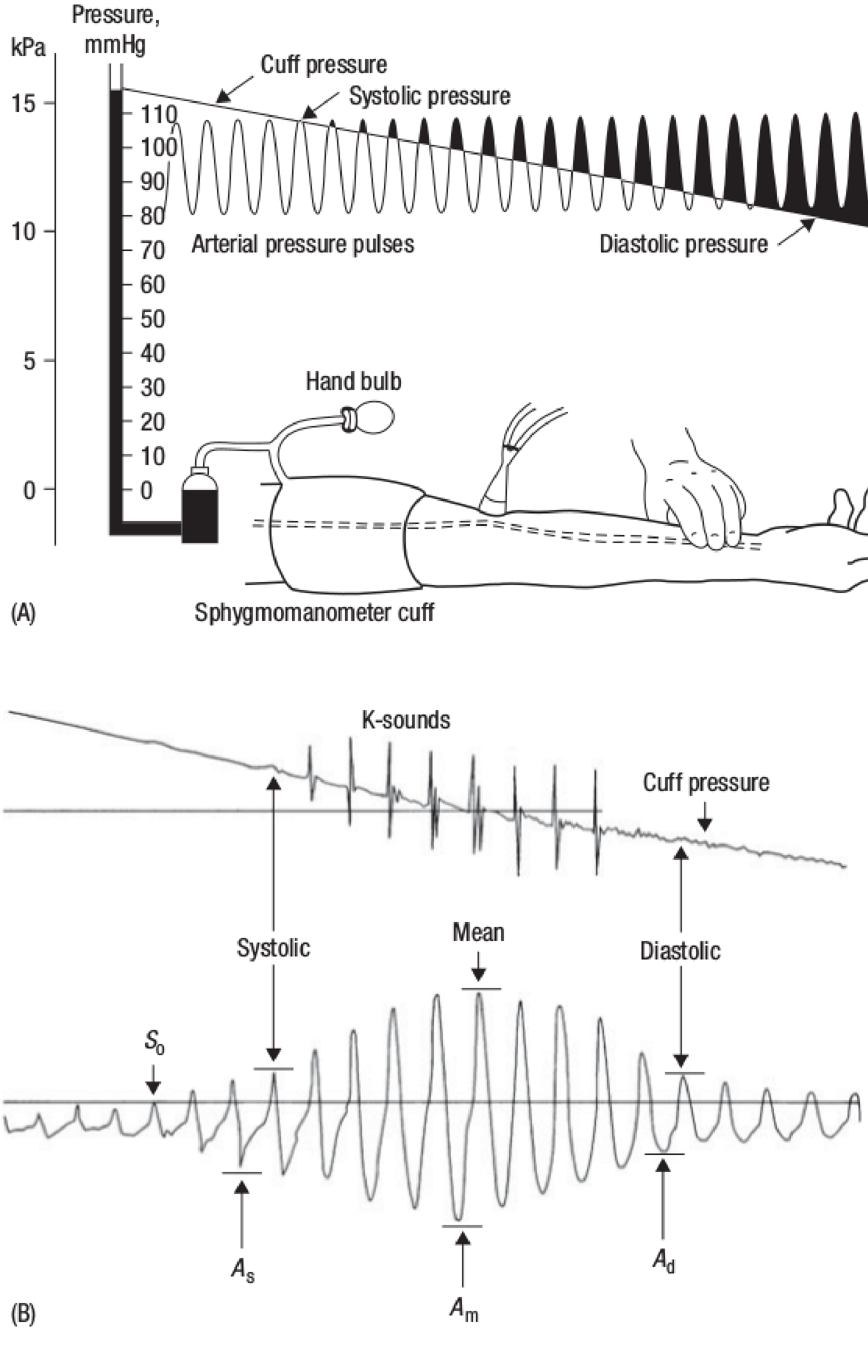

Figure 2.7: Occlusion procedure in a peripheral (limb) artery. Source [6]

In the procedure, an inflatable cuff is placed around the peripheral artery. The cuff is inflated exerting pressure on the limb artery to a value above the maximum intra-arterial (supra-systolic) pressure, thus bypassing the longitudinal blood flow of the artery through the cuff. Then, the cuff pressure is gradually relaxed, and a phase of turbulent blood flow begins. When the pressure exerted by the cuff is lower than diastolic blood pressure, the steady-state flow is reached again. In this process of occlusion and release, a couple of physical phenomena occur, which are exploited by the traditional occlusion techniques (auscultation and oscillometric). Note that, described procedure assesses only to local BP variables, the ones occurring at the occluded peripheral artery, the brachial in this example, which are arterial districts far from the organs of interest (to which blood pressure can cause permanent damage, these are, brain, kidneys, eyes). Finally, the occlusion is a bothersome procedure, which might cause artery injuries if it is used frequently for large periods; this is one of the main technique drawbacks.

2.2.2 Auscultation

The turbulent blood flow phase is identifiable by hearing characteristic sounds with the stethoscope. These sounds are known as Korotkoff sounds, K-sounds on figure 2.7.B. In the procedure, the artery to be assessed is occluded with a cuff. The stethoscope diaphragm is put over the artery next to the cuff (at the occluded side of the artery), whereas the cuff must provide the actual pressure (from a sensor) to be displayed somehow, a mercury column is used in the example in figure 2.7.A. Accordingly, mercury sphygmomanometer is known as the auscultation-based device for assessing BP where the cuff pressure is measured with a mercury column. Systolic and diastolic variables are thus assessed by identifying the boundary cuff pressure values in which the turbulent flow is ranging (or equivalently, the range that k-sounds are audible).

Auscultation technique was discovered more than 100 years ago, and despite the significant advances in technological resources in this period, this technique is nowadays the favorite for the non-invasive BP monitoring. The mercury sphygmomanometer represents the *gold standard* for the non-invasive BP assessment. The technique has demonstrated (throughout all these years) its robustness to predict cardiovascular events, comprises a simple procedure to perform, and does not require expensive material. Also, the method is characterized by the accuracy, and the expected offset and precision error limits are less than $\mu_e < 5mmHg$ and $\sigma < 8mmHg$ (respectively) against an intra-arterial catheter reference. However, the technique has some drawbacks; requires a trained operator to obtain the measurement correctly, the pressure can fluctuate minute by minute and a single BP snapshot may not be representative assessment, it is a cumbersome measurement for the user which in turn, may be vulnerable to the white coat effect and, the accuracy depends on the operator, on the deflating rate and also of the position of the bracelet. Despite having its setbacks, it seems a technique that resists its replacement in the near future.

2.2.3 Oscillometric

Oscillometric methods provide automatic (operator-independent) access to peripheral blood pressure through the arterial occlusion process. In operation, the oscillometric device CPU records the pressure pulses exerted by the occluded artery and exploits another phenomenon that occurred in the occlusion. The amplitudes of pressure pulses impacting against the cuff, depend on the pressure exerted externally by the cuff, these amplitudes reaching a maximum approximately when the external pressure is equal to the mean value of intra-arterial pressure (See fig. 2.7.B). The procedure, thus, could find approximately the mean blood pressure of the assessed limb by analyzing pulse amplitude. Then systolic and diastolic variables are estimated through proprietary algorithms. While these methods may have less accuracy than the ones based on auscultation, they are quite reliable and accurate, so making them attractive to users. The measure does not depend on the operator and the method gain in repeatability. Moreover, and very relevant in this context, the method opens the gap of outpatient BP monitoring. Finally, despite the accuracy issues, automatic oscillometric devices might be the adequate reference device for initial validations in the development of PTT-based BP monitoring systems [5].

2.3 Non-invasive central aortic blood pressure assessment

Even though BP readings at peripheral districts (i.e., at brachial, radial or femoral arteries) are important markers for the assessment of cardiovascular risk, there is a strong rationale and published evidence showing that central BP might be a better parameter to follow up cardiovascular health [2] [3] [4]. For instance, key organs and the major arteries supplying the brain are directly exposed to aortic rather than peripheral BP. Other reported evidence in favor of the use of central arterial BP (CABP) is the following. First, there are relevant discrepancies in CABP among people with similar peripheral BP (PBP). Second, the prognostic of end-organ damage by CABP is independent of the one by PBP [3]. Finally, there exist differential reactions to anti-hypertensive drugs through CABP and PBP [18]. Consequently, it is expected that CABP and PBP predict cardiovascular events and mortality differently. Non-invasive CABP estimation is possible based on carotid pressure assessments by applanation tonometry [19] and ultrasound techniques [20], or, through the use of a generalized transfer function from a peripheral pressure assessment [21] [22]. Nevertheless, all of them require either a trained operator or a brachial cuff for CABP estimation. Other methods for non-invasive CABP estimation based on inflatable cuff recordings and arterial modelling could be found in the literature [23] [24]. Nevertheless, the cuff requirement makes unfeasible the wearable and ubiquitous CABP monitoring.

2.3.1 Applanation tonometry techniques

The method estimates the CABP waveform from the assessment of a BP waveform at another artery. For instance, CABP is directly estimated by the carotid BP waveform, or conversely, the CABP waveform is estimated by using a generalized transfer function (GTF) with the radial BP waveform. A pressure sensor (applanation tonometer) over such arteries is used for the BP waveform registration. Since sensed pressure by tonometer is subject to inherent inaccuracies (motions, applanation issues) [7], the absolute intra-arterial pressure might differ from the sensed by the tonometer, and the waveform must be calibrated against an automatic (sec. 2.2.3) or manual (sec. 2.2.2) peripheral blood pressure assessment. However, the former is, in turn, subject to the widely known inaccuracies of the oscillometric based techniques, while the latter might suffer variability issues [25] being an operator-dependent procedure. Nevertheless, radial applanation tonometry is considered the gold standard procedure for the non-invasive assessing of the CABP [26] [27]. The technique has been successfully validated against invasive catheterization [27], even during tests involving exercises [26].

2.3.2 Generalized transfer function approach

AtCor Medical - SphygmoCor XCEL

Reference CABP measurements in this work were assessed with the SphygmoCor XCEL (AtCor Medical, West Ryde, Australia) unit by using the pulse wave analysis (PWA) [28]. Figure 2.8 shows such a cuff-based device used as a non-invasive CABP reference. The unit has been extensively validated for non-invasive central hemodynamic assessment [21] [29] [30] [31] [32], and the measurement is not based on the operator expertise. Regarding the assessment, the completion of a standard PWA attempt lasts in the order of 90 to 120 s to be accomplished. The device constructs a CABP waveform by extracting parameters derived from the brachial waveform by using proprietary signal processing over a sub-diastolic volume displacement recording [21], which is assessed with a cuff at sub-diastolic pressure on the brachial artery. As a result of a PWA assessment, a snapshot of variables extracted from the assessed PBP and estimated CABP waveforms are available. These are systolic, mean, diastolic, and augmentation index for CABP waveform, and, systolic and diastolic variables for brachial BP.

2.4 Cuff-less BP estimation: the pulse transit time method

The non-invasive method for measuring blood pressure has been based on the use of inflatable cuffs. Although the cuff-based method may provide accurate or autonomous paths for the BP assessment, it still has several disadvantages, such as occlusion, annoyance, heart workload, and interruption of activities. Moreover, cuff-based methods provide only intermittent measurements; that is, after an assessment attempt (that lasts in the order of minutes), only a snapshot of BP variables (of the occluded) artery are available. Consequently, it nullifies the

Figure 2.8: AtCor Medical - SphygmoCor XCEL. Cuff-based device used along this thesis for the central aortic blood pressure assessment. Figure from [33].

possibility for monitoring dynamic fluctuations of BP, which might be a determinant of cardiovascular risks [17], but also, it would eliminate any possibility of incorporating short term mechanisms to control BP. In order to achieve a method for estimating BP continuously, several groups [34], [35], [36] have worked on BP monitors based on the pulse transit time (PTT) method. The method would be capable of construct a new BP estimation at each heart-beat from the measurement of the time that a pulse pressure propagates along a particular segment of the arterial tree.

Pulse transit time (PTT) method

PTT-method is based on some effects on the pulse pressure propagation along the arterial tree. Principally, given that PWV is assessed by the transit time it takes the pulse pressure to travel a fixed vessel distance (L) in the cardiovascular tree (ec. 2.5); and, propagation models presented in 2.1.2, Moens-Korteweg in 2.4, and Bramwell-Hill in 2.2, that show how PWV is dependant of arterial distensibility (or, reversely, the stiffness). The pulse (pressure) transit time (PTT) is consequently also related to such an arterial wall property.

$$PWV = \frac{L}{PTT} \tag{2.5}$$

On the other hand, it is well-known that arterial distensibility (stiffness) is, in turn, affected by blood pressure. In effect, equations 2.6 [37] and 2.7 [38] show different models available in the literature, for the compliance and the elastic modulus, respectively, at central elastic arteries (near the aorta) as a function of the internal pressure (P).

$$C_{as}(P) = \frac{A_m}{\pi P_1 \left[1 + (\frac{P-P_0}{P_1})^2\right]} \tag{2.6}$$

$$E(P) = E_0 e^{\alpha P} \tag{2.7}$$

where, A_m, P_0, P_1, E_0, $\alpha > 0$ are subject dependant parameters. Eventually, artery distensibility (stiffness) might depend on other factors such as age, heart rate, treatment, and medication. However, by assuming that BP could be treated as the main factor that affects the arteries stiffness; thus, PTT could be threaded as a BP surrogate. PTT-method is based on such a hypothesis and thus, for a particular PTT, the method proposes that a BP could be found bi-univocally. Furthermore, the mathematical relationship between measured PTT and estimated BP are known as the PTT-based models (PTTBM).

Several PTTBM could be found in the literature, for instance, in chapter 7 some of them are explored for the CABP estimation and, in chapter 8 a novel PTTBM is proposed. Notably, a very popular PTTBM (eq. 2.8) could be derived by combining 2.5, 2.6 and 2.2 [39].

$$P \approx \frac{\sqrt{\frac{A_m P_1 \rho L^2}{\pi A}}}{PTT} + P_0 \longrightarrow P \approx \frac{k_1}{PTT} + k_2 \tag{2.8}$$

Where k_1 and k_2 are subject dependent parameters that could be resolved from a calibration procedure (basically, through parameter fitting routines by using pairs of P and PTT data); otherwise, P in 2.8 should be a value derived from the CABP waveform so that this theory is consistent. However, it does not exist a formal answer about the BP value that is related to PTT [8]. Most works use the systolic values [40] [41] (noteworthy, the PEP is included in the PTT assessment in many of those works, see sections sec. 2.4.1 and 2.5), whereas others propose that the mean/diastolic value of BP should be estimated from PTT [42] [43]. Moreover, even though the PTT theory is derived from artery models mainly elastic (near the aorta), most works use the PTT-method for estimating BP at peripheral locations, where neither the estimated pressure (CABP and PBP may be uncorrelated) nor the pulse propagating district corresponds with merely elastic arteries. Eventually, some abuse on the use of the PTT-method may be commonly found. This also occurs for the PTT assessment itself, where for simplicity in the acquisition, PTT may be commonly approximated, and thus, the assessment may include portions of time that are not purely a pulse propagation time (as will be shown in sec. 2.4.1).

Eventually, such approximations and other issues found (such as instrumentation accuracy, within person BP variability, smooth muscle contraction in the aorta) [5] might lead to inaccuracy problems for the PTT-based BP estimation which may be one of the main limitations of the PTT-method nowadays. Mainly if an Association for the Advancement of Medical Instrumentation (AAMI) type criteria is used for assessing the accuracy of the PTT-based estimation, where the device under test would be compliant with the AAMI accuracy if a bias error of $\mu_e < 5\ mmHg$ and precision of $\sigma < 8\ mmHg$ could be achieved against an auscultation reference [44], typically, such criteria is used for assessing the accuracy of oscillometric devices. Also, it might be in a kind conservative for the PTT-based methods. In effect, PTT-based systolic (diastolic) BP estimation could reach up to a bias error of $\mu_{es} = 10\ mmHg$ ($\mu_{ed} = 10\ mmHg$) and a precision error of $\sigma_s = 14\ mmHg$ ($\sigma_d = 11\ mmHg$), against an automatic cuff device reference, and the method still may be capable of screening hypertension [5].

Finally, PTT method emerges as an attractive approach for estimating BP since PTT could be assessed by using hand-held equipment, thus, the method may lead to the conception of an unobtrusive BP monitoring device, by eliminating any cumbersome inflatable cuffs and by also providing a continuous (that is, beat-to-beat) BP estimation.

2.4.1 PTT assessment

Several publications about pulse transit time assessment have shown that PTT can be accessed from the processing of at least two physiological signals [34], [35], [45]. For example, the ECG R-wave could be (roughly) considered as a time reference for the onset of the propagation of a pulse pressure (see sect. 2.1.3). Despite the inaccuracies, R-wave is a often preferred proximal reference by the PTT-method developers because ECG is a relatively easy physiological signal to acquire [39]. On the other side, the ballistocardiogram (BCG) offers diverse possibilities as a timing reference which emerges as an valuable physiological signal to be exploited in the PTT context.

Mechanical response to heart activity: the ballistocardiogram

Ballistocardiogram is a measurement of the body response caused by the blood ejected during the cardiac systole. The blood mass displacement confined at the arterial tree experiments accelerations and forces that are recoiled by the body in the opposite direction. Consequently, slight body accelerations are expected at each heartbeat mainly experienced in head-to-foot direction. Former studies in this area were implemented with constrained devices, such as suspended tables and then with chairs and weigh scales, restricting the measurements only to a medical/research environment. However, some works [46], [47] have proved the feasibility of integrating small sensors (based on electromechanical films (Emfi) or Microelectromechanical systems (MEMS)) in ambulatory and wearable devices which, in turn may enable continuous time monitoring.

The BCG is composed of several characteristic waves named with letters from G to O as were covenanted in the Scarborough-Talbot Report [48] by the Committee on Ballistocardiographic Terminology. In practice, the BCG acquisition is subject to low signal-to-noise ratios principally due to weakness of the BCG effect itself, motion artifacts, noise, and involuntary movements. The H, I, J, K, and L waves,

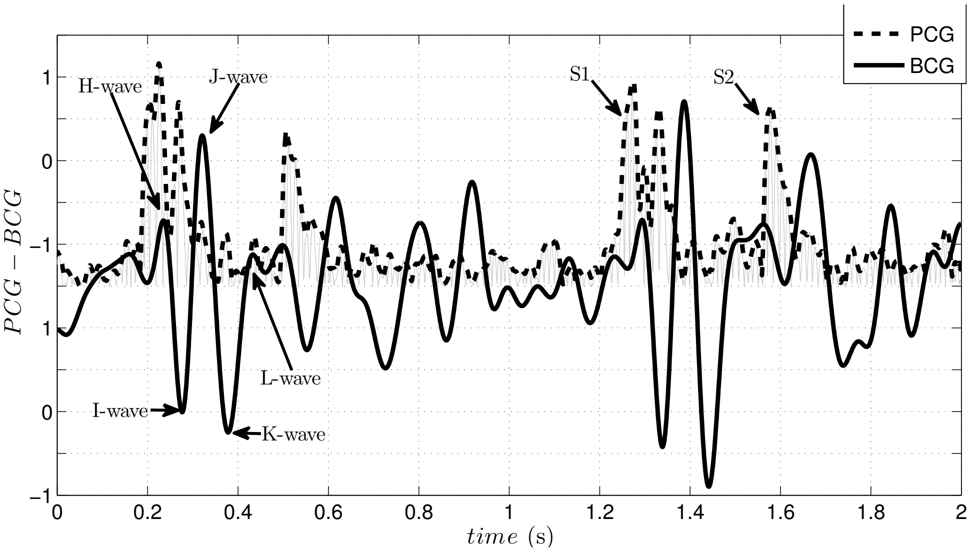

Figure 2.9: Phonocardiogram envelope and Ballistocardiogram.

indicated in Fig. 2.9, are in general, the strongest ones and those who give it its characteristic morphological shape. Notably, the H-wave has presented particular relevance compared to others since it was reported of occurs nearby the first heart sound [49] (shown as S1 in Fig. 2.9). Eventually, it could be an alternative for determining approximately the S1 event, as shown in Fig. 2.9, where the phonocardiogram envelope is superimposed on a BCG. Otherwise, the J-wave, also one of the most relevant waves and especially crucial for this work, corresponds to the first positive deflection from the H-point of the BCG signal. It was reported to coincide with the reaction caused by the blood displacement approaching the aortic arch and going through the descending aorta [50]. Also, it has been documented that the J-wave amplitude is correlated with stroke volume [51]; therefore, the cardiac output could also be estimated from BCG. Further information about ballistocardiography can be found in the literature [50] [52].

2.5 PTT-based device for CABP monitoring: wearable implementation

Measuring PTT as a surrogate of BP may lead to the conception of a wearable, unobtrusive, BP monitoring device. Nevertheless, the approach (a priori) requires the placement of two sensors on the body to find a pair of (proximal and distal) arterial waveforms. These waveforms are used to compute, on a beat-to-beat basis, the time that will be related to the BP, referred as feature time (FT) from now on since, as was discussed, the role of PTT might be filled in by an approximation that not strictly corresponds witha a PTT. Therefore, PTT, any PTT approximation, even the defined PEP are grouped in this FT category in this document.

Various PTT based approaches use the electrocardiogram (ECG) signal as proximal reference, and, another arterial waveform as the distal counterpart (e.g., photoplethysmogram (PPG) [53] [54] [55], ballistocardiogram (BCG) [56], magnetoplethysmogram (MPG) [57] [58]). When the ECG R-wave is used as a proximal reference, the FT is actually called pulse arrival time (PAT) because it includes not only the pulse transit time but also the PEP. There is controversy on whether the PEP inclusion in the FT is beneficial or detrimental to the BP estimation. Some works have highlighted the positive effect of PEP on such estimation [59] [60]. Meanwhile, other works have reported that BP and PEP may change independently [61] [43], and thus BP prediction from PAT would be inconvenient. This thesis will contribute to this discussion later on.

BCG waveforms can also be used to provide a proximal timing reference, since the I-wave on the BCG wave approximately indicates the initiation of the mechanical ejection of the heart [52]. Therefore, the R-I interval, i.e., the time interval between the ECG R-peak and the I-peak on the BCG, may correlate with the pre-ejection period [62]. Then, PEP can be disjointed from PAT to provide an FT that is independent of PEP; or conversely, PEP can be eventually assessed, since it is a non-invasive marker that may reflect the sympathetic nervous system activity [63]. Therefore, the BCG waveform, by itself, may contain information about pulse pressure propagation time at the aortic level. Notably, as was shown, BP-PTT dependency is mainly exploitable at elastic arteries [64] which are principally found on or near the aortic district. Additionally, although many of these works measure pulse propagation's mostly at aortic domains, none of them consider that the central (aortic) blood pressure is the most suitable parameter to collate for. In this work, it is proposed to use the presented PTT-method to estimate central aortic blood pressure rather than peripheral BP.

The CABP estimation from an aortic pulse propagation time was previously studied in [65], where a proposed approach for CABP estimation is based on employing the electrical impedance tomography technique. This method has the drawback of involving complex image processing, cumbersome hardware, and the need to inject electrical excitation into the body. The approach may be very constrained in a wearable application. This work aims to achieve a PTT-based methodology for the wearable estimation of CABP, which, to our knowledge, was not achieved yet. The material presented in this thesis contributes in that direction where a proposed wearable device was developed, and results show that wearable CABP estimation can be achieved by the proposed approach.

Chapter 3

PTT-Based Central Aortic Blood Pressure (CABP) Estimation: Proof of Concept

Chapter Summary

This chapter presents the proof of concept for the non-invasive central aortic blood pressure (CABP) estimation based on the pulse transit time (PTT) principle. A beat-to-beat PTT was estimated from electrocardiogram (ECG) and ballistocardiogram (BCG) recordings. As the measured transit time takes place mainly within the aortic domain, CABP was estimated instead of brachial pressure. Validation of the proposed method was performed with a small sample of healthy volunteers during strength maneuvers. Atcor Medical SphygmoCor XCELL device was used to monitor central and brachial blood pressure (systolic, mean, and diastolic) during the rest of the strength maneuvers. Pulse transit time was estimated from ECG and BCG recordings and simultaneously recorded with all BP readings. Results showed that systolic and mean central blood pressures were strongly correlated with PTT-estimated blood pressure in comparison to all other blood pressure variables, particularly, the brachial variables. Bland-Altman plots showed an almost zero mean error ($|\mu| < 0.02$mmHg) and bounded standard deviation $\sigma < 5$mmHg for all systolic and mean central BP readings. Experimental data thus showed promissory results for monitoring aortic blood pressure via PTT. The scope of this pilot work is to provide initial validation of this method in order to develop a compact miniaturized device that allows the integration of wireless blood pressure monitoring into a wearable system. The chapter is organized as follows: The context of this pilot study is presented in 3.1. Experimental methods are described in section 3.2. Then, section 3.3 shows preliminary measurements of the proposal. Finally, discussion and perspectives are included in section 3.4 and conclusions are drawn in section 3.5.

3.1 Study Context

The study presented in this chapter was the result of an exploration period with the PTT-method to estimate BP. PTT-method provided characteristics that are aligned with the primary objective of this thesis, the conception of a wearable device for BP monitoring. Several possibilities for the PTT acquisition were explored at that time, methods included: PTT computation from electrocardiogram (ECG), photoplethysmogram (PPG), ballistocardiogram (BCG) and magnetoplethysmogram (MPG) signals. In this context, ECG-BCG-based PTT provided the best correlations with BP at the time, and thus, ECG-BCG-based PTT became the best surrogate candidate for the BP estimation, conjecture which, needed to be further studied. Not mention that BCG acquisitions from longitudinal (head-to-feet) orientated accelerometer along with an adequate ECG acquisition might lead to a compact and low-power implementation of a wearable device. Additionally, since the ECG-BCG-based PTT defines a time elapsed for a pulse pressure to propagate at aortic domains, it was considered that the central aortic blood pressure (CABP) was the most suitable parameter to collate for. The major proposition of this proof of concept study is based on this hypothesis, that is, the ECG-BCG-based PTT needed to be collated to CABP rather than peripheral BP as typically analyzed in the literature. Such investigation is presented in this chapter.

At the time of the study presented in this chapter, there were some limitations to the methodology which should be noted here.

- Proposed ECG-BCG-based PTT includes a delay between electrical and mechanical activity of the heart; accordingly, the pre-ejection period (PEP). As widely considered in the literature [45] [66], and also in this work, PEP was assumed neglectable in the PTT assessment. Nevertheless, as will be shown throughout this thesis, PEP might not be utterly neglectable against an aortic PTT, and further, PEP will have a more leading role in our BP estimation than a simple error in the PTT assessment.

- Only one PTT-based model was evaluated to study its suitability for the blood pressure estimation. More alternatives are further studied later in chapter 7. Also, and more importantly, the approach used to evaluate the proposed method was based on calibrating and testing the PTTBM using the same group of data-sets for both operations. Although such an approach does not provide an ultimate validation [39], it was enough to give an insight into the feasibility of the proposed methodology. A moderate-hard validation approach might be based on predict accurately unseen BP data, which was the case for further validations.

- Data in this proof of concept were acquired with off-the-shelf equipment and custom hardware. However, the estimation of PTT could be spuriously affected at its signal-conditioning stages. Frequency limiting stages could produce phase lags between reference signals [67], accordingly ECG and BCG, resulting in a corrupted PTT. Potentials issues with the acquisition material were not rigorously analyzed at the time; phase issue was not

> considered in this proof of concept. Nevertheless, the concern is studied in the following chapter and represents one of the main contributions of this thesis.

Finally, despite the limitations of the study presented in this chapter, results shown that the CABP estimation by the presented cuff-less method is feasible.

3.2 Methods

As was previously discussed, an ECG-BCG-based PTT was pre-selected as a surrogate for the CABP estimation. Particularly, the time delay elapsed between ECG R-wave and BCG J-wave was the considered feature time (FT) for this work; and, such FT reasonably meets the transit-over-aorta condition if the pre-ejection period is neglected. Otherwise, ECG and BCG signals could be acquired simultaneously from the chest [66], thus appropriate for a future wearable device implementation. Wearable devices based on PTT definitions from very distal physiological locations require, cumbersome cables to operate or a wireless communication between sensing devices [45] [68]. Besides the increasing of power consumption, those later require precise synchronization between such distant devices. For the time being, an acquisition system mainly based on off the shelf equipment was used in this proof of concept work, which is enough since the scope of this work is solely to validate the measurement principle.

3.2.1 Hardware

Signals are acquired with the BIOPAC MP-36 unit (Biopac Systems Inc.) and particularly its ECG module used to obtain the electrocardiogram signal. BCG acquisition is performed with the Analog Devices ADXL335 accelerometer chip attached to the chest. This integrated circuit features a surface-micromachined sensor, conditioning circuitry with analog output, full scale range of +/- 3g and low power characteristics (350uA typ at 1.8V power supply), making it fairly suitable for a wearable device. A custom analog front-end (AFE of BCG AFE on Figs. 3.1) circuit is also included to condition the sensor signal prior to its acquisition by the MP-36 module. Fig. 3.1b summarizes the hardware and software paths for ECG and BCG signals, and Fig. 3.1a shows a scheme of the test-bench used in this experiment.

3.2.2 Signal processing

The signal processing section was performed with a Matlab/Octave script. The morphological characteristic pattern of each signal, i.e., PQRST waves for ECG and HIJKL waves for BCG, extracted from basal measurements of each subject, was swept to correlate with the signal itself in order to find where R-and-J-waves occur. Figure 3.2 shows the signals involved in such processing when a small

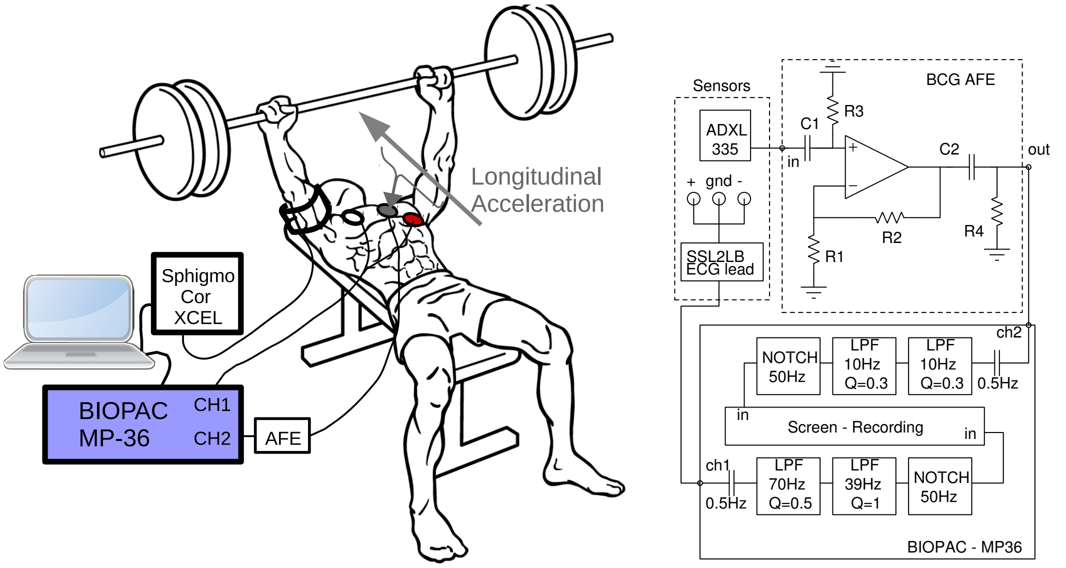

(a) Strength manoeuvre and test-bench

(b) Sensors, and hardware and software signal-paths

Figure 3.1: Acquisition scheme: (a) ECG and BCG were acquired with the BIOPAC MP-36 device. Central and brachial BPs were assessed with the SphygmoCor device (sec. 2.3.2). Measurements were acquired during the rest of the strength maneuver (sec. 3.2.3). (b) ECG and BCG signal-paths from the sensors to the recording in the computer. Electronics at BCG-AFE: $C_1 = 10\mu F$, $C_2 = 1\mu F$, $R_1 = R_3 = 47k\Omega$, $R_2 = 1M\Omega$, $R_4 = 100k\Omega$; analog circuitry implements two passive high-pass-filters to decouple DC from sensor ($f_{3dB} = 0.34Hz$), and towards the BIOPAC unit ($f_{3dB} = 1.6Hz$), along with an active gain section of Gain=22.3 V/V.

segment of the ECG and BCG recordings are considered. That is, firsts wave-patterns (PQRST waves for ECG and HIJKL BCG) at each signal are correlated throughout all the recording. ECG and BCG correlation result waveforms (Fig. 3.2) present a local maximum coinciding with the desired waves, R and J at ECG and BCG, respectively. The algorithm finished by launching a simple (threshold-based) peak algorithm over the correlation (result) waveforms in order to find a beat-to-beat PTT. ECG and BCG waveform section to be swept were chosen so its lengths only included the wave-pattern, and more critical so that they were wave-patterns as representative as possible, the decision was based on the overall vector observation. That is, both signals are subject to motion artifacts (specially BCG), and by choosing a representative waveform pattern adequately, the accuracy of the correlation swept algorithm is maximized.

$$BP = \frac{A}{PTT} + B \tag{3.1}$$

As presented in chapter 2, work in this area requires a model to estimate Blood Pressure using pulse transit time, ec. 3.1 is the previously introduced PTTBM recommended in the literature [39]; in chapter 7 the performance of several PTT-based models are further analysed for the CABP estimation. In this chapter, model

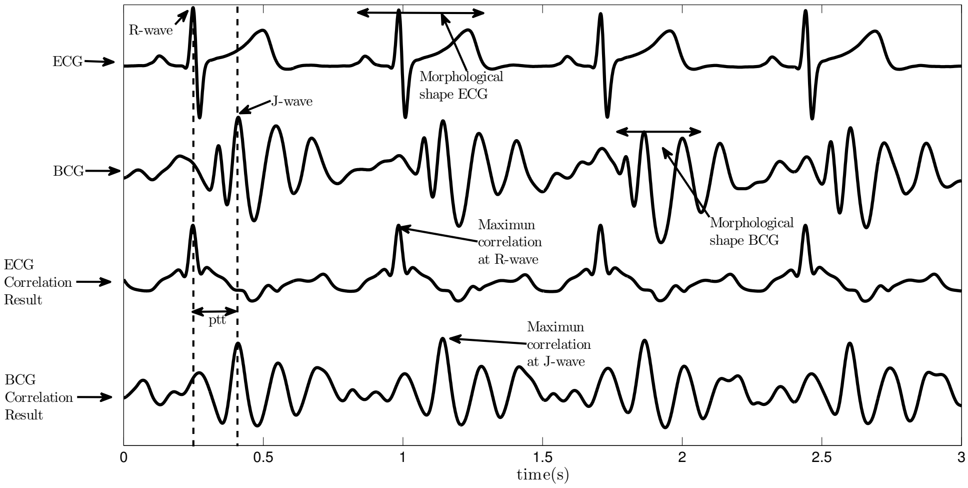

Figure 3.2: Signals involved in the PTT acquisition. Firsts appeared wave-patterns (PQRST waves for ECG and HIJKL BCG) are correlated throughout all the recording, and thus, generating two new signal vectors from the result of the correlation. Algorithm code was generated so correlation vectors presents local maximums coinciding with R and J waves.

in eq. 3.1 is used to construct a beat-to-beat aortic blood pressure estimation. A and B are subject-dependent coefficients which were found via least-squares fitting with recorded data.

3.2.3 Measurements

The proposed technique was validated with measurements as follows. ECG and BCG signals plus BPs were registered in six male volunteers (between 18 and 50 years old ¡ mean 30 years, SD 12 years ¿) during their typical workout session at a local gym in Paysandú - Uruguay (fig. 3.3). Particularly, Brachial - systolic and diastolic - and Central - systolic, diastolic and mean - blood pressures were registered with Atcor Medical SphygmoCor XCEL device using a cuff around the upper arm. The brachial mean blood pressure is not included because it is not provided by the SphygmoCor. Meanwhile, BCG and ECG signals were recorded with the previously mentioned BIOPAC hardware system. A continuous recording of these signals provided a discrete beat-to-beat PTT assessment. A moving average (ten samples) filter was used over the beat-to-beat PTT for smoothing (solid line in figure). Contrarily, in the cuff-based SphygmoCor blood pressure, only discrete BP snapshots (dots in figure) were accessed with at least 1-minute intervals between measurements. During the trial, each volunteer performed strength maneuvers to provoke changes in BP; data were recorded at rest in order to minimize motion artifacts in the same upright sitting position. The measurement process was conducted using the following steps:

1. Trial protocol began with basal measurements. Six subjects were asked to relax for approximately 5 minutes in a sitting position, then the ECG and BCG signals were recorded during two SphygmoCor discrete measurements.

Figure 3.3: Local Gym Maneuver: Volunteers were asked to perform their typical strength maneuvers in a gymnasium at Paysandú (Uruguay). SphygmoCor cuff was placed at the upper arm to perform the CABP, and PBP assessments, ECG and BCG were acquired simultaneously.

2. Recording was paused and subjects were then asked to do twenty repetitions on the bench press with a moderate weight. Immediately after the strength maneuver was finished, another series of BP, ECG and BCG readings were collected during three (or four in some occasions) SphygmoCor measurements.
3. Step 2 was repeated two more times. Thus, at least eleven BP measurements were taken per subject in a trial; a total sample of N=77 BP-measurements were recorded.

3.3 Results

Figures 3.4a and 3.4b show central systolic and mean blood pressure measurements with our estimation based on the method proposed in this article (from acquired ECG and BCG), for one subject in a complete trial. The estimated (solid) line presents a local maxima at the beginning of the rest and then drops gradually to a basal level as expected. In addition, the relationship between peak amplitudes on the solid line seems to be in agreement with pressure peak values reported by the SphygmoCor device, suggesting correlation between magnitudes. Such trend is quantitatively reflected in table 3.1, whose entries represent correlations between each type of BP (i.e. measured and estimated), and actually, significantly better results were reached on aortic systolic and mean cases for most subjects. Eventually, this is a reasonable outcome since measured events mainly take place in the

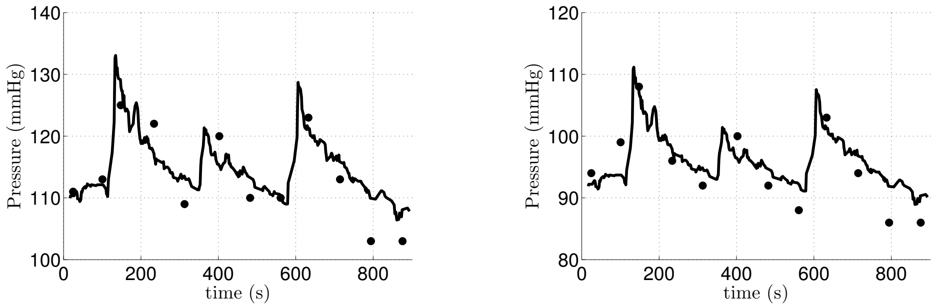

(a) Central Systolic BP

(b) Central Mean BP

Figure 3.4: Aortic Blood Pressure: Measurement (dots) and Estimation (solid line).

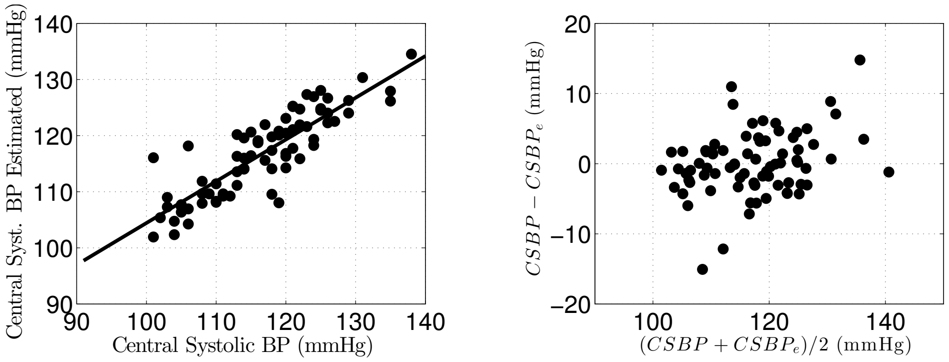

(a) Central Systolic BP(CSBP)

(b) CSBP: Bland-Altman

Figure 3.5: Mesurements vs Estimation (linear regression) and Bland-Altman plot, N=77.

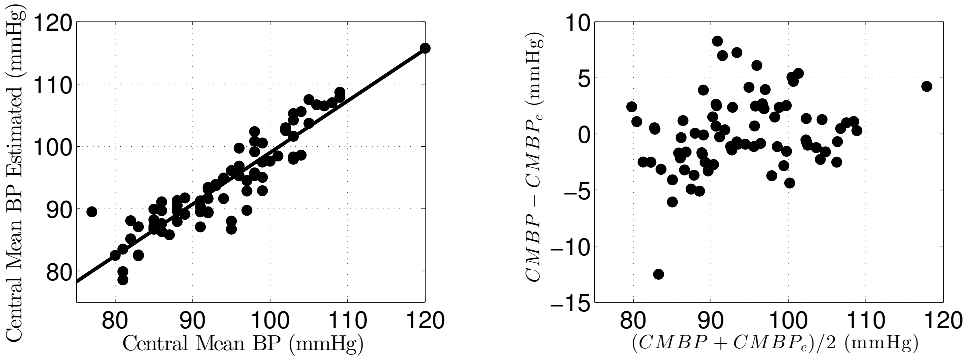

(a) Central Mean BP(CMBP)

(b) CMBP: Bland-Altman

Figure 3.6: Mesurements vs Estimation (linear regression) and Bland-Altman plot, N=77. Estimations were constructed from 3.1

aorta, and only there would it be appropriate to contrast them. Nevertheless, up to our knowledge, this has not been previously highlighted as method of estimation of the central blood pressure.

On the other hand, regarding population data (N=77), Fig. 3.5 and Fig. 3.6 present Estimation vs. Measurements and Bland-Altman plots for the mentioned Blood Pressures, demonstrating a reasonable agreement between measurement and estimation. In this context, correlation coefficients of $r = 0.89$ ($p < 0.05$) and $r = 0.92$ ($p < 0.05$) are obtained for the systolic and mean case respectively. Additionally, the identity line defined by Estimation vs. Measurements plots present a slope-intercept pair of m=0.75/b=30 mmHg and m=0.83/b=16 mmHg, respectively, showing slightly better results for the central mean BP estimation than its systolic counterpart. The same issue occurs in the Bland-Altman plots where data is slightly more scattered at the central systolic case (μ=-0.0133mmHg, σ=4.57mmHg) than for the central mean BP (μ=-0.0152mmHg, σ=3.32mmHg). Nevertheless, both data sets show that a reasonable estimation of central blood pressures could be made using the presented methodology.

Table 3.1: Association Table (Pearson Correlations): measured and estimated blood pressure. The model in 3.1 was calibrated to analyze its capability to estimate the following variables at peripheral and central aortic districts (all references were assessed with the SphygmoCor XCEL device (see sec. 2.3.2)).

	Brachial			Aortic	
Subject	Systolic	Diastolic	Systolic	Diastolic	Mean
1	0.61	0.46	0.9	0.57	0.89
2	0.7	0.25	0.81	0.32	0.77
3	0.79	0.46	0.85	0.43	0.78
4	0.3	0.72	0.66	0.86	0.89
5	0.57	0.72	0.73	0.73	0.79
6	0.66	0.48	0.78	0.42	0.86

3.4 Discussion and perspectives

The purpose of this investigation is to show the feasibility of this methodology to provide an aortic blood pressure estimation. Also, the method was conceived in order to be implemented without discomfort of any kind to the patient, suitable for a wearable application. As will be shown in this document, the material presented in this chapter served as prelude to achieve a compact and reliable implementation which is needed to gain confidence in a potential user. Additionally, although brachial BP has been the standard parameter for assessing hemodynamics within classical medicine, perhaps due to cultural reasons, it has been proven that central blood pressure presents richer aspects to perform a clinical outcome, and this method and in general, the work in this thesis, points to that direction. Further studies will be necessary to perform more exhaustive validations towards the implementation of the present method. That is, the following chapter presents the implementation of this method in a wearable device. The method along with the proposed wearable implementation (chapter 3) will be further validated in the next few chapters (chapters 6 and 7).

3.5 Conclusions

A non-invasive method to estimate central blood pressure with no occlusion and no annoyance was presented. This proof of concept work, despite its limitations (sect. 3.1), served as a seed for the research involved in this thesis. This chapter showed that CABP estimation is feasible from the proposed methodology, and the result was achieved based on experimentation with healthy volunteers. The method, based on ECG and BCG processing, might allow efficient CABP monitoring since it is a relatively easy extendable methodology to be implemented in a wearable device. That is, a proper sensor location might conceive a compact device, and it might allow a (relatively) low power consumption implementation due to the low consumption of the required sensing (ECG, electrodes, BCG, $I_{DD}@ADXL$ 335 $\approx 350\mu$ Amps). The conception of this methodology in a proposed wearable device is presented in the following chapter. The introduction of such types of wearable devices will undoubtedly help with the management of patients under suspect of cardiovascular risk.

Funding: This study was funded by Comisión Académica de Posgrado - Universidad de la República and Comisión Coordinadora del Interior - Universidad de la República.

Ethical approval: All procedures performed in studies involving human participants were in accordance with the ethical standards of the institutional and/or national research committee and with the 1964 Helsinki declaration and its later amendments or comparable ethical standards. The procedure of this study was approved and supervised by the Medical Review Committee of the Biological Engineering Department, Universidad de la República.

Informed consent: Informed consent was obtained from all individual participants included in the study.

Chapter 4

Proposed Wearable Device for CABP Estimation

Chapter summary

The previous chapter reported a method for estimating central (aortic) blood pressure from a feature time (FT), which includes a PTT at an aortic domain (such magnitudes may be referred indistinctly in this chapter). The method algorithm requires ECG R wave and BCG J wave detection. Nevertheless, the ECG-BCG-based FT estimation, being a delay measurement, may be affected by the group delay introduced by the signal conditioning chain of the acquisition hardware. A simple design approach for the signal conditioning chain, which can apply to any PTT-based device and, that takes care of minimizing the impact of eventually introduced spurious delays, is presented. The proposed approach provides less than 2ms group-delay. The design of a wearable device for ECG, BCG, and PTT acquisition featuring this conditioning is also presented. Experimental results of its application are reported, showing the effectiveness of the proposed approach. The work gives way for a wearable implementation of the central aortic blood pressure (CABP) estimation method presented in chapter 3. This chapter is organized as follows: section 4.2 presents the design criteria used to define the conditioning cores, which are discussed in section 4.3 for the analog one and in section 4.4 for the digital one. Then, section 4.5 shows overall results on the delay performance of the proposed filtering scheme which, is included in an implementation of a wearable device suitable for PTT acquisition (sec. 4.6). Section 4.7 presents measurement results on the wearable implementation. Finally, conclusions are drawn in section 5.5.

4.1 Introduction

A significant correlation between the FT (that it will refer indistinctly as PTT in this chapter) defined by ballistocardiogram J wave (BCG J wave) and electrocardiogram R wave (ECG R wave) and, aortic blood pressure was shown in the previous chapter [69]. Therefore, a continuous estimation of aortic blood pressure could be performed through a beat-to-beat PTT (FT) assessment. However, the measurement of PTT may be spuriously affected at the signal-conditioning stage where filtering inadvertently produces phase lags between signals [67], e.g., ECG and BCG in our case but the same applies to other PTT estimation methods. Despite being the PTT-method widely used in the literature to infer blood pressure, how to deal with the non-avoidable artificial phase shifting at signal-conditioning usually is not discussed. [66] applies the same IIR filter in the forward and backward direction to nullify the phase delays, but no caution was taken at the analog domain, and also such a digital filtering technique requires first to store whole signal sections.

Ideally, by keeping a zero-phase shifting along the processing chain for the ECG and BCG signals would guarantee uncorrupted PTT results, at least due to conditioning. However, a priori it would imply an excessively large analog filtering bandwidth since phase shifting increases as signals reaches the cut-off region. On the other side, constant group-delay filtering delays the signal events to be detected with a constant offset, but if the same constant group-delay is applied at both signal paths, the PTT, which is estimated as the time difference between two events, is unaffected. Usual analog filter design techniques uses magnitude frequency response requirement as main specification but presents large group-delay ripples at the limit of the pass-band which could be inadmissible in the considered application. The problem of controlling group delay in filters has been widely researched, in particular in the domain of communication systems [70]. Usually, an all-pass network is connected behind the analog filter to modify the phase-shifting conveniently and so seek to optimize the group-delay response [71], but this approach, though achieving high performance implies to add components and complexity to the design not compatible with low power, compact wearable device. Sometimes, filter order is increased to enlarge the constant-group delay region in the band, but at expenses of increasing the overall shifting, and that also increases consumption and complexity.

This chapter presents a proposed approach for signal conditioning of a PTT-based monitoring device suitable for a low power wearable implementation, which also takes into consideration the phase-shifting impact. Additionally, the ideas shown in this chapter are also incorporated in the conditioning circuitry of a proposed wearable device suitable to the PTT measurement. The wearable device was conceived to be capable of implementing the methodology presented in the previous chapter for the PTT-based central aortic blood pressure estimation.

4.2 Design criteria

The solution proposed in this work aims to induce an almost zero phase shifting between EGG and BCG signals to reach a PTT estimation that is free of offset and distortion. Moreover, in order to give the device a truly wearable characteristic, the design approach was based on reaching a as compact, autonomous and simple device as possible, so area, consumption and complexity are among the design priorities.

Since the average spectral support of the QRS complexes is $QRS_{BW} = (6, 30)Hz$ [72] [73], the design criteria were based on minimizing any eventual phase shifting at such domain in the ECG conditioning, or at least to guarantee a reasonable group delay at such region. On the other hand, it was reported [74] that most relevant spectral components of the BCG signal are located approximately in the same region as considered for the ECG; therefore, the same strategy design was adopted for both signal paths (the ECG and the BCG). Furthermore, as will be shown, the conditioning approach aims to apply the same filtering for both signals in order to cause (approximately) the same small delay at both signals, and thus, the resulted PTT would be unaffected from filtering.

In order to meet the goal of having a compact, low power, wearable device, the analog front-end was designed trying to minimize the number of components, particularly the active ones. On the digital side, the sampling frequency was fixed at the minimum necessary to reasonably estimate the transit time, as discussed next. Time quantization introduces an error at BCG J wave and ECG R wave time detection, which consequently implies an error in the PTT estimation. Therefore, the maximum allowable error defines a minimal sampling frequency. Taking a $1/2T_s$ error model for the detection of the start and end of the PTT period, the error in PTT estimation becomes less than 4 milliseconds (ms) for a $f_s = 250Hz$ which would lead to a less than 5% of uncertainty for an expected PTT (FT) of about 100 ms. Finally, such minimal allowable sampling frequency also requires the proper anti-aliasing treatment which in turn should be addressed at the analog front-end.

4.3 Analog core

4.3.1 Analog phase shifting

This section aims to present a result used in this work about phase shifting in first and second order low pass filter implementations. In particular, these results allow to design these filters for a given phase shift ($\Delta\phi$) specification at a given frequency f_0 (with corresponding angular frequency ω_0). For a first order low pass section with transfer function $H(s)$ the relationship of -3dB cut-off frequency ω_p with $\Delta\phi$ is as follows.

$$H(s) = \frac{\omega_p}{s + \omega_p} \tag{4.1}$$

$$\begin{aligned} \Delta\phi = Arg(H(j\omega_0)) &= atan(\frac{\omega_0}{\omega_p}) \\ \Rightarrow \omega_p &= \frac{\omega_0}{tan(\Delta\phi)} \end{aligned} \tag{4.2}$$

For a second order low-pass filter written in terms of its natural (cut-off) frequency (ω_n) and damping ratio (ζ), it is known that the phase shift transition at ω_n presents a sharper behaviour as damping ratio goes to zero at the expense of having a more oscillatory response. This work aims to exploit this effect, by letting the filter get close enough to instability in order to maximize the region with small phase shift over the filter bandwidth. The following equations give the relationship of the phase shift $\Delta\phi$ at ω_0 with ω_n and ζ.

$$H(s) = \frac{\omega_n^2}{s^2 + 2\zeta\omega_n s + \omega_n^2} \tag{4.3}$$

$$\begin{aligned} \Delta\phi = Arg(H(j\omega_0)) &= atan(\frac{2\zeta\omega_n\omega_0}{\omega_n^2 - \omega_0^2}) \\ \Rightarrow \omega_n &= \sqrt{\omega_0^2 + \frac{2\zeta\omega_n\omega_0}{tan(\Delta\phi)}} \end{aligned} \tag{4.4}$$

A damping ratio of $\zeta \approx 0.2$ allows to reduce the phase shift while providing a good filter response and guaranteeing minimal stability for the system in practice. Thus, a phase shift $\Delta\phi = 10°$ (or $\Delta\phi = 5°$) at $f_0 = 30Hz$ with a second-order low-pass ($\zeta = 0.2$) filter implies a cut-off frequency about $f_n = 2.65.f_0 = 79.5Hz$ (or $f_n = 4.8.f_0 = 144Hz$).

Summarizing, an under-damped second order filter is an efficiently solution in terms of bandwidth (and consumption) to provide an small phase shift over the desired frequency region (QRS_{BW}).

4.3.2 Analog implementation

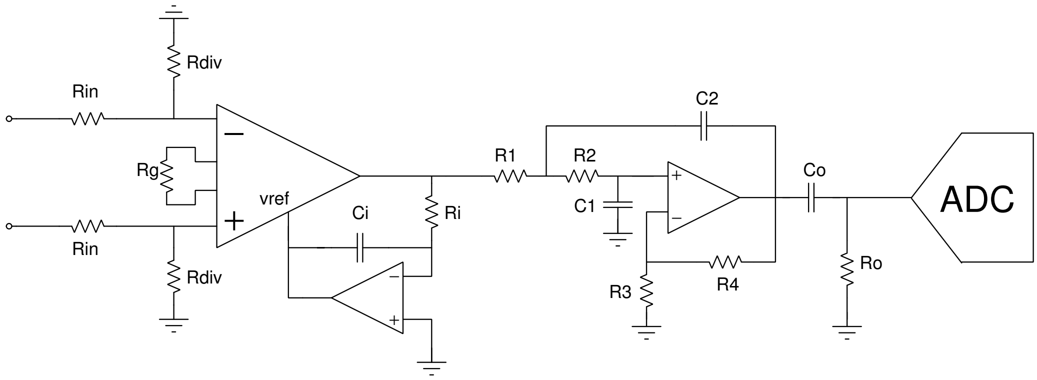

(a) ECG front-end

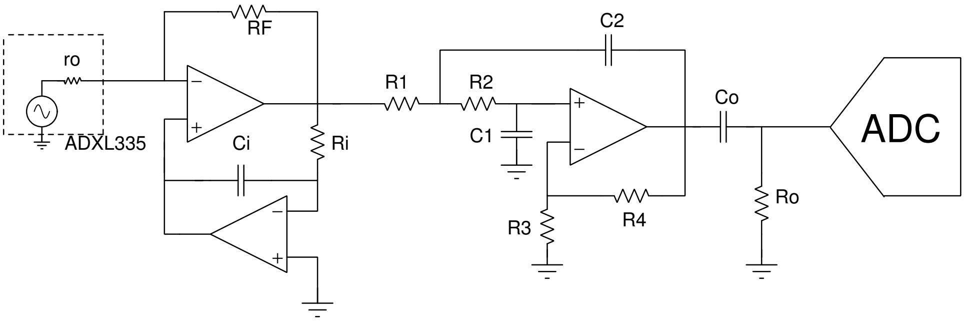

(b) BCG front-end

Figure 4.1: ECG and BCG analog front-ends

The ECG and BCG analog front-ends (AFE) are presented in Fig. 4.1a and Fig. 4.1b respectively. An electrical model of the accelerometer transducer used was also included in the BCG AFE scheme. For the AFE implementation, general purpose operational amplifiers (LM324) were used in traditional filter topologies and an off-the-shelf instrumentation amplifier (AD8226) was used for the ECG pre-Amplifier. Each AFE includes two first-order high pass filters and a second order low pass filter. The first order high pass sections are set more than one decade apart so that there is a dominant high-pass section that sets the high pass cut-off frequency. This dominant high pass filter is set with $\omega_p = \omega_{0HP}/12$ so it is expected to provide less than 5 degrees of phase shift at $f_{0HP} = 6Hz$. On the other hand, the second order low pass filter is designed with ($\zeta = 0.2$) and $\omega_n = 2.66.\omega_{0LP} = 80Hz$, providing a less than 10 degrees of phase shift at $f_{0LP} = 30Hz$. The low pass filter is also used as anti-alias stage suitable for the selected sample frequency $f_s = 250Hz$.

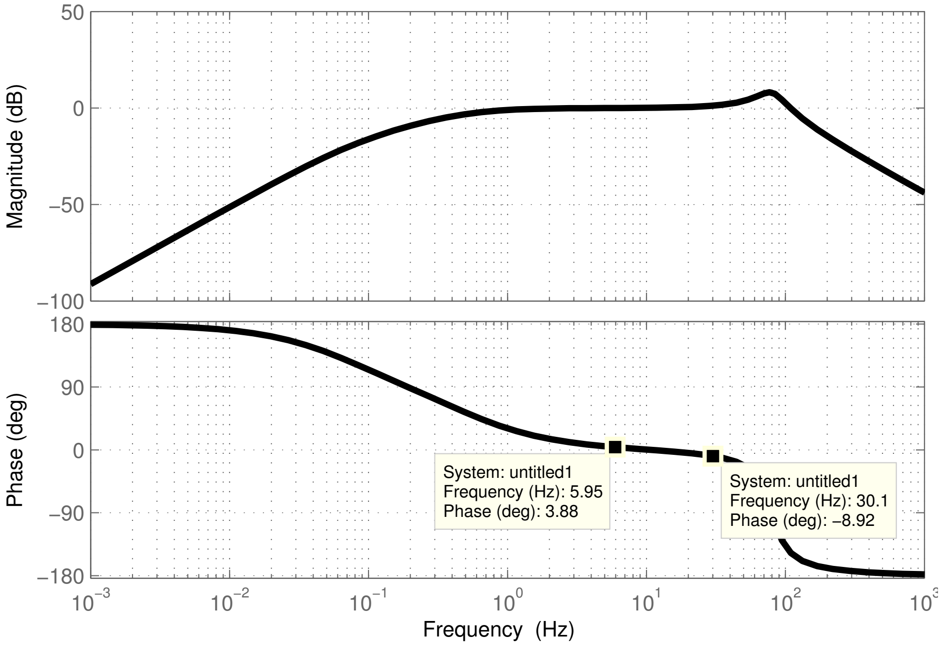

Figure 4.2: Simulated frequency response of AFE filters, showing expected phase shift in the band of interest

Fig. 4.2 shows the simulated frequency response of the filters (equal for ECG and BCG). A phase shift between -8.9 degrees and +3.9 degrees is expected in frequency band of interest $QRS_{BW} = (6, 30)Hz$.

4.4 Digital core

The presented analog filtering is not enough to provide a proper signal conditioning since undesired frequencies still remain. For instance, line frequency was not blocked, and, out of band noise can be suppressed with higher order filtering. Therefore, a Finite Impulse Response (FIR) filter was implemented at the digital domain. The FIR implementation was selected because of its linear phase characteristic, and applied at both signal paths (ECG, BCG) in order to avoid inducing any eventual delay between both signals.

Other issues to be considered here are complexity and consumption, so digital filtering with as few coefficients as possible was considered. Being a FIR digital filter of order N, written in terms of its coefficients (B_n); where the output y_n is obtained from the last N+1 input samples x_n, as stated in 4.5.

$$y_n = B_1 x_n + B_2 x_{n-1} + ... + B_{N+1} x_{n-N} \tag{4.5}$$

Proposed FIR coefficients are enlisted in table 4.1

Table 4.1: Proposed 15^{th} order FIR coefficients.

B_1	-0.016521630237534		B_9	0.327665395670958
B_2	-0.040154744966048		B_{10}	0.226665961705200
B_3	-0.091686037336591		B_{11}	0.059034837616000
B_4	-0.141765076142112		B_{12}	-0.079751120701733
B_5	-0.079751120701733		B_{13}	-0.141765076142112
B_6	0.059034837616000		B_{14}	-0.091686037336591
B_7	0.226665961705200		B_{15}	-0.040154744966048
B_8	0.327665395670958		B_{16}	-0.016521630237534

Fig. 4.3 shows the frequency response of the designed 15th order FIR filter. The proposed filter provides a low pass response with DC attenuation, so undesired components are eliminated at low and high frequencies (i.e., noise, motion artifacts), and its first null in the frequency response was used to filter line frequency (50Hz in this implementation) as a notch filter.

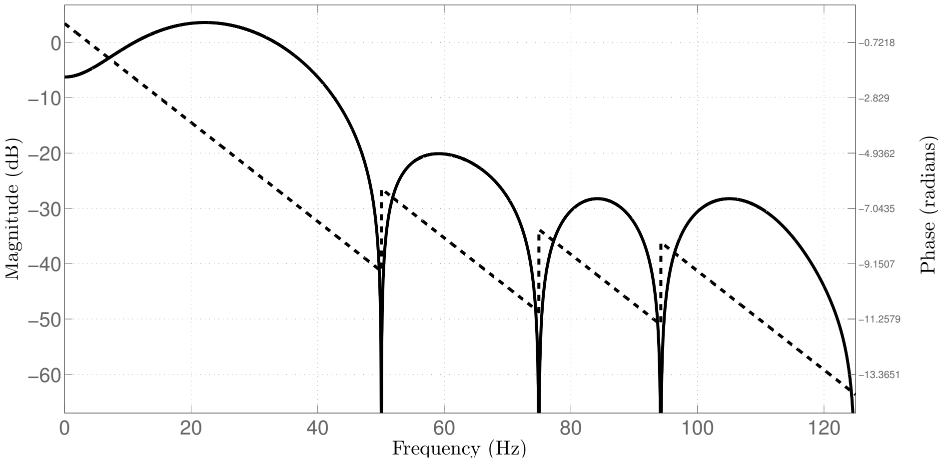

Figure 4.3: FIR filter frequency response

This implementation completes thus, the signal conditioning section, and it is intended to be applied at the end of both signal paths (ECG and BCG). The presented filtering scheme, implemented within one-digital-stage and with relatively few coefficients, presents a deterministic group delay of 7.5 samples (30 ms for $f_s = 250Hz$), which affects equally both signal paths and thus, does not affect PTT estimation.

4.5 Overall phase shifting results

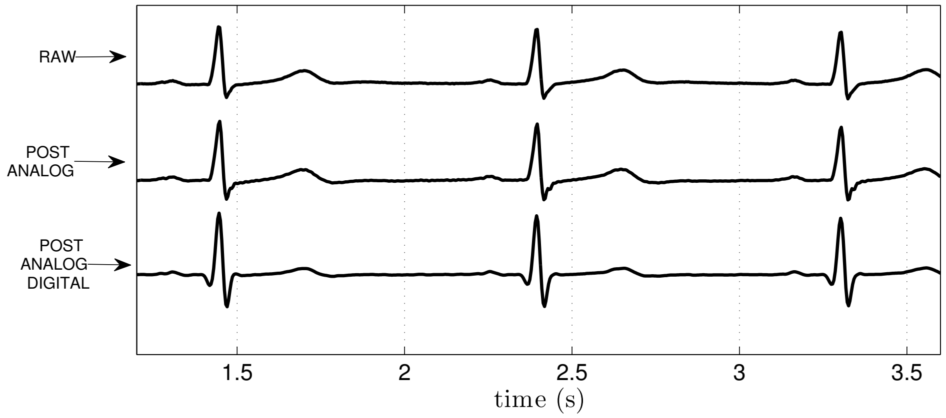

(a) ECG Shifting

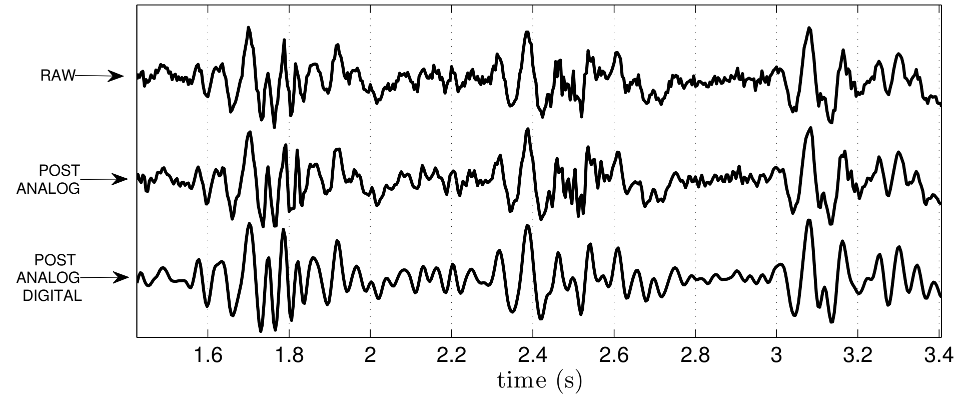

(b) BCG Shifting

Figure 4.4: Simulation of physiological signals phase shifting: Raw, post-Analog, post-Analog and Digital Processing

Fig. 4.4a and Fig. 4.4b show the simulated phase shifting by the proposed signal processing chain when applied to actual acquired raw ECG and BCG signals. The simulation shows that no significant delay is generated as the signals are processed in the chain from the raw signal through post-analog and post-digital processing. The post-digital line results were moved backward 7.5 samples suppressing the constant delay of the digital signal processing. Overall phase shift along the complete processing chain corresponds to a timing error of less than 2ms, which is negligible regarding the estimated values of PTT, which are around 100 ms, and the time quantization uncertainty.

4.6 Wearable device prototype

The proposed signal conditioning scheme was implemented in a device prototype to be tested in a real wearable application (photos shown in Fig. 4.5).


(a) Close up (b) Device testing

Figure 4.5: Photos of wearable device prototype

Fig. 4.6 summarizes the wearable device hardware in a block diagram. The device contains a custom printed circuit board (PCB) including a longitudinal, head-to-foot, accelerometer (ADXL335), front-end analog signal processing for BCG and ECG, and a Bluetooth Low Energy module for signal acquisition and transmission to an external computer.

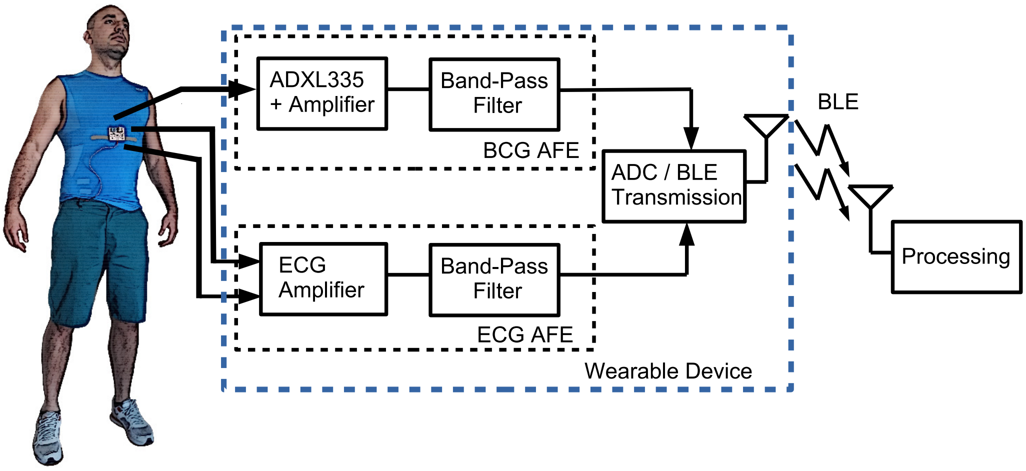

Figure 4.6: Custom Made Wearable Device Block Diagram

The PCB was designed to be electrically and mechanically coupled to a training shirt that features dry electrodes at the chest region. ECG and BCG conditioned signals are acquired at 10bits, $f_s = 250Hz$; and, transferred wirelessly to a remote PC where digital processing occurs. A Python script was written to receive signals, apply digital filters, find ECG R wave and BCG J wave (through a simple peak algorithm based on seeking for peaks in an adequate time-window),compute the beat-to-beat PTT, and display signals in a real-time basis.

4.7 Results

Fig. 4.7 shows the signals acquired by the wearable prototype as displayed on screen after the complete processing chain is performed. The subject was asked to relax in a sitting position during the acquisition and the PTT was almost constant at about PTT=112 ms.

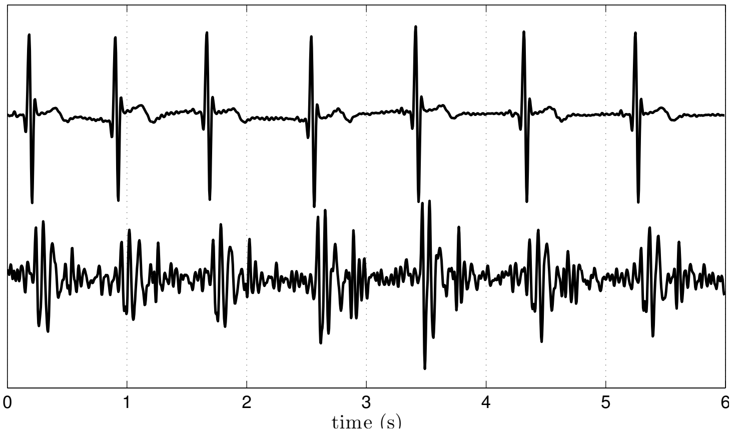

Figure 4.7: Signals acquired by wearable device

In order to show a dynamic PTT acquisition, the volunteer was asked to do push-ups repetitions until muscle fatigue to produce an hemodynamic fluctuation. Immediately after the strength manoeuvre was finished, a series of readings was collected with the prototype device. Fig. 4.8a shows the on-the-fly computed PTT which increases approximately from 85ms to 110 ms in a 8 minutes lapse. A moving-average filtered PTT (ten samples) was also superimposed on figure to show the mean signal trend. Fig. 4.8b (Fig. 4.8c) shows the ECG R wave (BCG J wave) phase shifting through the proposed conditioning chain. Finally, less than 2ms of phase lagging error is reached along the complete trial (Fig. 4.8d). The validation of this set-up for CABP estimation from these ECG and BCG wearable recordings are further studied in chapters 6 and 7.

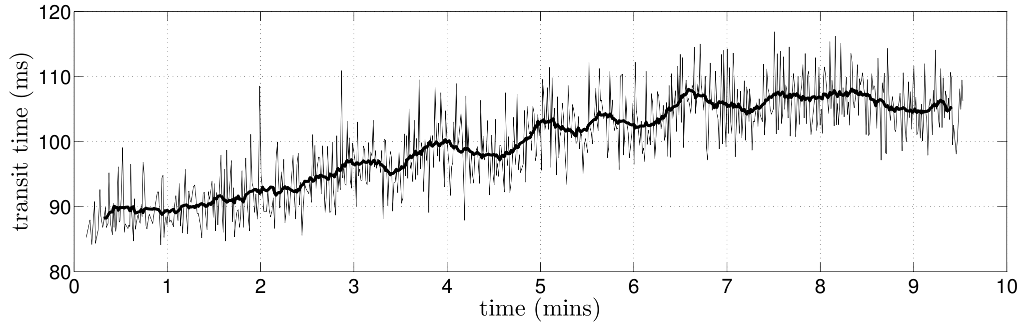

(a) PTT evolution after strength manoeuvre

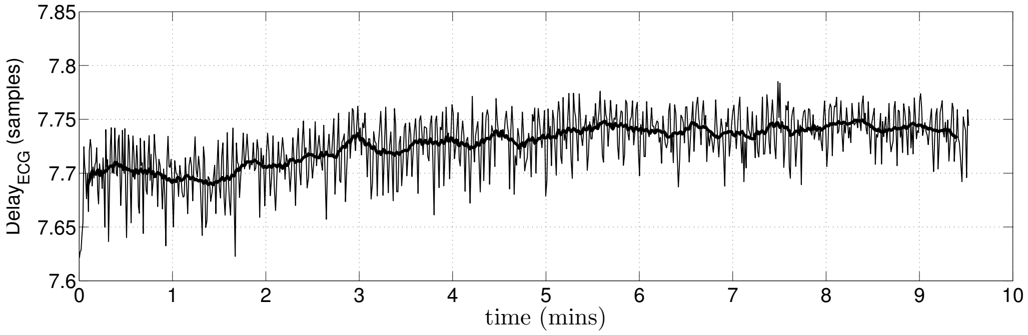

(b) ECG R wave phase lagging (due to filtering) expressed in samples ($T_s = 4ms$) during the trial. Digital introduces a 7.5 samples delay.

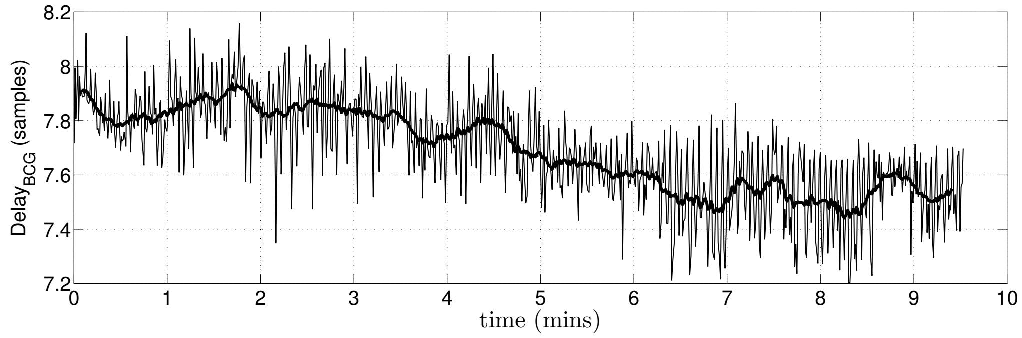

(c) BCG J wave phase lagging (due to filtering) expressed in samples ($T_s = 4ms$) during the trial. Digital introduces a 7.5 samples delay.

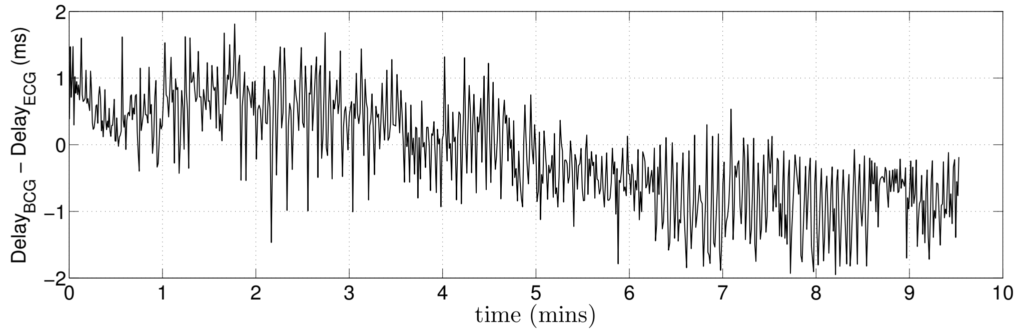

(d) PTT phase lagging error (due to filtering) during the trial.

Figure 4.8: PTT estimation by wearable device after strength manoeuvre and phase lagging induced on signals

4.8 Conclusions

When estimating pulse transit time, the timing error introduced by the signal processing chain must be taken into account, especially if featured times are required to be accurate and absolute (i.e., with no offsets corrupting the FT due to delays at acquisition). For instance, in chapter 8, it is developed a novel PTT based model (PTTBM) to estimate central aortic BP from few FTs (derived from the ECG and BCG acquisition). Proposed PTTBM is firmly based on physics near the heart, and consequently, its proper application depends on keeping the physics on its input magnitudes unaffected; the addition of delays with no physical sense certainly degrades the model accuracy/convergence. In this sense, conditioning chains must preserve the timing references unaffected, and this is the case for this proposed methodology. The simplicity of the design, which optimizes the filter parameters without adding additional components or stages, suits the low power and size needs of wearable applications. Simulations and measurements show that a spurious timing error, which is negligible (less than 2ms) in the context of the considered application, can be achieved. The designed wearable device features the proposed technique for the proper PTT acquisition. Its design and experimental results, including real-time ECG and BCG signal acquisition, and PTT estimation, are reported.

Chapter 5

Wearable Device: Conceiving an Integrated Version

Rationale

A novel methodology for the pulse transit time (PTT) acquisition was presented in the last chapter. Measurements with a wearable prototype demonstrated that a neglectable error at the PTT computation could be achieved, and thus, the proposed method contributes to the conception of hardware suitable to BP estimation based on PTT acquisition. In order to provide the methodology with higher autonomy and integration, a highly miniaturized implementation of the filtering approach was also proposed. An integrated ultra-low-power (ULP) version of the previously presented filtering scheme is proposed in this chapter. Simulation results showed that less than 2ms delay for the QRS complex of the Electrocardiogram (ECG) could be achieved with a total current consumption of $I_{DD} =$ 2.1nA at V_{DD}=1.2V of power supply. Given that integrated circuits are subject to a significant deviation on component parameters, and the proposed filtering scheme requires precise filtering parameter selections, this performance is based on the filter transfer function selection from a novel gm-C architecture and tuning procedure.

Even though this chapter is centered on the ultra-low-power filter block, in order to provide the context of its application, the proposed filter was included in the signals path chain of a complete analog front-end (AFE) suitable for the low-delay electrocardiogram (ECG) and ballistocardiogram (BCG) acquisition. Noteworthy, the material is presented focusing on the ECG signal path filtering, but the concepts were analogously applied for the BCG branch since, as was mentioned in 4.2, the average spectral support of both signals was considered approximately the same. Additionally, complete AFE was fabricated in a CMOS process with a 130nm technology node whose main objective was to integrate an AFE as complete as possible; that is, the chip would provide all the needed circuitry for the proper PTT acquisition while seeking for adding as few external blocks as possible. In this sense, besides of being fully-integrated, the proposed filter architecture and design aim to include novel solutions for facing issues typically found in the ULP IC design domain; such as large and well-controlled on-chip time-constant creation for filtering, on-chip generation of pico-Ampere current references, ULP voltage referencing, and mechanism for tuning internal currents. The chapter is organized as follows: section 5.1 briefly presents the integrated AFE, its context acting in a wearable device, the top level view and the key internal blocks are introduced. Section 5.2 presents the gm-C architecture where novel dc-attenuation and tuning features are highlighted; an algorithm for tuning is also presented along with the criteria adopted to design the part. Then, section 5.3 presents the biasing section of the AFE/Filter and the implementation of the tuning feature. Results of experimental characterization of the fabricated chips are shown in 5.4. Finally, discussions and conclusions drawn in section 5.5.

5.1 The analog front-end (AFE)

Fig. 5.1 shows the block diagram scheme of the wearable CABP monitoring device presented in the last chapter but, by using the proposed AFE IC at the conditioning chains. Ballistocardiogram (BCG) and electrocardiogram (ECG) are the two physiological signals that might serve as biological input to estimate central aortic blood pressure (see chapter 3). Each signal path features analog conditioning and bandwidth limiting stages to prepare signals to be digitalized, and then, to be transmitted (wirelessly) to an external computer for further processing as shown in the previous chapter. Proposed AFE IC is denoted inside the fine-dashed box in the context of the wearable implementation, and, a novel ultra-low-power filter is also denoted in the figure 5.1 as part of the AFE.

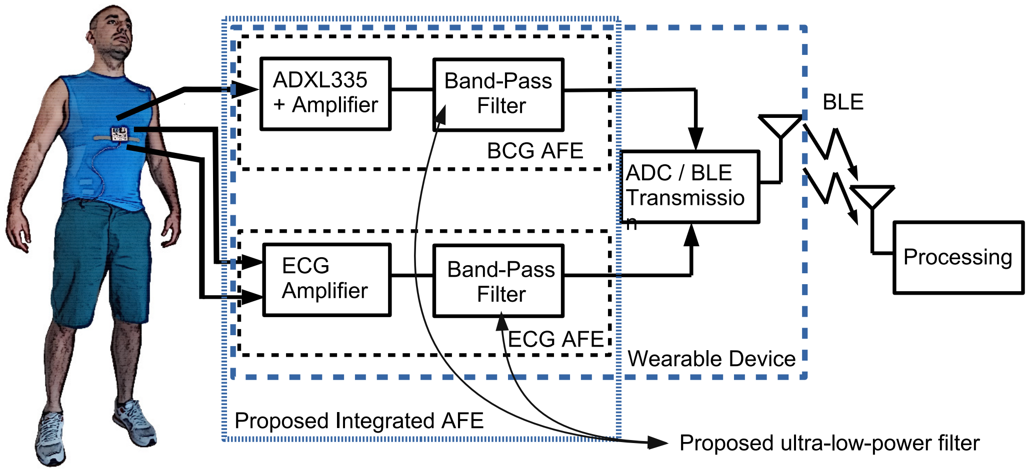

Figure 5.1: Scheme of the proposed blood pressure monitoring device

5.1.1 The technology

The whole AFE IC indicated in Fig. 5.1 was fabricated in the GlobalFoundries GFUS-8RF 130 nm CMOS Technology.

The technology features low power (LP), low threshold voltage (Low-Vt), zero threshold voltage (Zero-Vt), and standard metal oxide transistors (MOS) devices with n-type-channel (NMOS) and p-type-channel (PMOS) characteristics. All the presented designs in this chapter use LP MOS devices, and unless stated otherwise, all LP devices have their bulk terminal tied to GND for the NMOS, and to Vdd for the PMOS. Where GND (also referred to as Vss) refers to the negative terminal of the power supply, and Vdd stands for the positive one. The technology is characterized for operating with a Vdd=1.2...1.5V and, most discussed circuits are intended to operate for a Vdd=1.2V. However, as will shown, on-chip generated current reference (Iref, see section 5.3.1) might achieve better yields by operating at Vdd=1.5V. GlobalFoundries GFUS-8RF technology kit for the 6.1 version of Cadence electronic design automation (EDA) tools was used for the presented simulations with the Virtuoso Spectre Circuit Simulator L and XL tools.

5.1.2 AFE top level

Fig. 5.2 shows the top level view of the proposed AFE IC. Main Blocks are presented briefly in this section.

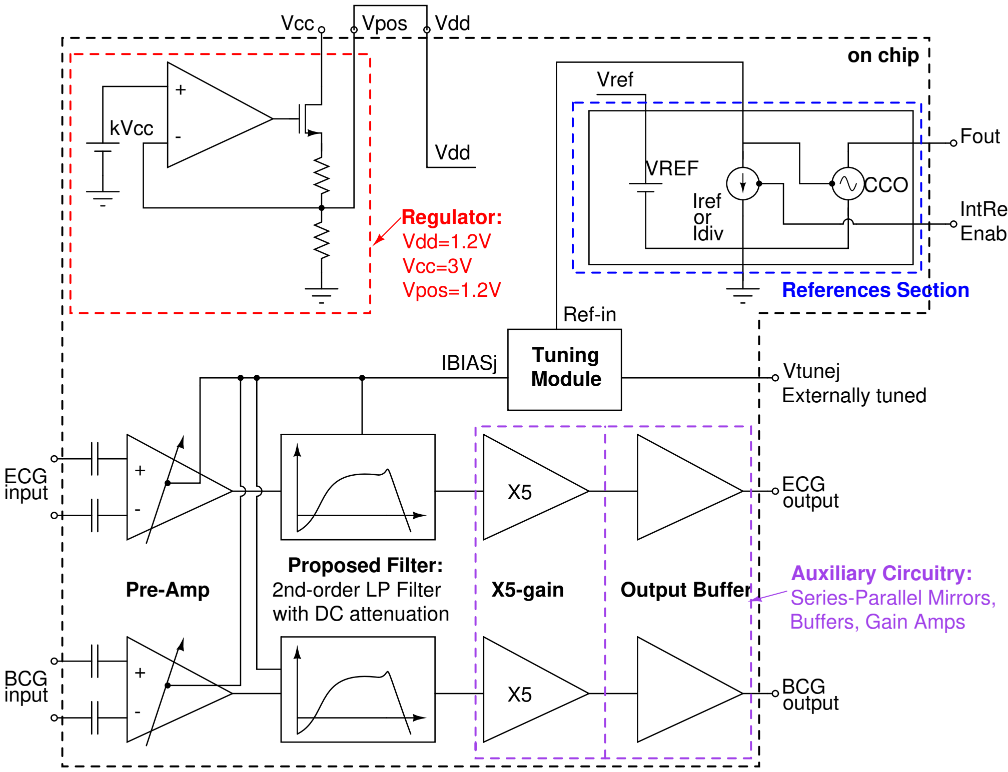

Figure 5.2: Top level view of the Analog Front End Integrated circuit

Signal path:

Each signal path (ECG and BCG) features a pre-amplifier block and the proposed tunable 2^{nd}-order low pass filter with DC attenuation (sec. 5.2) as the ultra-low-power section of the signal path. The signal path chain continues with more standard (by-the-book designs) blocks, which are not intended to achieve high-performance specs but to provide the auxiliary functionality to make possible the proper operation of the whole system. These are, the x5-gain block that provides the signals path with a further gain (5 V/V) while alleviating the linearity specification of the previous block; and the Output Buffer that was designed to drive the chip output and the eventual ADC input properly. Even though ECG second-order filter is the central block presented in this chapter, the same design considerations were applied for the BCG filtering. In effect, as was previously mentioned, and inherited from the previous chapter, both signal path were designed to implement the same filtering from a frequency response perspective and, signal path only differs on the pass-band gain to given to the signals. The design of pre-amplifier block along with signal path auxiliary circuits were not included in this document.

Voltage regulator:

As was previously mentioned, this IC design pursued an implementation that minimized the need for external blocks. Given that the wearable device was intended to be powered from a Vcc=3V CR2031 lithium battery, the IC should provide its power supply from there. Therefore a linear regulator was included in the AFE to provide from Vcc (k-factor in Fig. 5.2 from a voltage divider technique similar to the included in sec. 5.3.5), the power supply VPOS (1.2V) for the auxiliary circuits, and the Vdd for the ultra-low-power designs. The regulator is not described in this chapter.

References section:

The reference section will be further discussed in the following (sec. 5.3) since it is strongly related to the proposed filtering approach. This section introduces novel ultra-low-power designs which serve for biasing the AFE, particularly, the proposed filter. The section includes a Internal DC Voltage reference (Vref=600mV), currents references (Idiv=30/60pA, Iref=60pA, Ibias=30pA) and, a Current Controlled Oscillator (CCO) designed for measuring such small bias currents [75].

Tuning module:

The proposed filtering approach requires a very controlled damping ratio and cut-off frequency to achieve the desired low-delay at narrow bandwidth filtering. The tuning module provides the mechanisms for achieving such particular filtering despite the variability of the fabrication process. The module tunes each particular I_{BIASj} by controlling externally the voltage at inputs Vtunej as will be further detailed in section 5.3.4.

5.2 Ultra-low-power integrated filter

Objective: Implementation of an integrated version of the filtering scheme presented on chapter 4

The proposed filtering scheme developed in the previous chapter requires a precise and accurate filter parameter selection in order to produce low phase lags on biomedical signals in a reduced bandwidth. An integrated implementation of such proposed under-damped filtering scheme might be provided from different techniques available in the literature [76] [77] [78]. In general, the conception of circuits with very low cut-off frequencies might not be an easy task to implement on-chip. That is, low-frequency filtering accordingly requires the on-chip implementation of large time-constants ($\tau = RC$); notably, a τ in the order of 0.01..10 seconds would be needed for this biomedical application. Whereas, on-chip capacitances and resistances are limited to tens of pF and MΩ, respectively; higher valued components will not be integrable on the chip area.

Relatively large time-constants as long as reliably and repeatably for filtering might be achievable by using discrete-time structures, and thus, it is why the switched capacitor technique is widely encountered at conditioning stages in biomedical acquisition systems [78]. Nevertheless, such structures require the implementation of its respective sampling clock reference, which adds an avoidable circuitry design if there are no other circuits (in the chip) utilizing/sharing such timing references (e.g., Analog-to-digital converters, wireless communication or digital core). Further, required clocked references must be precise and/or well-matched with other devices, [78] in order to reach the accurate filtering needed by this application. Additionally, when using such discrete-time structures for biomedical filtering, filter reference frequency must be as high as several kHz to satisfy anti-aliasing restrictions, and such switching rate increases the dynamic consumption, thus compromising the ultra-low-power characteristic for the filter design.

On the continuous-time IC-design side, the operational transconductance amplifier Capacitor (OTA-C) or Gm-C technique might offer an alternative for implementing the required low-frequency filtering. Since large resistors are impractical to implement on-chip, such a role could be fulfilled by transconductances devices along with techniques to reduce its effective gain (Gm) [79]; such an approach might lead to achieving large on-chip time constants. Effective gm values of a MOS device (the core of OTA structure, then Gm could be proportional to gm), can be reduced by using a bulk-driven operation rather than the typical gate-driven one [80] [81]; the technique also might be suitable for low voltage design since it reduces the threshold voltage and facilitates low voltage operation [82]. Nevertheless, such an approach might not offer benefits for this design, since the chosen technology features Low-Vt and Zero-Vt MOS devices yet, and still, it is not intended an ultra-low voltage operation for this design (in the meantime). Also, bulk-driven devices might show linearity issues at sub-threshold currents due to the leakage, mainly affecting current mirror stages. Otherwise, the current splitting technique [83] is also utilized to reduce the effective Gm of the OTA, but the technique is based on draw current to decrease Gm, which is in the opposite direction respect the low power design.

The OTA with MOS devices operating in the deep sub-threshold region is a power-efficient solution aligned with the autonomy required by this application. Notably, the proposed filter presented in this section exploits the sub-threshold region of the MOS devices in order to achieve the required very low transconductance. Eventually, such OTA operation might be affected by linearity issues, whereas active source degeneration technique with transistors [84] offers a simple solution to improve the linearity in the transfer characteristics of the OTA devices, even operating at deep sub-threshold region. Additionally, MOS devices at such inversion levels present an almost constant transconductance over drain current ratio $g_m/I_D \approx 1/nU_t$ (where U_t is the thermal voltage, n is the slope factor). The proposed method exploits such feature in order to tune the g_m of MOS devices (and thus, the G_m of the OTAs) by means of tuning ultra low currents.

OTA current tuning could be provided by automatic tuning techniques [85] in order to achieve the target τ of the desired frequency response [69] automatically. Nevertheless, such a tuning approach, besides increasing the circuit complexity and requiring a very precise external timing reference [85], would leave the damping ratio setting, which is required to be precisely set, liberated only to the matching quality between devices through the layout techniques. Such an approach may not be sufficient for this application. A classic biquad topology [86] was selected so that parameters (time constant, and damping ratio) could be easily tuned by modifying biasing currents at individuals sub-blocks. Additionally, in order to improve the suitability of the classic biquad filter into the proposed analog front-end, some modifications to the classic structure were performed; as a result, a novel architecture which implements a second-order low-pass filter with DC attenuation and tuning capabilities is proposed in this section.

5.2.1 Architecture and design

Proposed filter is the bandwidth-limiter section of the analog front-end for the ECG and BCG signals acquisition. In this context, the filter is located after the pre-amplification stage (see fig. 5.1) and, besides filtering, the biquad block also provides (variable) gain at each signal path. Notably, ECG filter design is presented in this document, the same was applied for the BCG channel in this design; but also, the concepts involved could be extended to other physiological signals to minimize phase lags at acquisition.

The band of interest for detection of the ECG-QRS complex QRS_{BW} is from 6 to 30 Hz [72] [73]. The design criteria proposed in [87] was to minimize any eventual phase shift at such band for the ECG conditioning chain. Design presented here, similarly to the previous chapter and in [87], exploits the underdamped filter characteristics to provide the solution. In particular, a damping ratio of $\zeta = 0.25$, natural filter frequency of f_n= 100 Hz was the target in this work to minimize the phase shift in the QRS complex frequency band, while providing a variable

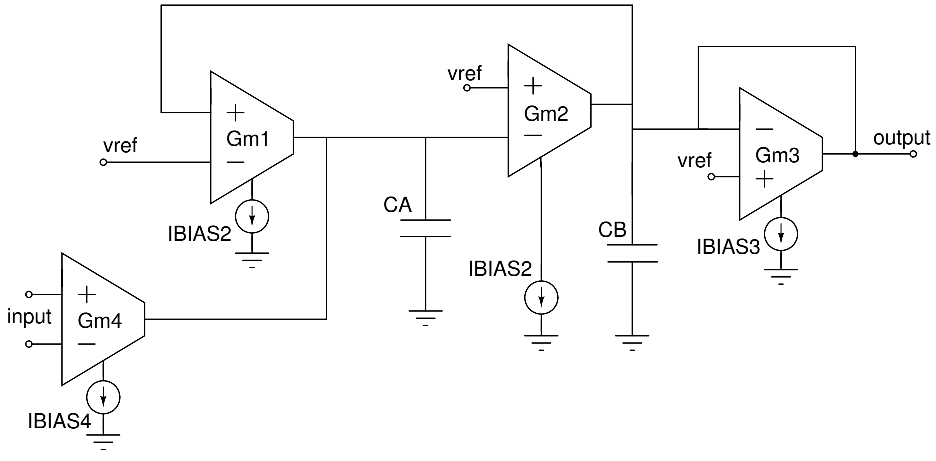

Figure 5.3: Classical biquad Implementation [86]

in-band Gain.

5.2.2 Classical biquad implementation

Filter architecture is based on a classical biquad implementation [86] which implements a second order low-pass filter as shown in Fig. 5.3.

The transfer function of this biquad is given by 5.1. The natural frequency (ω_n) and damping ratio (ζ) of the second order low-pass filter are given by 5.2-5.4.

$$H(s) = \frac{\frac{Gm_4}{Gm_1}\frac{Gm_1 Gm_2}{C_A C_B}}{s^2 + \frac{Gm_3}{C_B}s + \frac{Gm_1 Gm_2}{C_A C_B}} \tag{5.1}$$

$$Gain = \frac{Gm_4}{Gm_1} \tag{5.2}$$

$$\omega_n^2 = \frac{Gm_1 Gm_2}{C_A C_B} \tag{5.3}$$

$$\zeta = Gm_3\sqrt{\frac{C_A/C_B}{2Gm_1 Gm_2}} \tag{5.4}$$

5.2.3 Proposed biquad architecture

Classical biquad implementation was modified (Fig. 5.4a) as follows. Firstly, a loop through Gcm, Ccm and the DC_cont input of Gm4 is added. This loop implements the high pass characteristic and provides DC-attenuation to alleviate the effect of the preamp and filter DC offsets. Secondly, Gm2 is simplified, in order to save consumption to a source follower, as discussed later. Additionally, regarding the system level implementation, filter is preceded by the pre-amplifier block with a fully-differential architecture, and, followed by the single-ended input 5X-gain block. Consequently, a differential-to-single ended filter is the needed structure by the overall implementation.

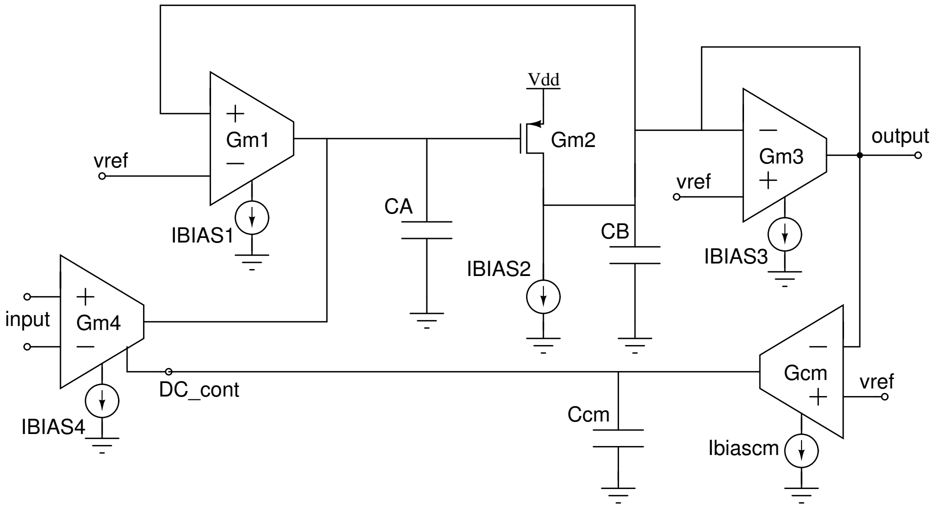

(a) Proposed circuit: top level view

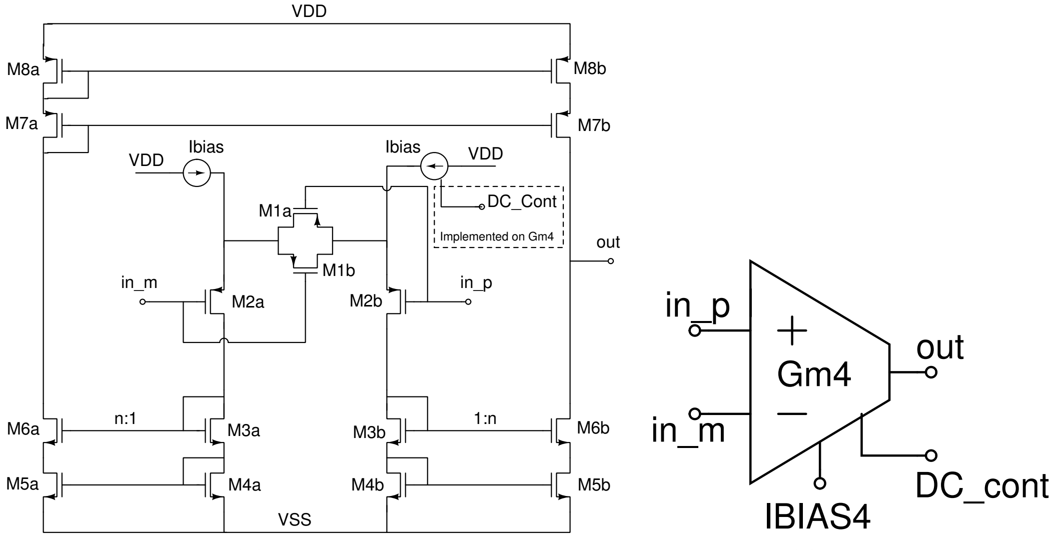

(b) Schematic (c) Symbol

Figure 5.4: Proposed circuit and transconductors implementation. Ibias current sources shown in (b) are mirrored from the bias current injected in the I_{BIAS4} input of (c). Gm4 also includes the DC_cont input that changes the ratio between the current injected in the Ibias input and the current of one of the Ibias current source that is internal to the transconductor as shown in (b). The implementation of such voltage-controlled current source will be shown in section 5.3.4

Ultra low power implementation and tuning

Target consumption was only few nano-amperes, consequently, differential pairs of the transconductance blocks were biased with only hundreds of pico-amperes. At such biasing levels, CMOS devices operate in deep weak inversion region where g_m/I_D values are confined to be close to $g_m/I_D \approx \frac{1}{nU_T}$. Therefore, such almost linear transconductance-bias behaviour gives an approximately linear tuning of the transconductance by tuning the bias current; I_{BIASj} will be the used nomenclature for referring to the different G_{mj} biasing currents in this chapter. The I_{BIASj} were adjusted from 10% to 120% of its nominal value by a tuning procedure (section 5.3.4) for each individual current. Then, filter parameters as, gain, bandwidth and damping ratio are adjusted at will by tuning bias currents properly as (5.2)-(5.4) suggest.

Circuit and dc-attenuation Loop

Fig. 5.4 shows the proposed architecture where G_{m1}, G_{m3}, G_{m4} and G_{cm} were implemented with the structure of Fig. 5.4b. G_{m4} includes an input for bias current tuning (DC_cont) shown in the dashed box at Fig. 5.4b, while G_{m1}, G_{m3}, and G_{cm} do not include it. The first novel approach is that the dc attenuation at the output is implemented by the feedback loop from the output, through G_{cm} to the DC_cont input of G_{m4}.

The second novel approach lies in implementing G_{m2} with a simple common source structure (Fig. 5.4a). This is due to the low amplitude at the input of G_{m2} (internal node of a fed-back structure with gain) which avoids the need for a transconductor with higher linear range.

5.2.4 Tuning algorithm

The filter specification requires a very well-controlled set of parameters (*Gain*, ω_n and ζ) due to the variability of CMOS process. This is achieved through a tuning procedure as follows (illustrated in Fig. 5.5). This tuning procedure is implemented off-chip.

- ***Gain:*** Starting from an initial (seed) value of G_{m1}=G_{m1o}, G_{m4} is tuned, through Ibias4 (Fig. 5.4a), to satisfy the *Gain* specification (5.2). If the desired *Gain* cannot be achieved within the tuning range, G_{m1} could also be modified conveniently to reach it.
- ***Natural frequency:*** G_{m2} is adjusted to reach the desired peaking frequency which is related to ω_n (5.3).
- ***Damping factor:*** G_{m3} is adjusted to reach the desired peaking amplitude, which is related to the damping factor ζ (5.4).

As was previously mentioned, a damping ratio of $\zeta = 0.25$, natural filter frequency of f_n= 100Hz was the target in this work to minimize the phase shift in the QRS complex frequency band, while providing a variable in-band *Gain*.

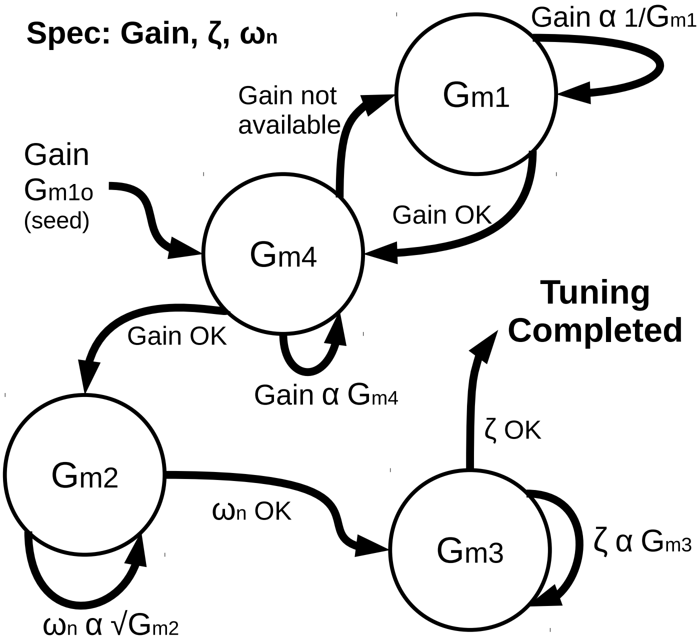

Figure 5.5: Tuning Algorithm.

5.2.5 Results

Circuit design was performed using Cadence EDA Tools for nominal and corner simulations. Table 5.1 presents final design parameters of the filter to achieve a damping ratio of $\zeta = 0.25$ at f= 100Hz with an in-band $Gain$=12dB. The total consumption achieved was Idd=2.1 nA for a Vdd=1.2 V. The equivalent input noise was 0.38 mVrms showed a reasonable noise for a second stage block since the reference value for the ECG input at pre-amplifier block was in the order of 1 mVrms. Whereas, the BCG expected input reference value for BCG signal is more than ten times higher.

Table 5.1: Filter parameters

Block	Value	I_{DD}
G_{m1}	1 nS	320 pA
G_{m2}	4.5 nS	170 pA
G_{m3}	1.5 nS	460 pA
G_{m4}	4.7 nS	960 pA
G_{cm}	0.13 nS	122 pA

Cap	Value
C_A	1.9 pF
C_B	4.4 pF
C_{cm}	20 pF

Frequency response

Figure 5.6 shows the simulated gain amplitude and phase-frequency response of the filter. By letting the filter get close enough to instability, the phase shift over

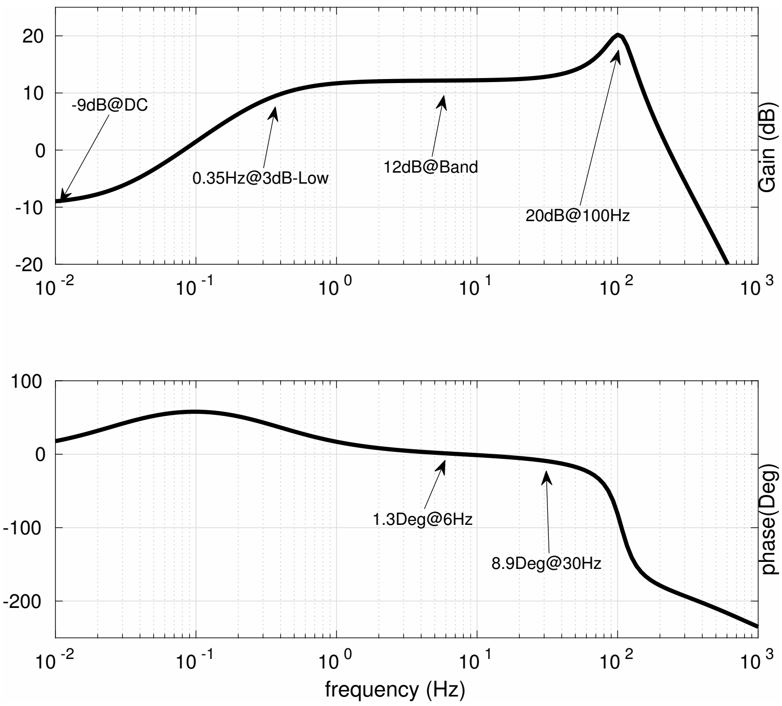

Figure 5.6: Frequency response of the tuned filter.

the region of interest is minimized. Phase shift varies only 10 degrees in the 6 to 30 Hz region, in spite that the overall bandwidth is only about 100Hz, which allows reducing consumption and noise. Additionally, the filter features more than 20dB of dc-attenuation. A high pass cut-off frequency as small as 0.35 Hz is reached by design. The proposal decreases the usual stability margins in order to minimize phase lag. This will lead to slightly increased ringing, which is an acceptable cost for having a much better phase lag performance. As shown in the next sub-section, the resulting transient response is fully adequate for the application.

Transient response

In order to show the performance of the technique from a low QRS delay perspective, an acquired ECG signal (from the wearable device presented in the previous chapter) was filtered by the proposed circuit. A 50-beat ECG recording was modeled as a piece-wise linear voltage source in a transient simulation. The beat-to-beat QRS delay between filter input and output was automatically measured by the simulator. QRS complexes were delayed less than 2ms over the hole 50-beat recording. Figure 5.7 shows such simulation for two cardiac cycles, and depicts qualitatively that no significant delays are generated by the proposed approach.

In order to show more closely the improved delay performance of the proposed circuit it is compared with the case of an ideal second order low pass filter implemented with two identical first order stages in cascade. All signals were normalized to have the sample peak amplitude; and both, proposed and ideal filtering struc-

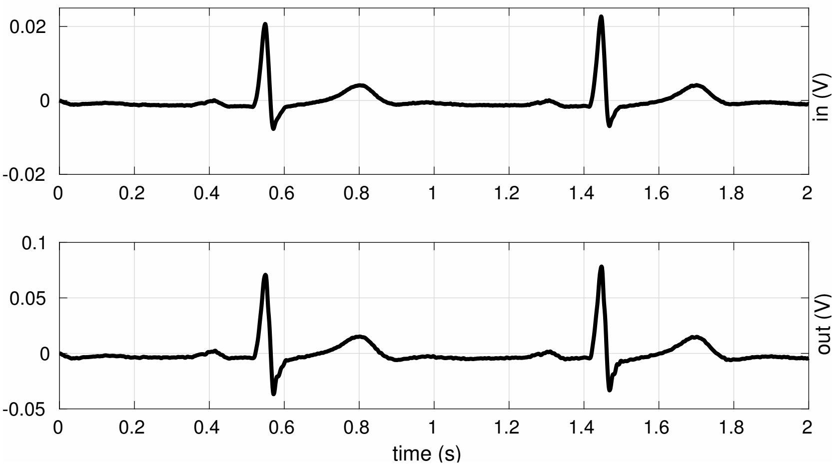

Figure 5.7: Acquired ECG signal processed with the proposed filter. Input and output voltage are displayed

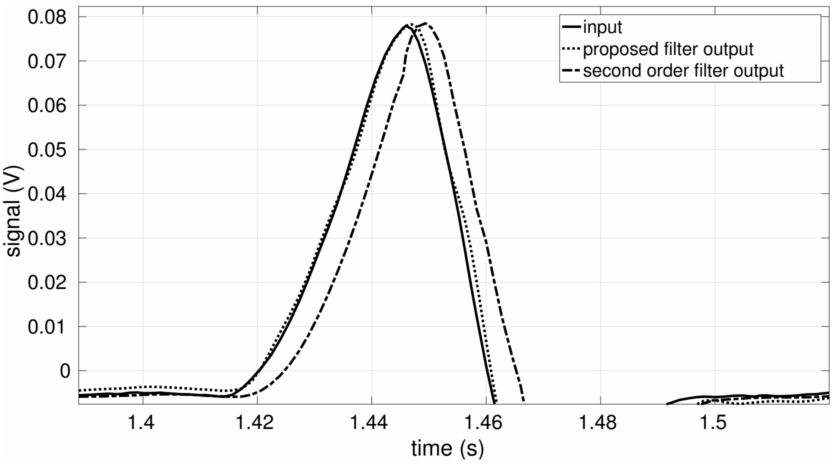

Figure 5.8: Closer view of the aquired ECG R-wave (continuous trace) as input signal. ECG R-wave filtered by the proposed circuit (short dashed trace) and by two identical first order low pass stages in cascade(long-short dashed trace). Both filtering structures have the same equivalent bandwidth.

tures have the same equivalent bandwidth. Fig. 5.8 shows an R-peak filtered by the proposed circuit and by the ideal filter. The proposed filtering scheme produces a delay almost 4 times smaller than the produced by the ideal structure.

Tuning performance

In order to show the feasibility of the proposed tuning method, the filter was tuned for each of the process corners of the CMOS technology used. Fig. 5.9a shows the filter frequency response from a corner analysis at nominal biasing and no tuning performed. Although, all curves show large variability on the three characteristics (in-band Gain, natural frequency, evidenced in the peaking frequency,

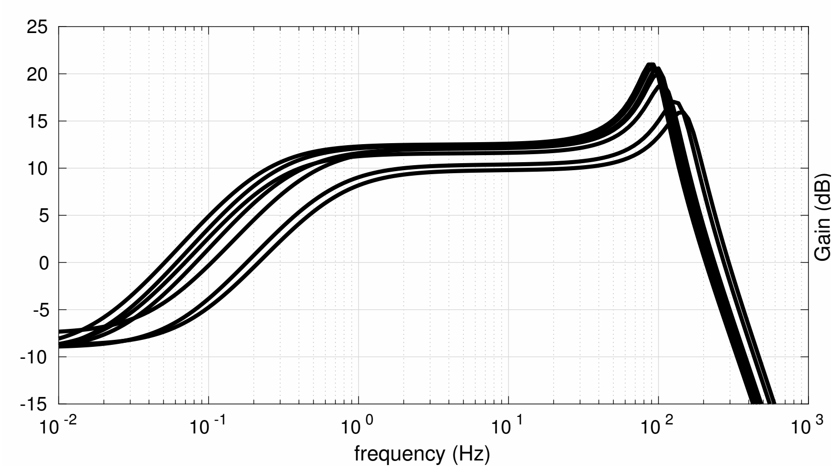

(a) Before tuning

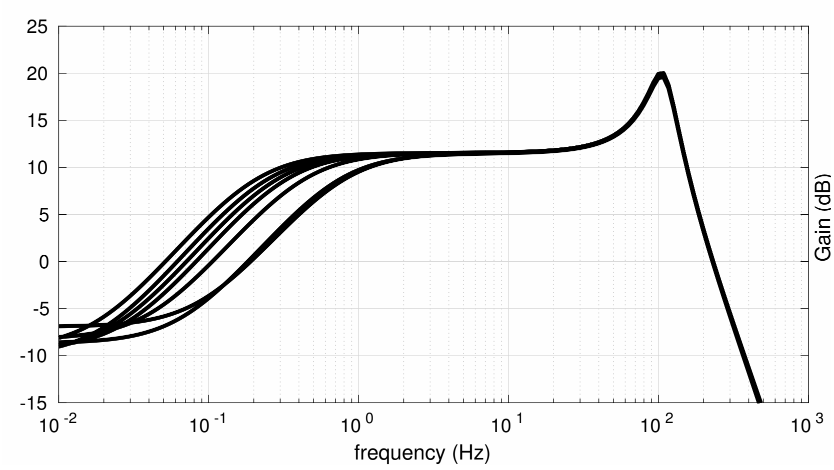

(b) After tuning

Figure 5.9: Frequency response over technology corners.

and damping factor, evidenced in the peaking amplitude), all curves can be successfully tuned. Every corner run was subsequently tuned with the algorithm presented in section 5.2.4, with Gain=12dB, peaking frequency=100Hz, peaking amplitude=8dB as target. In such proceeding, biasing currents were adjusted from 10% to 120% of its nominal value by an external block. Fig. 5.9b shows the corner frequency responses after the tuning procedure. The tuning procedure allowed to reach a very low spread of the frequency response in the band of interest, further, the tuned low-pass filtering is almost the same for all corners. The bias current values after tuning are shown in Table 5.2. The nominal bias current corresponds to 100%. Some bias current are tuned below 100% in all corners (such as Ibias4) because the target tuning specification was different from the initial design specification. In the case of Ibias4, for instance, it was set a gain target for tuning higher than the initial specification. Finally, the frequency response after tuning presents larger variability at frequencies below the band because the dc-attenuation path was not tuned. Monte Carlo simulations were also performed (over process and mismatch) showing that variability did not lead to the occurrence of unstable responses (checked both in the frequency response and in the transient response). Furthermore, the parameter-tuning capabilities would allow to compensate a potentially unstable unit.

Table 5.2: Bias currents (I_{BIASj}) resulted after the tuning procedure performed for each corner of the technology in order to obtain the desired filtering. Respectively I_{BIASj} values at each corner are written as percentages of their nominal value, which are indicated at the *100%* row.

	I_{BIAS1}	I_{BIAS2}	I_{BIAS3}	I_{BIAS4}
100%	30 pA	60 pA	30 pA	60pA
tt	73 %	92 %	83 %	39 %
fff	33 %	83 %	11 %	34 %
ssf	87 %	108 %	103 %	46 %
fs	100 %	71 %	77 %	55 %
sf	100 %	69 %	44 %	59 %
ff	73 %	68 %	13 %	52 %
ss	100 %	86 %	85 %	54 %

5.3 References section

Presented filtering scheme proved to be a suitable solution for a narrow-band and low-delay filtering of the ECG QRS complex. Nevertheless, at this point, the required tunable pico-Amps biasing (table 5.2) of the structure emerges as a new problem to be addressed. In this sense, two major difficulties are encountered. Firstly, the efficient generation of biasing currents in the order of pico-Amperes, that is, filter design is tuned from their nominal I_{BIASj}= 30/60 pA, and such nominal currents must be generated in some way; and, the generation of a voltage reference (sourcing the node vref at Fig. 5.4) which also should feature ultra-low-power characteristics to maintain the consistency of the design. Then, and critical for the proposed low-delay filtering scheme, to provide the mechanisms for precisely tuning I_{BIASj} currents to reach the values showed at table 5.2 (written in rows as percentages of its nominal values at second row). Integrated circuits are subject to a significant spread on component parameters which defines the biasing, and so the filtering. Featuring the design with a proper tuning module may lead to achieve the needed frequency response despite of technology process as showed in section 5.2.5. This section presents the solution for the pico-Amps bias generation (sections 5.3.1 for the on chip solution and 5.3.2 for an alternative externally-biased solution), the ultra-low-power voltage reference (sec. 5.3.5) and the externally-controlled tuning module (section 5.3.4).

5.3.1 Ultra-low-power on-chip pico-Ampere current reference

Objective: Generation of the references currents of Ibias =30pA and Iref=60pA

Figures 5.10 and 5.11 shows different self-biased structures capable of generating current biasing in-which, the resistor-based (Fig. 5.10b) and resistor-less (Fig. 5.10a), are among the conventional structures that can be found in the literature [88]. For all structures, and across the section, it is considered the current through devices M2-M4 as the target Ibias current (that is, Ibias=$I_{D2} = I_{D4}$), then, through a current copy (factor of two) of Ibias, it is generated Iref which will provide the nominal biasing for external blocks. That is, Ibias (=30pA) is an internal-block current that will be relevant within this section from a design perspective, whereas Iref is the output current that will be relevant for external blocks as will be shown.

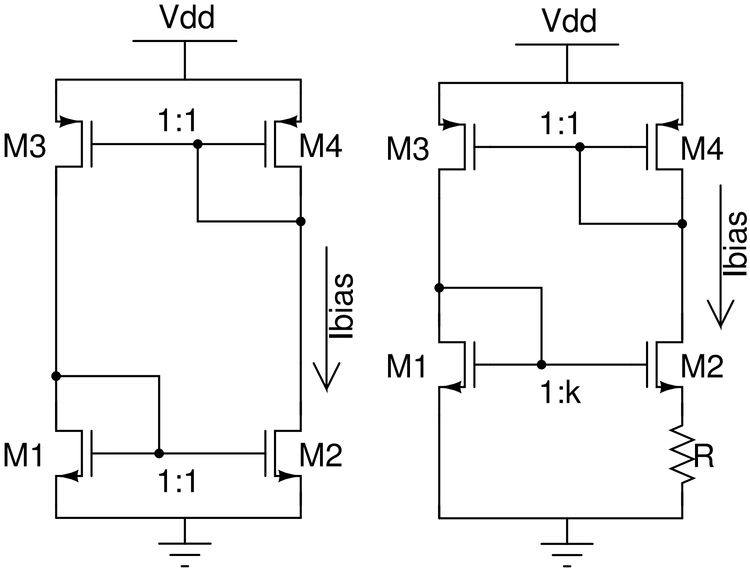

(a) Resistors-less self-biased (b) Resistor-based self-biased structure

Figure 5.10: Current bias (Ibias) generation through self-Biased structures available in the literature.

The proposed structure is based on the resistor-less structure (Fig. 5.10a) with a relevant modification to achieve the pico-Ampere biasing requirements. Especially considering that self-biased references based on resistors would need resistors (R at Fig. 5.10b) in the order of G-Ωs to generate in the order of tens of pico-Amps biasing. The proposed on-chip generation of a current reference in the order tens of pico-Amperes is based on exploiting the effect of the output transconductance of MOS devices operating at deep sub-threshold region. That is, the proposed topology (Fig. 5.11a) forces the circuit in order to use the output conductance for a role similar of the resistor R in Fig. 5.10b. That is, the equations

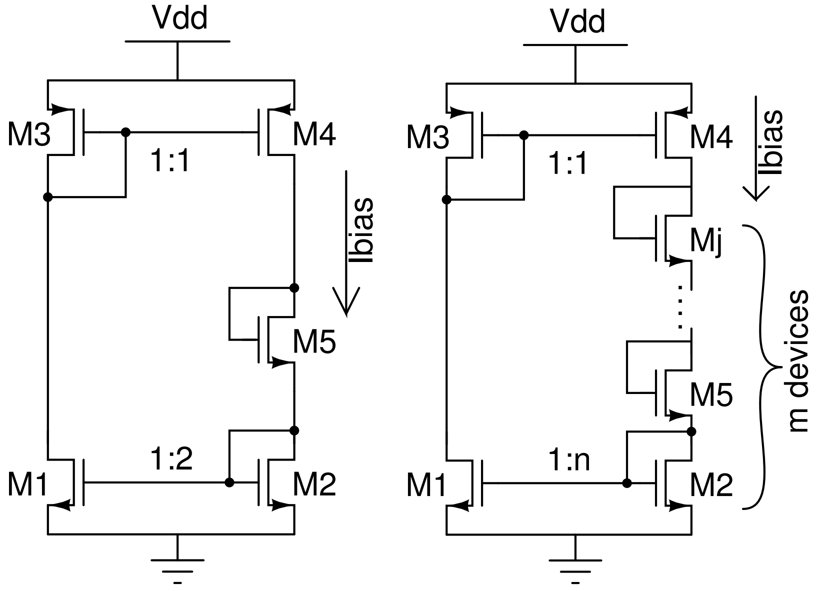

(a) Proposed self-biased (b) Proposed self-biased: generalized

Figure 5.11: Proposed self-Biased structures to generate the basing current Ibias.

of the topology implies $I_{D1} = I_{D3}$, $I_{D2} = I_{D4}$ but, copy-factors between mirrors defined M1-M2 (n_{12}=2) and M3-M4 (n_{34}=1) impose an in-congruent restriction for such currents. The circuit resolves such a situation by increasing the unitary copy factor of M3-M4 by utilizing the output conductance (OC) effect.

Considering the following simple model (5.5) for the drain current of a NMOS device at weak inversion. Diffusion current is the predominant conduction mechanism at such region which lead in a exponential behaviour for drain current.

$$ID \approx I_0 \, e^{\frac{V_{GS}}{nU_t}} \left(1 + \frac{V_{DS}}{V_A}\right) \tag{5.5}$$

Where, I_0 factor embeds the characteristic current I_S along with the W (width) over L (length) factor and additional terms related to the threshold voltage. V_{GS} and V_{DS} are the gate-to-source and drain-to-source voltages, respectively. V_A parameter in 5.5 models the finite output conductance effect by incorporating to the exponential in V_{GS} behavior, the increase in drain current with the increased drain voltage. Eventually, the OC effect is one of the worst modeled characteristics of MOS devices by EDA tools, and also, here it is considered a simple linear model for the effect. Nevertheless, simulations in the used 130nm-technology showed that, for the considered long-channel MOS devices, the increased drain current due to the OC effect for P-channel devices roughly doubled the effect for the N-channel ones. Thus, in the simplified model 5.5, the parameter V_A was differentiated according to the type of CMOS device (V_{An} for the NMOS and V_{Ap} for the PMOS), then, for the considered long-channel devices, the technology verified $V_{An} \approx 2\ V_{Ap} \approx 2V$. Such relation between OC effect in N and P type devices established the wiring of the topology, that is, M3 (and not M4) was wired as a diode in Fig. 5.11a, in order to exploit the OC effect at M4 and, satisfy the requirement of increased current conduction for the M5-M4-M2 branch respect to the M3-M1 one.

Therefore, by equationing the circuit in Fig. 5.11a with the model in 5.5 as follows.

$$I_{D1} = I_{D3} \rightarrow I_{0n}\, e^{\frac{V_G}{n_n U_t}} \left(1 + \frac{V_{dd} - V'_G}{V_{An}}\right) = I_{0p}\, e^{\frac{V'_G}{n_p U_t}} \left(1 + \frac{V'_G}{V_{Ap}}\right) \tag{5.6}$$

$$I_{D2} = I_{D4} \rightarrow 2\ I_{0n}\, e^{\frac{V_G}{n_n U_t}} \left(1 + \frac{V_G}{V_{An}}\right) = I_{0p}\, e^{\frac{V'_G}{n_p U_t}} \left(1 + \frac{V_{dd} - 2\ V_G}{V_{Ap}}\right) \tag{5.7}$$

where V_G stands for the gate-to-source voltage (V_{GS}) at NMOS devices, and, V'_G for the source-to-gate voltage (V_{SG}) at PMOS devices. By dividing the drain currents in 5.6 and 5.7 results in 5.8,

$$\frac{I_{D1}}{I_{D2}} = \frac{I_{D3}}{I_{D4}} \rightarrow 2\left(1 + \frac{V_G}{V_{An}}\right)\left(1 + \frac{V'_G}{V_{Ap}}\right) = \left(1 + \frac{V_{dd} - V'_G}{V_{An}}\right)\left(1 + \frac{V_{dd} - 2\ V_G}{V_{Ap}}\right) \tag{5.8}$$

Then, by considering roughly a similar drop at $V_{GS} \approx V_{SG}$ at N and P devices, and thus, $V_G \approx V'_G$. The voltage V_G could be approximated from 5.9.

$$V_G \approx \frac{\frac{V_{dd}}{V_{An}//V_{Ap}} + \frac{V_{dd}^2}{V_{An}V_{Ap}} - 1}{\frac{2}{V_{An}//V_{Ap}} + \frac{1}{V_{An}//\frac{V_{Ap}}{2}} + \frac{3\ V_{dd}}{V_{An}V_{Ap}}} \approx V'_G \tag{5.9}$$

where function $V_{An}//V_{Ap} = (V_{An}.V_{Ap})/(V_{An} + V_{Ap})$ was used in 5.9. By using $V_{dd} = 1.2\ V, V_{An} \approx 2\ V_{Ap} \approx 2V$, 5.9 lead in a theoretical gate-to-source drop of about $V_G = 208mV \approx V'_G$, which verifies a deep sub-threshold value for the gate voltage overdrive (low-power devices used in the design showed a threshold voltage about $Vth_n = 560mV$ for NMOS and $Vth_p = 500mV$ for PMOS). By comparing biasing results with the obtained through simulation with EDA tools, theoretical result 5.9 overestimated the simulated of $V_G@sim = 130mV$ and $V'_G@sim = 140mV$. The estimation accuracy could be improved by a more accurate OC theoretical modeling for devices. For instance, MOS devices simulation showed an increased output resistance by an increased V_{DS} which, was not considered in the modeling 5.5 (a constant V_A was considered), the VG solution in 5.9 reaches a weaker inversion level with such consideration, which is consistent with simulations. Nevertheless, for the time being, the analysis is enough to understand the behavior of the circuit and, as follows, to predict qualitatively changes that can be performed over the proposed circuit (see Figs 5.11a and 5.11b).

Generalization of the proposed circuit and programmable feature

The proposed circuit presents a novel point of view to be noted. An extended version of the proposed circuit is shown in Fig. 5.11b, that is, mirror M1-M2 copy factor (n) and the number of stacked diodes-devices (m) like M2...Mj could be reasonably programmed by adding transmission gates properly. Then, through a derivation similar to the presented in 5.8 for the circuit 5.11b, it can be showed that is possible to set the level of weak-inversion of the devices on the circuit, by setting the V_G defined by the intersection of the two programmable parabolas $y_1(V_G, n)$ and $y_2(V_G, m)$ in 5.10 and 5.11, respectively. That is, equation 5.8 is a particular case for the intersection of such parabolas when m=n=2. Figure 5.12 shows the intercept of the parabolas 5.10 and 5.11 for some values of m and n, and also for V_{dd} since it would provide a variation of $y_2(V_G, m)$.

$$y_1(V_G, n) = n\left(1 + \frac{V_G}{V_{An}}\right)\left(1 + \frac{V_G}{V_{Ap}}\right) \tag{5.10}$$

$$y_2(V_G, m) = \left(1 + \frac{V_{dd} - V_G}{V_{An}}\right)\left(1 + \frac{V_{dd} - m\,V_G}{V_{Ap}}\right) \tag{5.11}$$

Figure 5.12 shows 5.10 and 5.11 for some values of m and n, and also for V_{dd}. Sub-figures 5.12a-5.12d titles shows the V_G ($\approx V_G'$) defined by the intercept of parabolas and, the simulated (absolute) gate-source voltages of NMOS ($V_G@sim$) and PMOS ($V_G'@sim$). Even thought the presented model over-estimates the simulated V_G (it could be improved by an improved OC modelling), it gives an insight of biasing changes by different selections of m,n, and V_{dd}. Particularly, tuning Ibias by the variation of V_{dd} would provide a continuous biasing adjustment which is suitable for the proposed PTT-filtering application which seeks for an accurate biasing.

Final version of the current reference circuit

Fabricated circuit (Fig. 5.11a) is a particular configuration (m=n=2) of the circuit in Fig. 5.11b. Eventually, proposed design may be affected by the process fabrication, especially considering that such a low biasing current (Ibias =30pA) is achieved by exploiting the output resistance effect of MOS devices which corresponds with a second-order effect on the I-V characteristic of MOS devices. The design adjusts Vdd node showed in Fig. 5.11a in order to achieve the Ibias =30pA specification despite fluctuations due to the process fabrication. Monte Carlo simulations (N=500 runs, process and mismatch) showed that an yield of 100% can be achieved for a programmable $V_{dd} < 1.5V$ in order to achieve the Ibias=30pA specification along process. Then, being Vdd input-node in Fig. 5.11a a node responsible for tuning the Ibias, it will be considered as a high-impedance node to be accessed externally from a pin of the chip, such an input node is named as VddRef from now on in order to be differentiated from the global power-supply node (Vdd) of the chip. In the meantime, such implementation for the reference current might be just a practical solution for providing on-chip the required current reference easily. In the near the future the block might provide autonomously the required referencing by adding the adequate loop for controlling VddRef node. Figure 5.13 shows the final design of the proposed current reference where an Ibias=30pA can

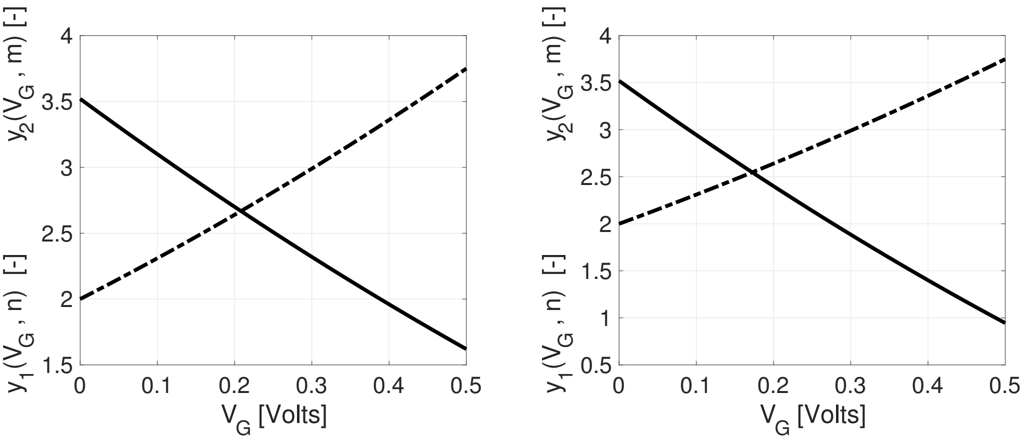

(a) m=2, n=2, $V_{dd} = 1.2V \rightarrow V_G = 208mV$ $V_G@sim = 130mV$ $V'_G@sim = 140mV$

(b) m=3, n=2, $V_{dd} = 1.2V \rightarrow V_G = 170mV$ $V_G@sim = 110mV$ $V'_G@sim = 124mV$

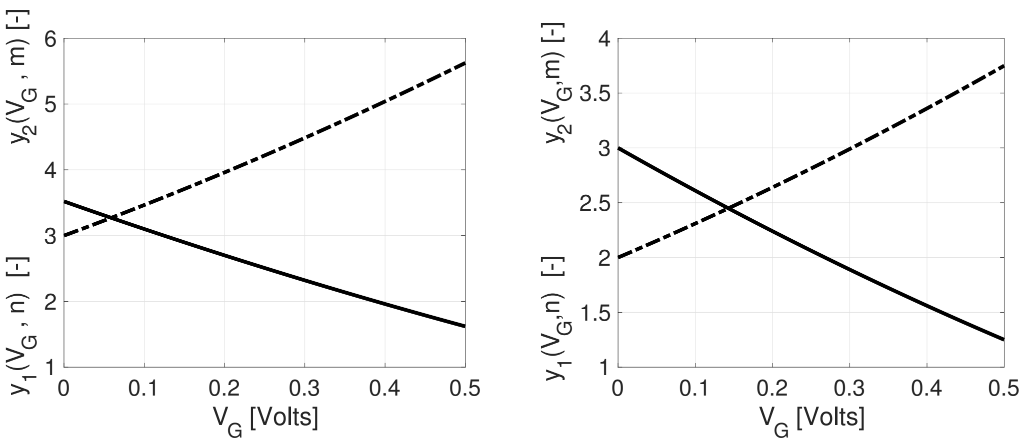

(c) m=2, n=3, $V_{dd} = 1.2V \rightarrow V_G = 60mV$ $V_G@sim = 90mV$ $V'_G@sim = 110mV$

(d) m=2, n=2, $V_{dd} = 1V \rightarrow V_G = 140mV$ $V_G@sim = 110mV$ $V'_G@sim = 120mV$

Figure 5.12: Programmed bias for the extended version of the proposed circuit 5.11b. Dashed curve represents a $y_2(V_G, m)$ and continuous one the $y_1(V_G, n)$ for few values in n, m and V_{dd}. Different discrete settings can be found by modifying the mirror M1-M2 copy-factor (n) and the number of stacked diodes-devices like M4-M2 (m), affecting the curves $y_1(V_G, n)$ and $y_2(V_G, m)$, respectively. Additionally, parabola $y_2(V_G, m)$ is affected by modifying V_{dd}. Fabricated design used the particular case of n=m=2 (Fig. 5.12a) where simulations showed an Ibias in the order of ten of pA as needed. Sub-figures 5.12a-5.12d titles shows the V_G ($\approx V'_G$) estimated by 5.9 and the simulated (absolute) gate-source voltages of NMOS ($V_G@sim$) and PMOS ($V'_G@sim$).

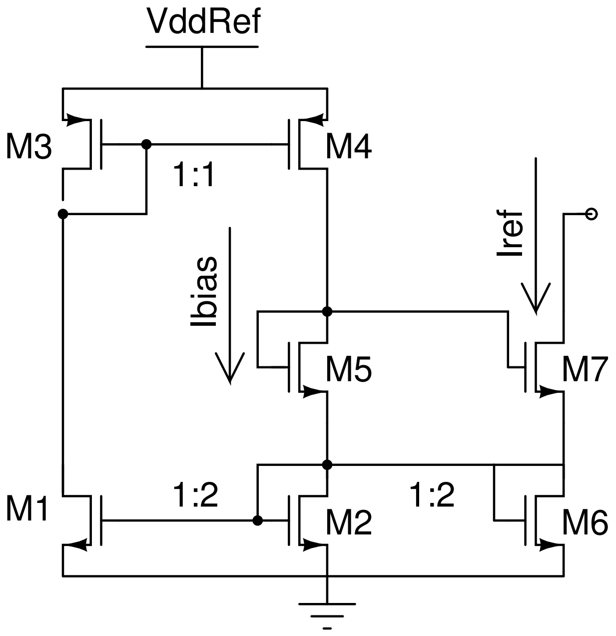

Figure 5.13: Final version of the block that implements the internal current biasing generation

be achieved along corners, and consequently, Iref= 2Ibias = 60pA is also provided by mirroring.

5.3.2 Externally pico-ampered current biasing

Objective: Alternative generation of currents Ibias =30pA and, Iref=60pA.

In order to provide the circuit with an alternative current reference generation, an externally induced current was included on the chip. Figure 5.14a shows a simplified scheme of the used circuit which includes an external resistor R_{BEXT} and on-chip MOS devices; an external current (I_{ext}) generated by a resistance (R_{BEXT}) in series with two PMOS (wired as diodes), is scaled-down (factor 1/M) to an output current (I_{div}) by a current mirroring procedure. The circuit exploits the parallel-series approach [79] in order to achieve a considerable attenuation factor (M) at the current-mirroring between I_{ext} and I_{div} currents. Notably, the block implements a cascade of two structures of 12 devices in parallel by 12 in series as shown in Fig. 5.14b, resulting in a theoretical attenuation factor of $M = 12^4 = 20.74\ kA/A$.

Circuit simulator showed a systematic under-estimation for the current-copy factor at nominal conditions ($M_{nom} = 19.6\ kA/A$) along with Monte Carlo simulations ($M_{MC\mu} = 19.9\ kA/A$, $M_{MC\sigma} = 367\ A/A$, $M_{MC_{min}} = 19.14\ kA/A$, $M_{MC_{max}} = 22.57\ kA/A$). Nominal simulations showed that biasing the circuit with an external resistor of $R_{BEXT} = 390\ k\Omega$ ($R_{BEXT} = 120\ k\Omega$) generated a current flow (at the on-chip PMOS devices) of $I_{ext} = 610\ nA$ ($I_{ext} = 1.22\ nA$). A copy factor of $1/M_{nom}$ lead to the $I_{div} = 30pA$ ($I_{div} = 60pA$), which is an alternative

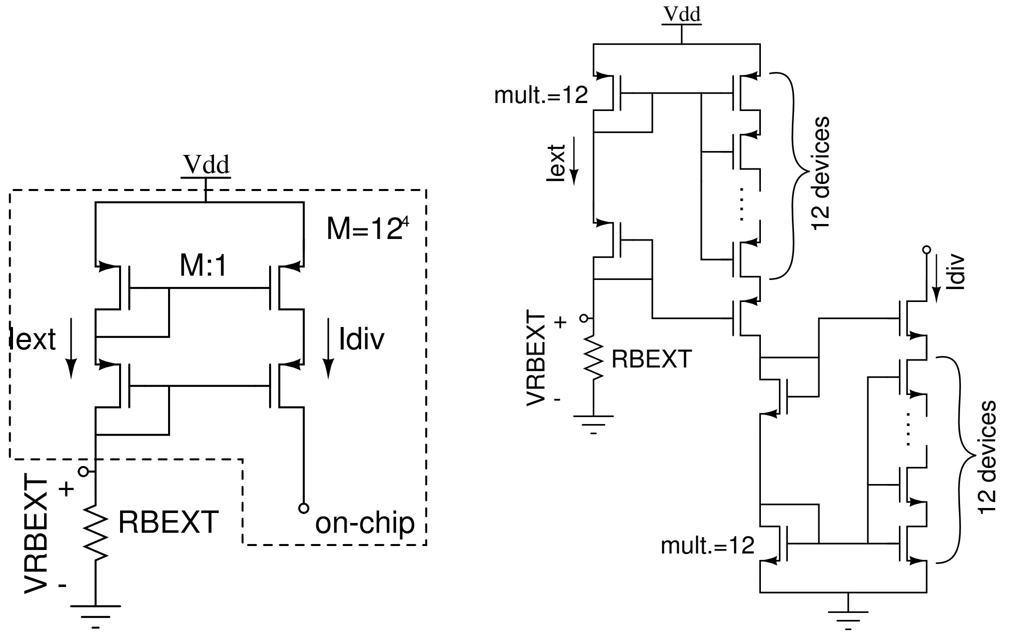

(a) Simplified View (b) Implementation

Figure 5.14: Scheme of the externally generated current biasing.

solution for the current reference of the previous section (sec. 5.3.1). Eventually, such an alternative reference requires an external resistor, and it does not offer an efficient solution as the previously presented one (sec. 5.3.1) since, for example, it draws more than 614nA to generate a 30pA reference. Internal current reference in the previous section draws 45 pA to generate 30pA, but it may require a variable Vdd_{ref} for tuning I_{ref} as a drawback. Nevertheless, on-chip and external current biasing circuits offer two simple solutions to obtain the required pico-Ampered current biasing, which might be difficult of injecting directly at the chip with no specialized equipment; and further, having an alternative circuit for generating the required current biasing served mechanisms to characterize the proposed on-chip current reference. The next section shows how the later was implemented in the design.

5.3.3 Mechanisms for selection and characterization of biasing currents

Further circuitry was included in the design in order to provide a mechanism to select between currents Iref (sec. 5.3.1) or Idiv (sec. 5.3.2) for biasing the filter in section (sec. 5.2) and also, in order to provide a mechanism for measuring such small currents. Figure 5.15 summarizes the level-view of the design that includes the biasing selection and characterization. The figure includes the blocks that implement Iref and Idiv, an analog multiplexer (AMUX), the tuning module (see sec.

5.3.4) that provides the biasing for the filter in section 5.2, and a current-controlled-oscillator (CCO) which produces an square-wave signal (assessed externally) with a frequency proportional to its input current.

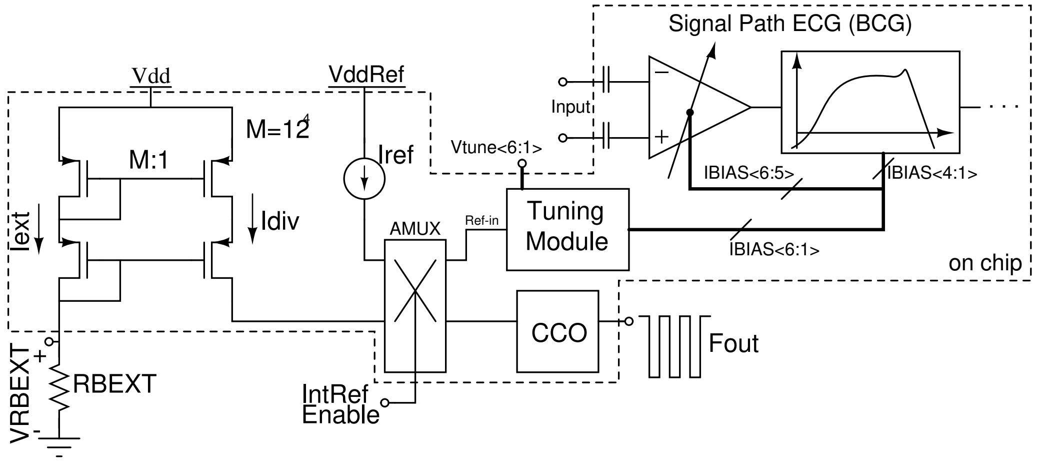

Figure 5.15: Top-level of current biasing. Analog multiplexer (AMUX) selects the wiring of Iref or Idiv currents, where, *IntRefEnable=1* sets Iref into the tuning module and Idiv into the current-controlled-oscillator (CCO), and reversely, *IntRefEnable=0* sets Iref into the CCO and Idiv into the tuning module.

Biasing currents, Iref and Ibias, are connected into the AMUX, which alternatively wires such currents between the tuning module and the CCO block. That is, digital signal *IntRefEnable* at AMUX (assessed externally), selects the wiring, where, *IntRefEnable=1* sets Iref into the tuning module and Idiv into the CCO, and reversely, *IntRefEnable=0* sets Iref into the CCO and Idiv into the tuning module.

5.3.4 Tuning Module

Objective: Generation of the I_{BIASj} currents required by the proposed filtering block (see table 5.2).

As showed at the end of section 5.2, proposed filter should include the possibility of tuning its biasing currents (I_{BIASj}) in order to preserve the required frequency response by also coping with process fluctuations. One possibility for implementing such current tuning might be given by using a circuit similar to the shown in Fig. 5.16a. Effectively, an eventual I_{BIASj} might be adjusted by setting the gate voltage properly. However, one of the main drawback of such an approach arises in the lack of control for the current to be tuned. That is, several orders of magnitude on I_{BIASj} could be reached through in the order of volts variations on the gate voltage. Given that the required tuning for I_{BIASj} remains in the order or tens of pico-Ampere for all corners in the technology (see table 5.2), such an approach for tuning would be difficult to implement properly.

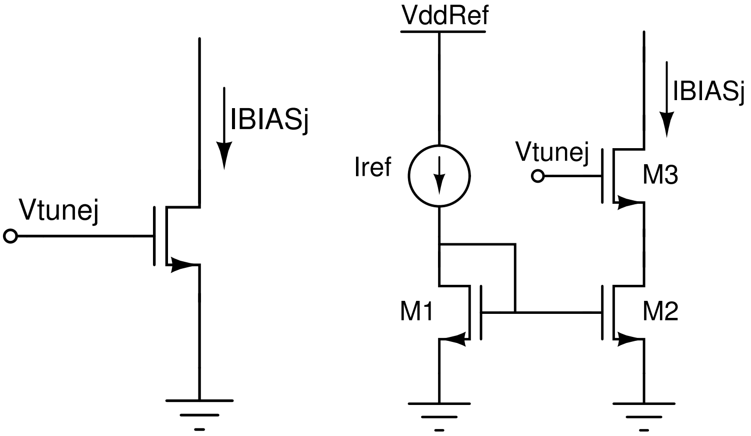

(a) Common source approach (b) Proposed Tuning Implementation

Figure 5.16: Generation of I_{BIASj} current which is tuned by a voltage Vtune.

Since I_{BIASj} currents are fractions (and, in the proximity) of Iref (or Iref/2), the proposed approach aims to perturb current copies of Iref in a controlled way for achieving each individual I_{BIASj}. That is, Fig. 5.16b shows the approach which tunes a copy of Iref by adjusting the voltage at terminal Vtunej; eventually, I_{BIAS1} and I_{BIAS3} as a fraction of Iref/2 (see table 5.2), are achieved from a proper mirroring, as will be shown later. The approach exploits the output conductance (OC) effect of MOS devices, which would produce a soft modulation of its large signal direct current by modifying its drain voltage. For instance, As was mentioned in section 5.3.1, the rough first-order modeling for OC effect might result in a linear modulation for such current; which in turn, the modulation strength depends on the channel length. The shorter the MOS device channel, the heavier such modulation slope is.

Concerning the proposed circuit for tuning I_{BIASj} currents by using the OC effect, increasing the modulation (or tuning capability) implies reducing the channel length of devices M1 and M2 in Fig. 5.16b, which, eventually, it also reduces the matching between transistors that implement the current mirror. Consequently, it exists a tuning-matching trade-off on the length design of M1-M2 devices. Another drawback for the proposed tuning approach might arise in the substantial reduction of the output impedance of the tuning module (r_{out}: output impedance seen at M3 drain on the circuit in Fig. 5.16b) when Vtunej voltage is sufficiently decreased, since M2 operates in triode region for small enough Vtunej values. The problem of biasing a circuit with a current source with relatively small output impedance could lead to a poor common-mode-rejection-ratio, or a poor gain, if, for instance, such current source would be directly tied to a differential-pair or to a common-source-amplifier/class-A stage, respectively. Nevertheless, currents I_{BIASj} are further mirrored (in this chip) until such currents reach the biased block; thus, the reader should note that a relatively low r_{out} may not cause such kind of limitations. Otherwise, the eventual triode operation at the M2 device is precisely the cause for I_{BIASj} reaching small fractions of Iref (Iref/2).

In order to have a knowledge of the tuning boundaries that ensures an acceptable r_{out}, it is defined a reference value for the minimum Vtunej ($Vtunej_{min}$) to be considered. Tuning module output impedance could be estimated by 5.12.

$$r_{out} \approx \frac{g_{ds3}}{g_{m3}\ g_{ds2}} \tag{5.12}$$

Where g_{mj} and g_{dsj} are the gate transconductance and the output transconductance, respectively, for the j-th NMOS device on Fig. 5.16b. Then, $Vtunej_{min}$ is defined as minimum value at Vtunej so that r_{out} with M2 operating in the triode region reaches the same output impedance of the M2 device operating at saturation region. Equation 5.13 summarizes the definition of $Vtunej_{min}$; since $g_{ds2}@M_{2Triode}$ depends (strong-inversely) on Vtunej, there exist a (small) Vtunej which satisfies the condition in 5.13.

$$Vtunej_{min} = MIN(Vtunej)\ /\ \frac{g_{ds3}}{g_{m3}\ g_{ds2}@M_{2Triode}} \approx \frac{1}{g_{ds2}@M_{2Saturated}} \tag{5.13}$$

On the other hand, analogously, it is defined a reference value for the maximum allowable voltage at Vtunej for tuning. That is, the criteria was based on allowing enough headroom for stacking two PMOS wired as diode to load the tuning structure (as shown in Fig. 5.17). Preliminary simulations showed that $Vtunej_{max} \approx Vdd - 4U_t$ reasonably satisfied such headroom restrictions, since the heavily affected by body effect M3 device (@Vtunej=$Vtunej_{max}$) presented barely a gate-source voltage drop similar to the required by the mentioned load (MP1 and MP2 diodes). Figure 5.17 summarizes the tuning procedure where the desired I_{BIASj} is obtained as a corrupted copy of Iref at will by setting Vtunej properly. Then, $Vtunej_{max}$ and $Vtunej_{min}$ defines a pair of safe boundaries for the Vtunej in order to tune a particular I_{BIASj}.

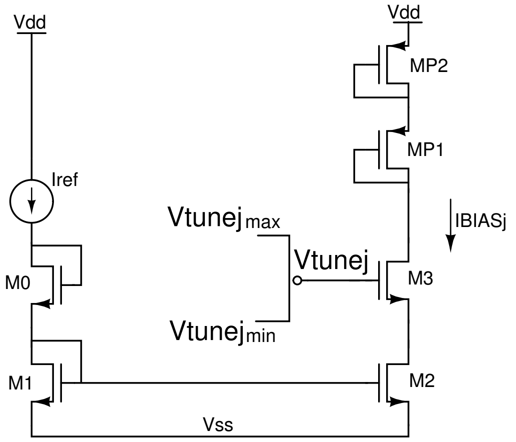

Figure 5.17: Tuning procedure, the desired I_{BIASj} is obtained as a corrupted copy of Iref at will by setting Vtunej properly.

Design

Regarding the design of the proposed tuning scheme (Fig. 5.16b). Current mirror defined by M1 and M2 devices, certainly would require the shortest channel length available in order to maximize the tuning capability. Whereas the mentioned tuning-matching trade-off would force to set a limit for the abuse of OC effect on shortening the device channel. The adopted criteria was to decrease the M1-M2 length but just the necessary to fulfill the required tuning specs along the corners. In this sense, table 5.2 shows that tuning procedure must provide a 108% (11%) of Iref (Iref/2) as a maximum (minimum) tuning boundary. Channel length was chosen so that maximum tuning boundary (108%) was achieved in a Monte Carlo analysis (process and missmatch, N=500) with an yield of the 100% when Vtunej was tied to a voltage source of $Vdd - 4U_t$ (1.1V). Additionally, by defining tuning capability of the approach as the spread reached by the I_{BIASj}-over-Iref quantity (expressed in percentage); the design achieved tuning capability of [7%, 120%] for Vtunej in the range of $[Vtunej_{min}, Vtunej_{max}]$ for a nominal simulation with EDA tools. Nominal simulations also showed a $Vtunej_{min} \approx 20mV$, by using 5.13 and the operating point data from a DC simulation, as long as, by measuring $Vtunej_{min}$ directly from AC simulations with EDA tools. Therefore, such result confirmed that Vtunej range could almost cover the supply range by maintaining acceptable values of r_{out} and a proper operation.

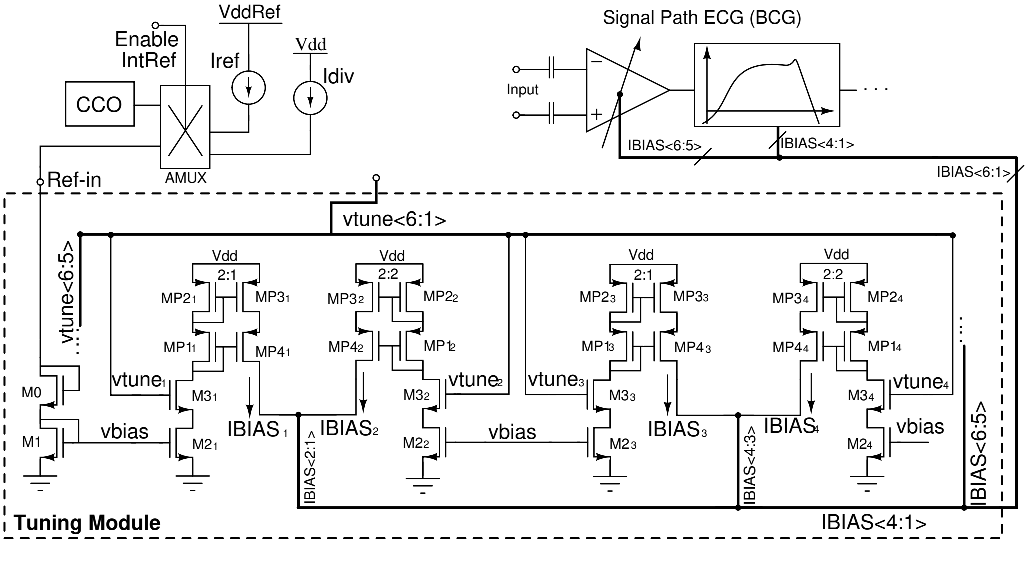

Figure 5.18: Tuning module at transistor level.

Figure 5.18 shows the expanded version of the tuning module at transistor level; Idiv or Iref input selection (with AMUX) (as long as a portion of the signal path) were also included to show the operation context of the tuning block. Idiv of Iref (both intended to source 60pA) serves the input current reference (at the Ref-in input of the block) to be tuned by the presented approach. Proposed tuning procedure tunes each I_{BIASj} from the current injected at Ref-in by controlling the respective Vtunej voltages. Filter in section 5.2 uses $I_{BIAS} < 4 : 1 >$ for biasing, whereas, pre-Amplifier uses $I_{BIAS} < 6 : 5 >$ for bandwidth and gain tuning (not included in this thesis). Respectively mirrors implemented by MP2j:MP3j devices in Fig. 5.18, sets the nominal values for the I_{BIASj} currents as follows in table 5.3:

Table 5.3: Nominal values for the bias currents (I_{BIASj}) to be tuned and then to be sourcing to signal path ECG filter. Extracted from table 5.2 in section 5.2

	I_{BIAS1}	I_{BIAS2}	I_{BIAS3}	I_{BIAS4}
nominal (100%)	30 pA	60 pA	30 pA	60pA

Finally, just to report the role of the tuning module on this chip. Although this document is centralized in the ECG signal path, tuning Module provides the tuning for both signal paths. That is, twelve tuned currents are provided for this tuning block in order to source ECG and BCG signal paths with the required biasing.

Corollary application

Presented ideas for modulating currents through OC effect could be extended to other types of circuits, which may require a controlled (soft) variations of a particular biasing currents. For instance, that is the case for the Gm4 operational transconductance amplifier block showed in Fig. 5.4b. Block Gm4 uses such an approach to generate an additional input (DC_Cont), which provides a path for the feedback-loop responsible for the DC-attenuation feature and the setting of the common voltage of the filter (see sec. 5.2). Figure 5.19 shows the full implementation of the Gm4 block at transistor level.

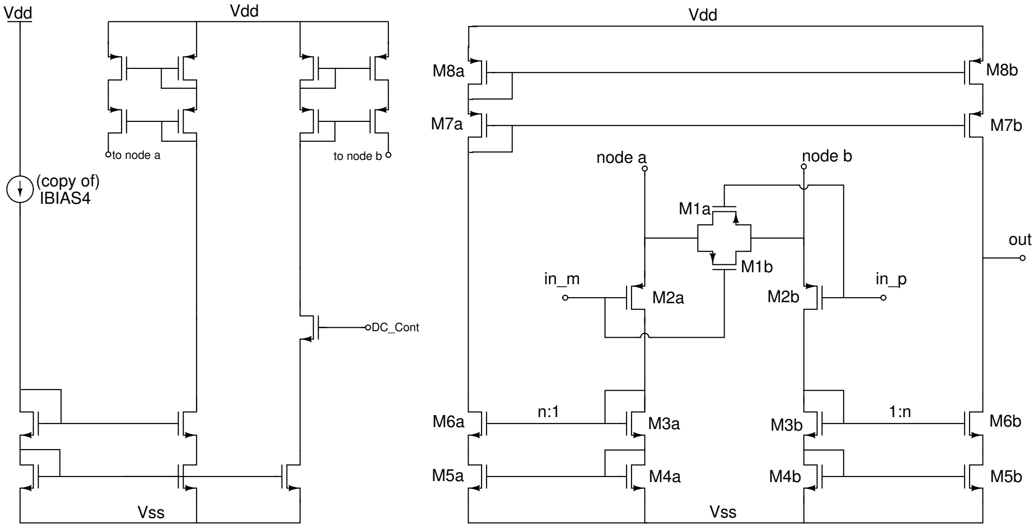

Figure 5.19: Full transistor-level implementation of mplifier Gm4 which uses the presented approach to provide the block with an additional input at DC_Cont node

5.3.5 Voltage divider as a voltage reference

Objective: Ultra-low-power on-chip generation of a voltage divider as reference of Vref= Vdd/2 = 600 mV to load up to 50pF-capacitance nodes

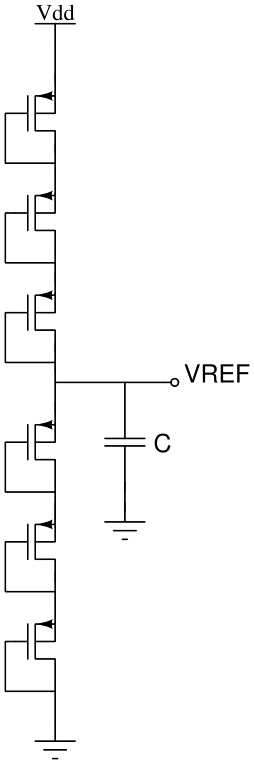

Figure 5.20: Voltage Reference Implementation at transistor level

Besides of an accurate current biasing, the proposed filtering scheme in Fig. 5.4a, requires a voltage reference to operate. Plus, in order to maintain consistency for the whole design, the implementation for such voltage reference should achieve such an ultra-low-power characteristic as the proposed current biasing (sec. 5.3.1). Systemic top-level requirements established that the block should deliver a stable voltage at the mid-range of the supply voltage, that is, Vref=600mV for a $V_{DD} = 1.2V$; and, the voltage reference is intended to only be loaded by capacitive nodes in the chip. Thus, top-level specifications could be reasonably fulfilled by a voltage divider structure. Even though such structure is not a voltage reference (mainly because of the Vdd dependence), some abuse of notation might occur at this point, and the presented voltage divider block in this section will be referred to as voltage reference because of its role of providing a (voltage) reference in the chip.

Eventually, on-chip voltage dividers utilizing stacked resistors may lead to an inviable budget of chip area or power consumption. That is, in order to achieve an ultra-low-power design with power consumption similar to the achieved by the proposed current bias (sec 5.3.1), a 30 $G\Omega$ resistor is required, where (as previously discussed) integrable resistors values are limited to tens of $M\Omega$. Figure 5.20 shows the proposed implementation for the voltage reference, which rather than stack resistors, the design uses stacked (low power) transistors wired as diodes. The design leverages from stacking the threshold voltages of the devices (which opposes the current flow) in order to cover the voltage supply range, which leads to low current draws by using few devices. Also, the voltage divider was constructed with PMOS devices with sources tied to the body to ensure no body bias source-bulk (and thus avoiding threshold voltage differences between devices) in order to achieve the same voltage drop at each device.

Design

Relatively large PMOS devices (W/L=4/20) were used in order to reduce the mismatch between devices by maintaining the area-mismatch trade-off at reasonable values. Monte Carlo (N=500 samples) simulations showed a solid stability for the proposed voltage reference along process and mismatch, showing a Gaussian behaviour with a mean value of $Vref_{\mu} = 600\ mV$ and a standard deviation of

$Vref_{\sigma} = 0.5\ mV$; whereas $Vref$ current draw (I_{dd}) showed a right-skewed distribution with the following parameters: $\mu = 108pA$, $\sigma = 120pA$, and maximum and minimum values of $Max_{Idd} = 1.2nA$ and $Min_{Idd} = 7pA$. Eventually, current draw scattering seems to be the main issue of this simple approach to obtain an on-chip ultra-low-power voltage reference. Nevertheless, it can be showed that such an issue might not be a problem at application time, by analyzing potential problems at the worst possible scenarios for the block. That is, a batch which voltage reference draws Min_{Idd} might have problems related to starting-up/settling time or/and dynamic recover issues caused by glitches at eventual Vref node. For instance, when circuit starts-up with a Vref=0 at scenario, the Vref node is loaded by the three PMOS devices wired between Vref and Vdd, which would have a higher current capacity being at a stronger inversion region since, Vdd would drop only over such three devices. Simulations showed that such a low current draw in Vref $Min_{Idd} = 7pA$ would load (up to 99%) a 50 pF at Vref node in the order of one second, which is an reasonable start-up time for a biomedical application. Then, for a steady-state situation, after a small ripple at Vref node the voltage reference would have a time-constant (τ_{rcvry}) for recovering of

$$\tau_{rcvry} \approx \frac{50pF}{1.5\left(\frac{g_m}{I_D}\right) Min_{Idd}} \approx \frac{50pF\ nU_t}{1.5\left(\frac{g_m}{I_D}\right) Min_{Idd}} \approx 175ms \tag{5.14}$$

On the other hand, for a very low probable batch which voltage reference draws the maximum estimated current from power supply ($Max_{Idd} = 1.2nA$), the design would achieve the best recovery/settling time responses whereas it remains a reasonably low-power design.

5.4 Silicon results

As was mentioned previously, the whole design presented in this chapter was fabricated in the GlobalFoundries GFUS-8RF technology featuring a 130nm node. Previous sections showed results assessed through simulations with EDA tools for each particular block, whereas this section aims to show some measurements over fabricated chips. Five chips were encapsulated in a QFN56 package, and accordingly, measured data is shown for such five prototypes. Regarding the measurements, unfortunately, the design did not contemplate methods for individual characterization of the designed blocks (mainly due to the ambitious number of blocks integrated on-chip in order to achieve a fully integrated characteristic and the lack of pin-out available). This restriction constrained critically the quality/quantity of measurements that can be done for the individual blocks characterization. For instance, the voltage reference block Vref (sec. 5.3.5) was not available for being assessed from outside the chip. Thus, due to the simplicity of such design, the relatively secondary role at the whole system, and the high yield achieved at Monte Carlo simulations, the voltage reference presented a low priority for spending resources (time, pin-out) for characterization and thus, no results are presented here. Also, as will be shown, neither for blocks at the signal path chain was possible to consider an adequate individual characterization, particularly, that includes the proposed filter (sec. 5.2). Unfortunately, that was the outcome for seeking such an ambitious design that integrates all the required blocks and mechanisms for the proposed PTT acquisition.

Concerning the available silicon assessments, this section begins with measurements over the current mirror that from an external current generates the required pico-ampered (30-60 pA) current biasing (seen in section 5.3.2); then, measurements on the proposed on-chip current reference (sec. 5.3.1) are presented; both biasing currents are measured by using on-chip dedicated circuitry (CCO:current-controlled-oscillator and AMUX:analog multiplexor) as mentioned earlier at section 5.3.3. Finally, some measurements on the proposed signal path filter (sec. 5.2) are showed.

5.4.1 External current references

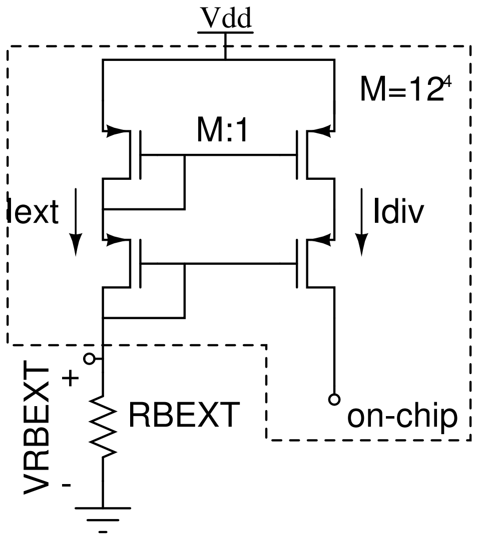

Figure 5.21: Simplified scheme for the current mirror presented in section 5.3.2. The mirror implements two series-parallel structures in cascade in order to achieve large copy-factor (M)

As presented in section 5.3.2 the external generated current (Iext) is divided inside-chip by a current mirror that features a series-parallel current divider. Although theoretical value for the copy factor (M) is $M_{theo} = 20.74\ kA/A$ ($M = 12^4$), EDA tools showed slightly under-estimated values for the simulated copy-factor at nominal conditions ($M_{nom} = 19.6\ kA/A$) along with for Monte Carlo test ($M_{MC\mu} = 19.9\ kA/A$). In order to analyze possible fluctuations for the resulted divided current (Idiv), different estimations of Idiv are constructed by using the different M obtained. In this sense it will be distinguished $Idiv_{theo}$, $Idiv_{nom}$, $Idiv_{MC\mu}$, $Idiv_{MC_{min}}$ and $Idiv_{MC_{max}}$, as the considered estimations of Idiv by using the copy-factors found in section 5.3.2, these are, M_{theo} (theoretical M), M_{nom}

(simulated: nominal M), $M_{MC\mu}$ (simulated: Monte Carlo mean value achieved), $M_{MC_{min}}$ (simulated: Monte Carlo minimum M achieved) and $M_{MC_{max}}$ (simulated: Monte Carlo maximum M achieved).

Regarding the generation of the external current, Iext was generated from a resistor R_{BEXT} along with the two on-chip PMOS transistor as shown in Fig. 5.21 and mentioned in sec. 5.3.2; and, Iext was assessed by measuring the voltage VR_{BEXT} from a known R_{BEXT}. $R_{BEXT} = 245k\Omega$ was chosen to produce an Idiv in the order of 30 pico-Amperes at current mirror output. The following table shows the measured VR_{BEXT} and Iext along with the mentioned Idiv estimations (from Iext) for the five propotypes.

Table 5.4: Estimation of Idiv current as a factor (M) of Iext current. Considered M values (showed at last column) lead to different Idiv results. Following Idiv estimation will be performed using the mean M from the Monte Carlo analysis ($M_{MC\mu}$19.9 kA/A)

Chip #	1	2	3	4	5	Units	M (kA/A)
VR$_{BEXT}$	165	152.2	152.3	160	154	mV	-
Iext	650	621	622	653	629	nA	-
$Idiv_{theo}$	31.3	30	30	31.5	30.3	pA	20.74
$Idiv_{nom}$	33.2	31.7	31.7	33.3	32.1	pA	19.6
$Idiv_{MC\mu}$	**32.7**	**31.2**	**31.3**	**32.8**	**31.6**	**pA**	**19.9**
$Idiv_{MC_{min}}$	34.0	32.4	32.5	34.1	32.9	pA	19.14
$Idiv_{MC_{max}}$	28.8	27.5	27.6	28.9	27.9	pA	22.6

Even though circuit simulator underestimated the theoretical Idiv current, the spread of all the considered Idiv estimations remained inside the 5% (of relative error) from the estimated by the mean of the Monte Carlo test (if the low-probable $Idiv_{MC_{max}}$ estimation is discarded). Therefore, $M_{MC\mu}$ will be the considered copy-factor M used for Idiv estimation from now on; in other words, Idiv (M) and $Idiv_{MC\mu}$ ($M_{MC\mu}$) magnitudes will be considered the same hereafter.

5.4.2 Measurements of on-chip currents by using the current controlled oscillator

As previously mentioned in section 5.3.3, a current controlled oscillator (CCO) was included to measure the inside-chip reference currents by performing frequency measurements. That is, given that CCO input can be alternated between the (apriori) known current Idiv and the un-known internal generated current Iref; the latter was intended to be assessed from CCO responses to Iref after CCO transference (output frequency as a function of the input controlled current) was characterized by injecting different Idiv inputs.

Current controlled oscillator transference - Idiv driven CCO test

Table 5.5 shows the tests performed over the CCO for three values of Idiv, that is, three R_{BEXT} were used to produce in the order of Idiv= 30pA, 45pA, 60pA.

CCO output frequency (F_{out}), R_{BEXT}, voltage drop across R_{BEXT} (VR) and estimated Idiv current were included in table 5.5. Even though the described CCO characterization procedure was intended to be performed for all the five chip prototypes, chip# 3 showed issues with the switching between Iref and Idiv currents (always Iref was wired to CCO no matter the IntRefEnable state), which prevented them from being measured properly, and consequently, chip# data was discarded.

Chip #	1	2	4	5	Units
Test 1	$F_{out} = 146.5$	$F_{out} = 131$	$F_{out} = 156$	$F_{out} = 147.5$	Hz
R_{BEXT}	VR= 84	VR=77.8	VR=85	VR= 78	mV
$71k\Omega$	Idiv= 59.4	Idiv=54.2	Idiv=60.4	Idiv= 55.2	pA
Test 2	$F_{out} = 121$	$F_{out} = 105$	$F_{out} = 126$	$F_{out} = 117.5$	Hz
R_{BEXT}	VR= 110	VR= 104	VR=112	VR = 105	mV
$116k\Omega$	Idiv= 47	Idiv= 45.1	Idiv=48.5	Idiv=45.5	pA
Test 3	$F_{out} = 80$	$F_{out} = 69.8$	$F_{out} = 85$	$F_{out} = 76$	Hz
R_{BEXT}	VR = 159	VR= 152	VR=160	VR=154	mV
$245k\Omega$	Idiv= 32.7	Idiv= 31.2	Idiv=32.8	Idiv=31.6	pA

Table 5.5: Measurements on the current controlled oscillator (CCO) frequency when different Idiv currents provided the CCO input. Three tests were included which produced three different Idiv at CCO input along chips 1,2,4,5. CCO output frequency (F_{out}), R_{BEXT}, voltage drop across R_{BEXT} (VR) and estimated Idiv current were reported.

On-chip current reference (Iref) assessments - Iref driven CCO test

Internally generated current reference (Iref showed in sec 5.3.1) was indirectly assessed by using data in table 5.5 and, by assuming a linear piece-wise behaviour for the CCO frequency-current response. Particularly, since Iref value is tuned by modifying its VddRef node, the Iref tuning range was estimated by seeking for its boundary conditions for Iref through measurements. Consequently, Iref tuning range was defined from two particular conditions in the assessed Iref, that is, from a *Iref min* up to *Iref@*$(VddRef = 1.2V)$.

Where:

- *Iref min* was defined as the Iref that CCO frequency coud not be further decreased by lowering $Vddref$ node.
- *Iref@*$(VddRef = 1.2V)$ was defined as the Iref when $Vddref = 1.2V$.

Table 5.6 shows the defined Iref range assessed for chips 1,2,4,5. Output Frequency of the current controlled oscillator (F_{out}) and Iref values are reported for the mentioned boundary conditions that defines the IREF tuning range.

Chip #		1	2	4	5	Units
Iref@($Vddref = 1.2$)	Fout	110.5	54.4	114.2	93	Hz
	Iref	41.3	24.1	42.2	36	pA
Iref min	Fout	53	19.1	23.7	21.3	Hz
	Iref	22.3	10.5	9	12.8	pA

Table 5.6: Along fabricated chips

5.4.3 Proposed filtering - signal path frequency response

The proposed filter is responsible for limiting the bandwidth at the signal path, then filter features, such as bandwidth and damping factor, were intended to be assessed by measuring the frequency response of the whole signal path. That is, by injecting signal at pre-amplifier input and measuring the whole signal-path response at output-buffer output. However, the signal path could not be adequately assessed due to unexpected issues at the pre-amplifier block. In effect, Monte Carlo simulations at design time under-estimated the offset at the pre-amplifier output and, the filter DC-attenuation feature could not cope with such offset at measuring time. Being pre-amplifier a DC-decoupled block, there was (apriori) no chances for solving such an issue from outside of the chip, notably by attempting to compensate the offset at signal path input. Thus, chip samples showed a saturated output at most conditions. Figure 5.22 summarizes the signal path chain, indicating the node reported from offset issues, *input* and *output* are nodes externally accessed.

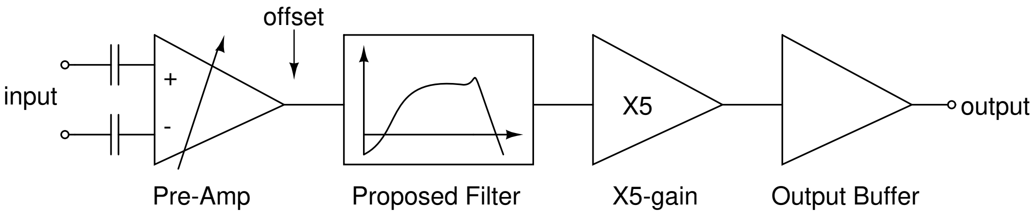

Figure 5.22: Identified offset issues at signal path

Nonetheless, one chip that featured a very poor signal path gain, which was further decreased externally (up to the minimum) at pre-amplifier and filter stages (by the proposed biasing tuning procedure showed in section 5.3.4), showed a non-saturated output. Although such a procedure degraded the pre-amplifier and filter basing conditions, it (barely) allowed to assess the frequency response of the signal path for different damping ratio settings. Unfortunately, other signal path settings could not be acquired because they lead in a saturated output.Figure 5.23 shows the frequency response of the signal path for different damping factor settings. The

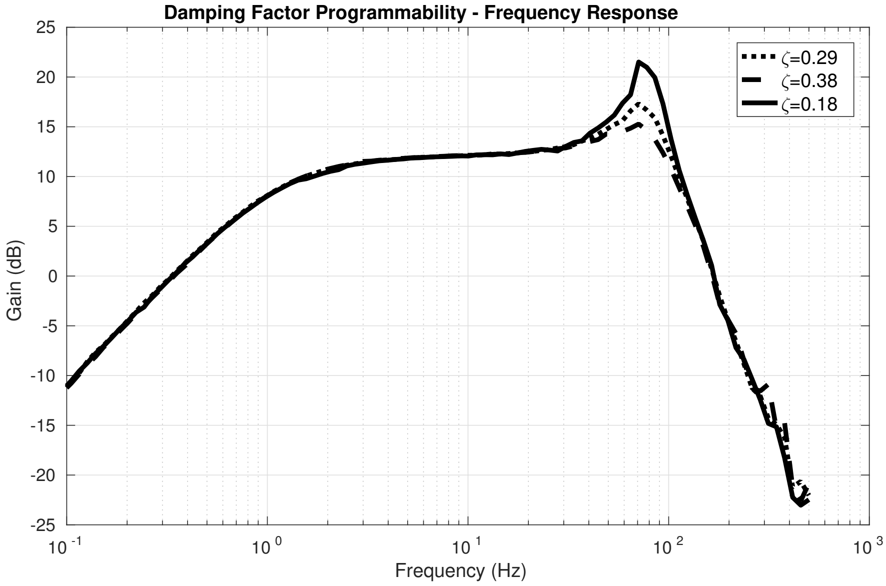

Figure 5.23: Signal path filter - Measured frequency response on chip 4

test-bench included voltage source at Vtune3 input in order to set three particular damping factor (ζ) at the filter, these were, ζ@min, ζ@mid, and ζ@max. Such ζ were defined for Vtune3 settings of $Vtunej_{min}$ ($\approx 20mV$), Vdd/2 ($= 600mV$), and $Vtunej_{max} \approx 1.1V$, respectively. Thus, ζ@max - ζ@min defines the absolute tuning range for damping factor, since it is delimited by the damping factors achieved for boundary conditions of Vtune3 voltage defined in 5.3.4.

Table 5.7 summarizes the measured achievable damping factors by the tuning procedure, as long the other signal-path frequency-response characteristics. The table includes the high pass cut-off frequency (f_{HP}), the in-band gain (Gain), the estimated natural frequency (f_n), and the mentioned damping factor. The signal path was biased by using the proposed on-chip internal current reference (Iref), which, having presented a slightly reduced generation of biasing current, consistently, it led to a slightly smaller bandwidth (f_n=72Hz) than the expected (f_n=100Hz).

Table 5.7: Filtering damping factor programability

Feature	f_{HP}	Gain	f_n	ζ@min	ζ@mid	ζ@max
Value	1.2 Hz	12 dB	72 Hz	0.18	0.29	0.38

5.5 Discussions and conclusions

The fabricated design aims to provide a highly miniaturized solution for the low-delay narrow-band ECG and BCG conditioning, which lead to a proper PTT acquisition. Material presented in the chapter is centralized on presenting a proposed second-order filter which acts at the conditioning chains for the ECG acquisition (similar filter was applied for the BCG one). Filter block is responsible for producing a particular (under-damped) bandwidth limitation characteristic, which is fundamental for achieving the proper PTT acquisition. Such an approach might be challenging to implement with integrated technologies since circuits are subject to suffer significant fluctuations in the parameters of the IC building block devices, which in turn, lead to fluctuations on the main characteristics of the designed blocks. Additionally, IC designs are limited for implementing relatively large on-chip time constants (in the order of 0.01 to 10 seconds), which would lead in the required small filtering bandwidth for this application. The pursued ultra-low-power (ULP) characteristic took the challenge for this design further away. For instance, the design required the on-chip generation of pico-ampered currents and ULP voltage references, while, efficient solutions for such particular references might not be easily found in the literature. Additionally, a ULP solution for tuning the filtering parameters of the proposed filter was showed within this chapter.

Measurements over the proposed internal current reference showed that the on-chip pico-ampered current generation is feasible by the proposed circuit. Even though the Iref value was slightly under the required spec for the tested conditions, that is, Iref≈ 40 pA @(VddRef=1.2V) while an Iref=60pA was required; proposed reference might approach the required nominal Iref for a higher VddRef as shown in the simulations (the technology supports up to Vdd=1.5V). Effectively, measurements for all prototypes suggests that Iref could be tuned up by conveniently increasing the VddRef node. On the other hand, even though the Vref block was not available for externally measurements, the voltage divider approach was used at the linear regulator block shown in Fig. 5.2 which provided an estimation of the performance of stacked MOS as a voltage divider. That is, being k, the voltage divider factor assessed; the measurements on the prototypes showed that the stacked MOS approach achieved a mean (relative) error of $\mu_{e\%}$= (expected(k) - mean(k))/mean(k)=1.5% along with a relative standard deviation over the mean of $\sigma_{e\%}$= std(k)/mean(k)= 0.2% for the voltage divider factor (k) spread for the five prototypes.

The proposed ultra-low-power second-order filter was presented as the central block of this chapter. As was mentioned, the low delay characteristic was achieved by using an under-damped second-order (target $\zeta = 0.25$) low-pass section plus a very low-frequency dc-attenuation characteristic. The filter was implemented with a modified biquad structure that features a novel feedback arrangement for dc-attenuation, and exploits, for current consumption saving, the use of a simple common source amplifier as one of the transconductors. Simulations showed that the total consumption of 2.1nA @ 1.2V power supply is achieved. Some issues encountered on the signal path prevented the proper characterization of the frequency response (mainly given by this proposed filter); nevertheless, available measurements showed the correct filter operation by also using the internally generated references (Vref and Iref). That is, the measured signal path frequency response showed that filter parameters were near ($\zeta = 0.18...0.38$, fn=72Hz) the target values ($\zeta = 0.25$, fn=100Hz) when biased with the proposed internal references and no tuning performed because of the very constrained measurements due to the mentioned unexpected offset.

The proposed filter features a novel tuning mechanism to cope with fabrication process fluctuations. Simulations showed that the particular under-damped filter characteristic could be successfully tuned for all technology corners. Preliminary measurements also showed that such required damping ratio ($\zeta = 0.25$) is achievable from the proposed tuning procedure, whereas the narrow filtering bandwidth could be easily approached to the target value ($\approx= 100Hz$) by using at least two on-chip available mechanisms (increasing Iref with VddRef and/or by tuning Gm2 or Gm1 with Vtune2 and Vtune1. The offset issues at pre-amplifier constrained the possibility of utilizing such features for the presented results.

The presented filtering approach achieved the primary goals of the design. Power consumption of about Idd=2.1 nA at Vdd=1.2 V satisfies the pursued ultra low power characteristics. The design is fully integrated; that is, it included all the required circuitry to achieve the needed functionality and, proposed auxiliary circuitry introduced novel solutions for on-chip biasing and tuning while also featured ULP characteristics. Simulations showed that the required filter frequency response could be achieved along the technology corners, whereas the assessments (despite being a kind constrained) showed remarkable behavior and programmability. Finally, proposed AFE provides a mechanism for the external adjustment of several design parameters, which could be driven by an MCU in the future application. Unfortunately, the project policy (limited individual block characterization) and the unexpected issues at the signal path, limited heavily the AFE characterization, which prevented from including more measurements at fabricated prototypes. Eventually, some circuits may deserve to be part of a future tape-out where more characterization mechanisms should be included.

This page was intentionally left blank.

Chapter 6

Wearable CABP Estimation: First Validation

Rationale

In chapter 3 was shown that central aortic blood pressure (CABP) estimation from electrocardiogram (ECG) and ballistocardiogram (BCG) might be feasible. Chapter 3 study was based on the acquisition through off-the-shelf equipment. This chapter aims to test whether the proposed wearable device (chapter 4) is capable of achieving similar feasibility results on CABP estimation. This chapter also aims to situate the scope of this wearable method to predict CABP, that is, the study analyzes (by utilizing data acquired along few days), the calibration interval of the CABP estimation and the stability of calibrated parameters of the used CABP estimation model. The study uses data from one healthy subject involving three-days trials for CABP estimation from a wearable ECG and BCG acquisition. The methodology was evaluated in two levels, which differ in the way that CABP estimations are constructed. The level-1 procedure aims to evaluate the feasibility of the proposed wearable method for estimating CABP, but also was used to determine whether the wearable version of the method achieved similar results that the obtained by using off-the-shelf equipment [69]. Meanwhile, the level-2 evaluation aims to test the capability to predict unseen CABP data. The two types of method evaluations presented in this work provided relevant information about model parameter scattering, calibration interval, accuracy, and, the strength of agreement and association. The content presented in this chapter constitutes the first set of validations for the CABP estimation method by using the proposed wearable device. In the next chapter (chapter 7) the method is tested and refined considering tests performed with ten volunteers. This chapter is organized as follows: section 6.1 presents the methods used to acquire and process the data, and the procedure to construct the estimation of CABP. In sections 6.2 and 6.3 the results of the proposed method are presented and discussed. Finally, conclusions and perspectives are drawn in section 6.4.

6.1 Methods

6.1.1 Acquisition

Acquisition was based on simultaneous CABP assessments along with the wearable ECG and BCG recordings.

CABP assessments

Central Aortic BP was assessed with the Atcor Medical SphygmoCor XCEL unit by using the pulse wave analysis (PWA) feature, which is a cuff-based methodology that provides a non-invasive central blood pressure estimation [28] [21] (see section 2.3.2). The device provides time-discrete (snapshots) BP assessments at each attempt. The assessment includes a snapshot of the central aortic sysolic, mean and diastlolic BP variables, along with the sysolic and diastlolic brachial-level ones.

Wearable ECG and BCG recordings

The wearable device presented in chapter 4 was used to record the ECG and BCG waveforms. Since ECG and BCG signals provide the timing references for the relevant feature times used in this work, phase lags between signals were carefully considered at each design stage. Mainly, analog and digital conditioning stages were selected to minimize the phase shift between signals [87]. Results showed that a delay of less than 2ms between signals could be achieved by the proposed architecture.

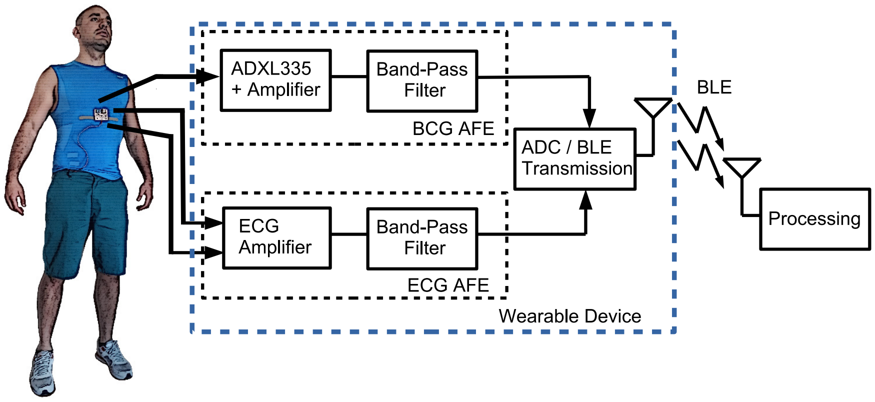

Figure 6.1: Custom Made Wearable Acquisition System: Block Diagram. System includes: head-to-foot accelerometer (ADXL335), analog front-end (AFE) signals chain for conditioning BCG and ECG signals, and a Bluetooth Low Energy (BLE) module for signal acquisition (sampling = 250 sps) and transmission to an external computer for processing.

Fig. 6.1 summarizes the wearable device hardware in a block diagram view as presented in chapter 4. The device contains a custom printed circuit board (PCB) including a longitudinal, head-to-foot, accelerometer (ADXL335), analog front-end (AFE) signal chain for BCG and ECG conditioning, and a Bluetooth

Low Energy module for signal acquisition (sampling = 250 samples-per-second-sps) and transmission to an external computer. The PCB is directly connected to dry electrodes, positioned in the chest region of a training shirt. On the remote device (computer, tablet, or smartphone), a python program receives the ECG and BCG signals, applies digital filters, and saves the processed ECG and BCG waveforms.

Nomenclature

Along this and the following chapters were used a particular nomenclature for managing the acquired data. Notably, it was defined the *data-set* as a set of paired data which includes a CABP snapshot (including the respective diastolic and systolic variables), and, a continuous-time recording ($f_s = 250$ Hz) with the wearable device (including a segment with ECG and BCG waveforms). The criteria used to define the simultaneity between these devices acquisitions is presented in the following section.

Eventually, data-sets were in turn, grouped with others data-sets within a particular trial, in order to construct a *group of data-sets*. Thus, the group of data-sets acquired at the j-th trial was referred as GR_j. Figure 6.3 summarizes these concepts along the trials considered for the experimentation in this chapter.

Blood Pressure snapshots and continuous-time data sinchronization

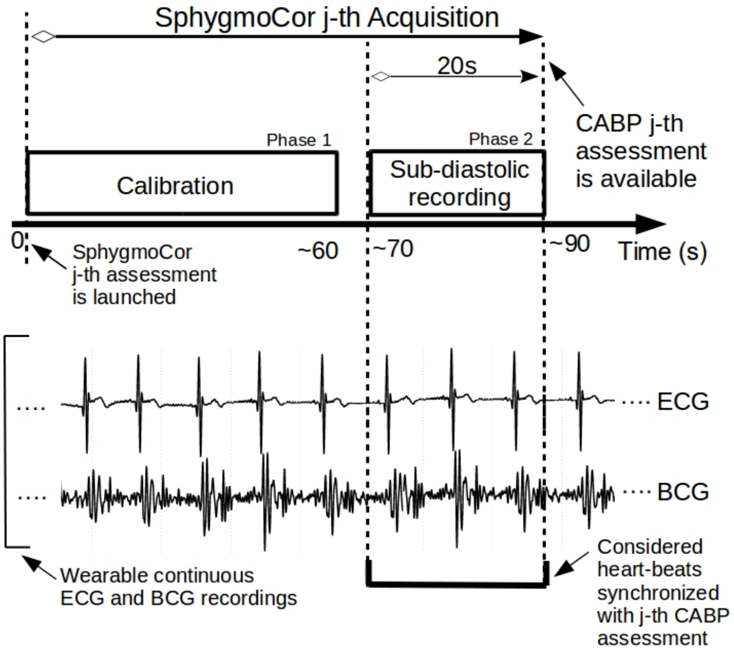

Figure 6.2: SphygmoCor acquisition phases by using the PWA. Sketched ECG and BCG signals from the proposed wearable device are superimposed in order to show the section of the wearable recordings to be considered paired with particular (j-th) CABP assessment.

In order to formalize the procedure of synchronization between an snapshot-based measurement (by the SphygmoCor XCELL) and continuous one (by the wearable device), the SphygmoCor acquistion (through the PWA feature) was further analyzed.

The SphygmoCor acquisition is performed across two phases. In the first phase, that is, the calibration phase [21], the unit obtains the brachial BP variables (i.e., systolic and diastolic) by an automatic oscillometric procedure; such procedure takes on the order of few minutes to compute the information (cuff inflation/deflation time). Then, during the second phase, that is, the sub-diastolic recording phase [21], the SphygmoCor uses the brachial variables from the first phase to calibrate the acquisition of a brachial waveform by using cuff at sub-diastolic pressure [21]; and the measurement itself is finished. The user defines the duration of the second phase. For all the trials within this document, such a phase was set to last 20 seconds. Then, aortic BP waveform is derived by applying digital signal processing based on transfer function approaches to derive the central aortic BP waveform from the brachial one [21], and thus, CABP and brachial BP variables are available. Fig. 6.2 shows a timing diagram of the phases for a particular j-th BP assessment in a trail, along with the signals in the wearable recording.

Since the sub-diastolic recording phase defines a period from which the SphygmoCor unit extracts the information for constructing the CABP estimation, wearable device recordings during such a phase in a particular j-th SphygmoCor assessment were considered paired with the resulted CABP variables from such acquisition. Figure 6.2 summarizes such an approach designed for pairing the assessments within a data-set. All the performed measurements used such a systematic procedure in order to maintain the data consistency.

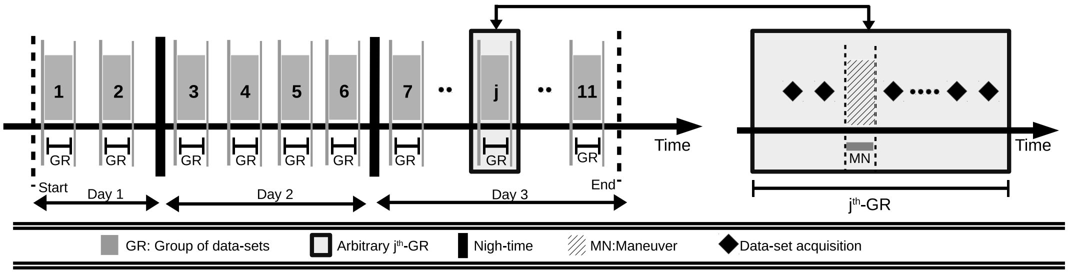

Figure 6.3: Acquisition procedure. Eleven groups of data-sets were acquired for three days of intermittent observations. Each group consists of four to six data-sets, where, data-sets included simultaneous CABP assessments and ECG and BCG recordings. Rhombus markers indicate a data-set collection event. Hatched boxes indicate a hemodynamic maneuver (MN = [HB: Hold breathing, SB: Slow breathing, HG: Handgrip, VA: Valsalva])

6.1.2 Protocol

The study used eleven groups of data-sets (GR_1 to GR_{11}) from a healthy subject recorded along three days. Each GR_j corresponded with a trial in which five to seven data-sets were taken during hemodynamic maneuver (as shown in fig. 6.3). Each data-set included simultaneous CABP assessments and ECG and BCG recordings, as was detailed previously. A healthy male of 33 years, 184 cms tall with a weight of 86 kg volunteered the trials after the respective informed consent was signed. The procedure of this study was approved and supervised by the Medical Review Committee of the Biological Engineering Department, Universidad de la República. The principles of the declaration of Helsinki were followed. The CABP was assessed non-invasively and intermittently from the shpigmoCor brachial cuff device using the PWA. BCG and ECG signals were recorded (with the proposed wearable device) simultaneously with the CABP assessments, and, as was mentioned, during the sub-diastolic recording period of each PWA assessment [21]. Every measurement was performed with the subject was relaxed at sitting up straight position.

Two group of data sets were acquired along day one, four on day two, and five data sets were acquired on day three, as shown in fig. 6.3. Hold and slow breathing, Hand-grip and Valsalva maneuvers were also carried out to produce BP fluctuations along the recordings and thereby obtain multiple CABP values along data-sets (See fig. 6.3).

6.1.3 Data processing

Ensemble averaging

Ensemble averaging technique was used to suppress the uncorrelated noise and artifacts, but also for preserving and enhancing the signal features extracted by signal processing. Although the data acquisition system provided a clean ECG waveform for all trials, the intrinsic nature of the BCG signal (small head-to-foot body accelerations were taken from a sensor) made the ensemble averaging

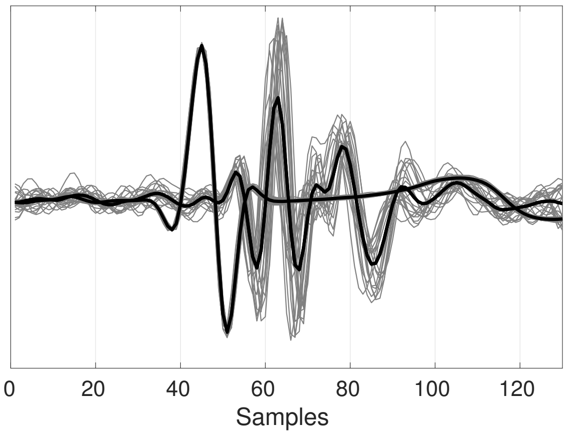

Figure 6.4: Averaging procedure: Construction of the (representative) beat-long waveforms from the ECG and BCG recordings on an arbitrary data-set. Acquired ECG and BCG signals (in grey) and averaged result in black.

a required technique to help with processing. Nonetheless, both signals, ECG and BCG, were treated with the same processing (averaging technique) to prevent inducing any phase lag between signals. The averaging was applied to the signals acquired during 20 s corresponding to the period used by the reference cuff-less device to provide an assessment. ECG R-wave was used as a reference point in the ensemble averaging; and, the variable beat length issue was not treated because of the proximity of the BCG J-wave to the ECG R-wave (less than 10% of the cardiac cycle). The averaging resulted in a representative waveform (for the ECG and the BCG) that lasts one cardiac cycle. Fig. 6.4 shows the averaging result for ECG and BCG waveforms on a particular data-set.

Feature time (FT) extraction

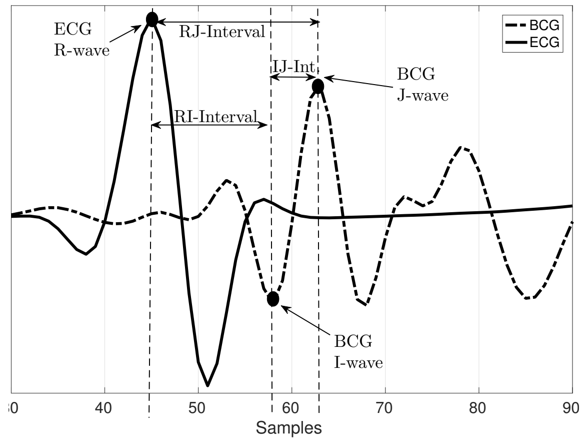

Figure 6.5: Feature time extraction on averaged ECG and BCG heartbeats

Averaged signals were used to extract the feature times (FT) that were used for the CABP estimation (see the following about the PTTBM CABP estimation) FT extraction was based on diverse literature findings of ECG and BCG acquisitions. I-wave was reported to indicate the initiation of the mechanical ejection from the heart to the aorta inlet [52]; thus, the pre-ejection period (PEP) could be estimated through the R-I interval. Additionally, the I-J interval was reported to be associated to a pressure pulse propagation time (PTT) at an aortic district [89], and, the R-J interval (RJ), which can be calculated as the sum of PTT and PEP, i.e., PAT, was published to correlate with CABP [69]. Hence, feature times (i.e., IJ, RJ, and RI) were directly extracted from ECG and BCG averaged signals. To do this, first, the ECG R-wave and BCG J-wave were determined using simple peak detection algorithms. Then, the BCG I-wave was detected as the local minimum just before the J-wave. Finally, the considered FTs were assessed by the following expressions, both designations for each FT shall be used indistinctly hereinafter.

$$RI = PEP = I_{wave} - R_{wave} \tag{6.1}$$

$$IJ = PTT = J_{wave} - I_{wave} \tag{6.2}$$

$$RJ = PEP + PTT = PAT = J_{wave} - R_{wave} \tag{6.3}$$

Where, X_{wave} in (6.1)-(6.3) indicates the sample position where the X_{wave} takes place on the averaged ECG or BCG signals. Figure 6.5 sums up the FTs extraction from representative signals. Finally, FT procedure upgraded each data-set by adding a paired FT (RI, IJ, and RJ) to the CABP snap-shot assessment and wearable recordings. Thus, each data-set is considered to include such fields hereinafter.

Pusle transit time based model (PTTBM) for the CABP estimation

In chapter 3 RJ-interval was proposed to estimate CABP. Strong correlations between CABP estimations and measurements were achieved by using the PTTBM in 6.4 and 6.5 [39] [69].

$$BP_{S_{FT}} = \frac{A_{S_{FT}}}{FT} + B_{S_{FT}} \tag{6.4}$$

$$BP_{D_{FT}} = \frac{A_{D_{FT}}}{FT} + B_{D_{FT}} \tag{6.5}$$

The PTTBM was extended here to be evaluated for CABP estimation by using not only with RJ (as input FT) but also with RI and IJ. Equations 6.4 and 6.5 were the PTTBM used to estimate systolic ($BP_{S_{FT}}$) and diastolic CABP ($BP_{D_{FT}}$) from a particular FT. $A_{S_{FT}}$, $B_{S_{FT}}$, $A_{D_{FT}}$ and $B_{D_{FT}}$ are constants tailored by curve fitting procedures over the different groups of data-sets(GR_j).

6.1.4 CABP Estimation: evaluation levels

The methodology was evaluated in two levels, which are based on how PTTBM parameters (in 6.4 and 6.5) were found and then used to estimate CABP over different groups of data-sets. The two levels are summarized in Figs. 6.6 and 6.7.

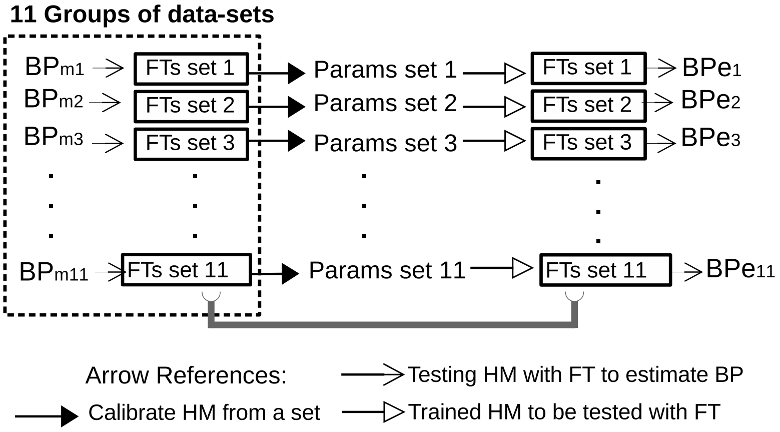

Figure 6.6: Evaluation Level-1 procedure to find the CABP estimations (BP_e). Measured CABPs (BP_m) from cuff-based device and FTs from wearable device, are part of each group of data-sets. The BP estimation model (PTTBM) is constructed/calibrated (parameters are resolved) and tested (calibrated PTTBM is evaluated to find BP_e) using the same data-sets

Evaluation level-1, when the model-parameters in the PTTBM were resolved using a particular group of data-sets (GR_j), then were used to find BP_e by testing the same data-setsgroup (GR_j) (Fig. 6.6). Such a simple approach might evaluate the feasibility of the method for the CABP prediction (i.e., PTTBM is constructed and tested using the same data-sets).

A moderate-hard evaluation for the proposed method was carried out by evaluating the capability of the calibrated PTTBM to accurately predict unseen CABP data. Thus, in this level-2 procedure, the evaluation of the CABP prediction/examination capability was based on the accuracy of the CABP estimations BP_e constructed by testing FTs in GR_i through the PTTBM being calibrated with data included in GR_j with $j \neq i$. In this study, parameters were resolved (calibrated) from the first group of data-sets GR_1 (which constituted a group of baseline-state data-sets) and then tested with the FTs on the other ten groups of data-sets. Figure 6.7 summarizes such Level-2 procedure adopted for constructing the CABP estimations (BP_e) in this work.

6.1.5 Data Analysis

The strength of association between cuff-based device and wearable device were assessed by Pearson correlation. Linear regression was also used to gauge the agreement of estimated CABP (BP_e) and measured CABP (BP_m) variables. The two-sample Kolmogorov-Smirnov test was used to evaluate if data in vectors BP_e

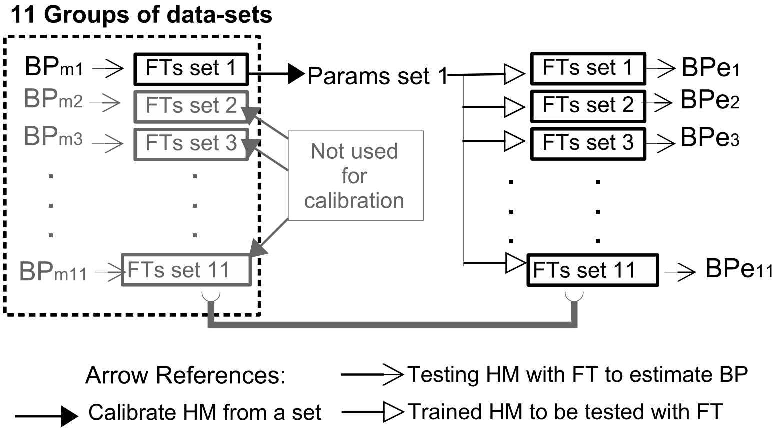

Figure 6.7: Evaluation Level-2 procedure to find the CABP estimations (BP_e). Measured CABPs (BP_m) from cuff-based device and FTs from wearable device, are part of each group of data-sets. The BP estimation model (PTTBM) is constructed/calibrated (parameters are resolved) with data in GR_1 and tested (calibrated PTTBM is evaluated to find BP_e) by using data in GR_j with j=2..11

and BP_m are from the same statistical distribution functions [90]. P-value (p) was taken two-tailed and p<0.05 was considered statistically significant. Agreement between devices was considered with a mean difference of BP_m and BP_e to be less than 5mmHg ($|\mu_e| < 5mmHg$), which is the current pass criteria for the bias error of the cuff-based BP estimation according to the Association for the Advancement of Medical Instrumentation (AAMI) [44].

6.2 Results

Sixty-seven data-sets (N=67) were acquired during the three days of study to evaluate the performance of the proposed method by the two degrees of rigorousness (sec. 6.1.4). The first evaluation (Level-1) provides an insight into the feasibility of the method for estimating CABP. Level-2 evaluation procedure features a more rigorous metric by evaluating the capability for predicting CABP from an initial calibration. Tables 6.1 and 6.2 summarize the performance of the presented method considering this two-level evaluation. The common figure of merits (FOMs) on the tables are: Correlation (r), slope (m) and intercept (y) from linear regression plots (Measurements vs. Estimation), and root-mean-square error (RMSE).

6.2.1 Method results: Level-1 evaluation

Level-1 procedure (PTTBM is calibrated and then CABP is estimated with the same group of data-sets) was used to construct CABP estimations (BP_e). Each calibration generates a pair of $A_{X_{FT}}$ and $B_{X_{FT}}$ parameters (see Fig. 6.6). Besides

Table 6.1: Performance table of the BP Models (eqs. 6.5 and 6.4) on the estimation of Central Aortic Blood Pressure through the different Featured Times (FT). Model constants are estimated through curve fitting routines using the discussed *Level-1* evaluation method

Mode	***Evaluation Level-1***						
FT	**RJ-interval**		**RI-interval**		**IJ-interval**		
CABP	**S**	**D**	**S**	**D**	**S**	**D**	**Units**
r	0.89	0.88	0.88	0.87	0.90	0.88	-
m	0.79	0.77	0.78	0.75	0.80	0.77	-
y	23.2	18	25	19	22	18.0	mmHg
RMSE	2.25	2.35	2.2	2.4	2.1	2.38	mmHg
$\frac{\sigma}{\mu}(A_{X_{FT}})$	758	450	887	430	944	735	%
$\frac{\sigma}{\mu}(B_{X_{FT}})$	119	524	64	187	80	104	%

including common FOMs (r, m, y, RMSE), table 6.1 summarizes the the PTTBM parameter scattering resulting from calibrations performed at each group of data-sets. $\frac{\sigma}{\mu}(A_{X_{FT}})$ and $\frac{\sigma}{\mu}(B_{X_{FT}})$ represent standard deviation of the parameter over the mean value of the parameter along the eleven trials. If the method had absolute time stability over the three days, $\frac{\sigma}{\mu}(A_{X_{FT}})$ and $\frac{\sigma}{\mu}(B_{X_{FT}})$ would be zero. Fig. 6.8 shows the evolution of the PTTBM parameters along different groups of data-sets. Scatter on parameters is written as a relative scatter (error) from the parameters resolved from the first group of data-sets. For instance, $\epsilon_{r1}(A_{S_{FT}j})$ in 6.6 shows the parameter $A_{S_{FT}}$ resolved at a particular GR_j and written as a relative error to the value of such parameter being resolved at GR_1.

$$\epsilon_{r1}(A_{S_{FT}j}) = \frac{A_{S_{FT}j} - A_{S_{FT}1}}{A_{S_{FT}1}} \tag{6.6}$$

Then, black dots in Fig. 6.8 are thus constructed by evaluating $\epsilon_{r1}(A_{S_{FT}j})$ along the eleven groups of data sets; similarly was proceeded for describing the relative scattering of the other parameters in 6.4 and 6.5. Accordingly, defined relative scatter is zero at GR_1 for all the parameters on the considered PTTBM.

6.2.2 Method results: Level-2 evaluation

Central aortic blood pressure estimations (BPe) were constructed by testing the groups of data-sets with the PTTBM being calibrated with the first-acquired group (see fig. 6.7). Table 6.2 includes the calibration parameters. Fig. 6.9 shows the mean of the estimation error segmented in days from its calibration.

6.3 Discussion

Evaluation level-1 procedure shows that the central CABP estimation might be feasible by the proposed methodology. Findings showed that always it is possible to find a pair of parameters to be used with PTTBM and the FT, to estimate a group

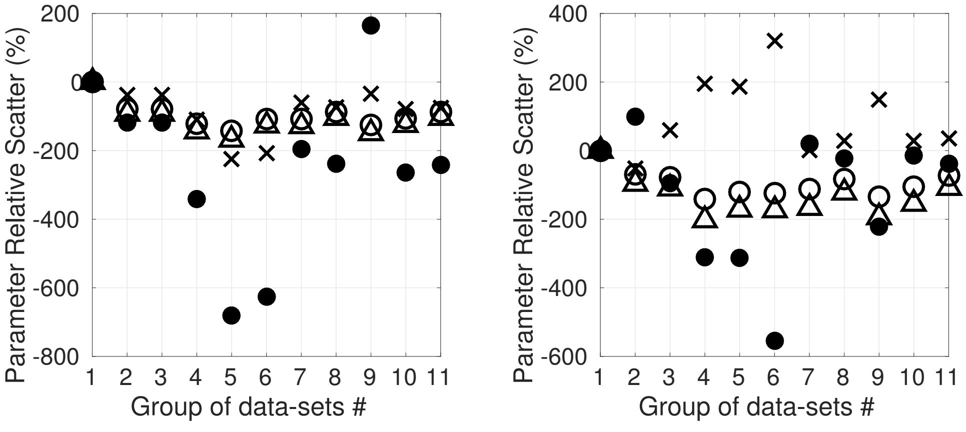

(a) CABP estimation from RJ

(b) CABP estimation from RI

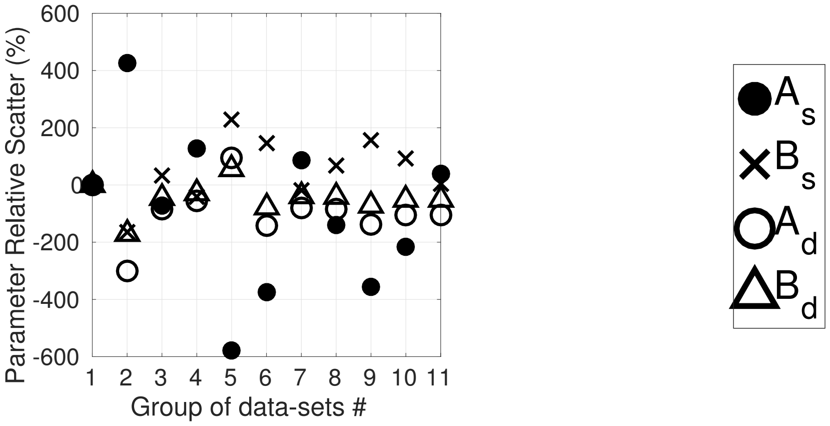

(c) CABP estimation from IJ

(d) Parameter Reference

Figure 6.8: Scattering of parameters of the used in CABP-PTTBM: evolution along the eleven groups of data-sets acquired during three days of intermittent assessment. Parameter variability is written as a relative scatter (error) from the parameters resolved from the first group of data-sets

of CABP values accurately. Additionally, evaluation level-1 showed that similar feasibility on CABP estimation could be achieved by considering all three FT alternatives (RJ, RI and IJ). CABP-PTTBM level-1 evaluation presents performances of $r \approx 0.9$ ($p < 0.05$), $m \approx 0.8$ and $y \approx 20mmHg$ and $RMSE \approx 2.3mmHg$. Similar results were reported in chapter 3 when RJ interval was used as input FT. Thus, the proposed wearable device was capable of achieving similar results that the ones obtained in the chapter 3 where acquisition was mainly based on using off-the-shelf equipment. This validation of the proposed wearable device represents one of the main findings in the study presented in this chapter. Furthermore, this work showed that more FT alternatives could be used for the CABP estimation from the proposed wearable device. When BP_e was constructed with

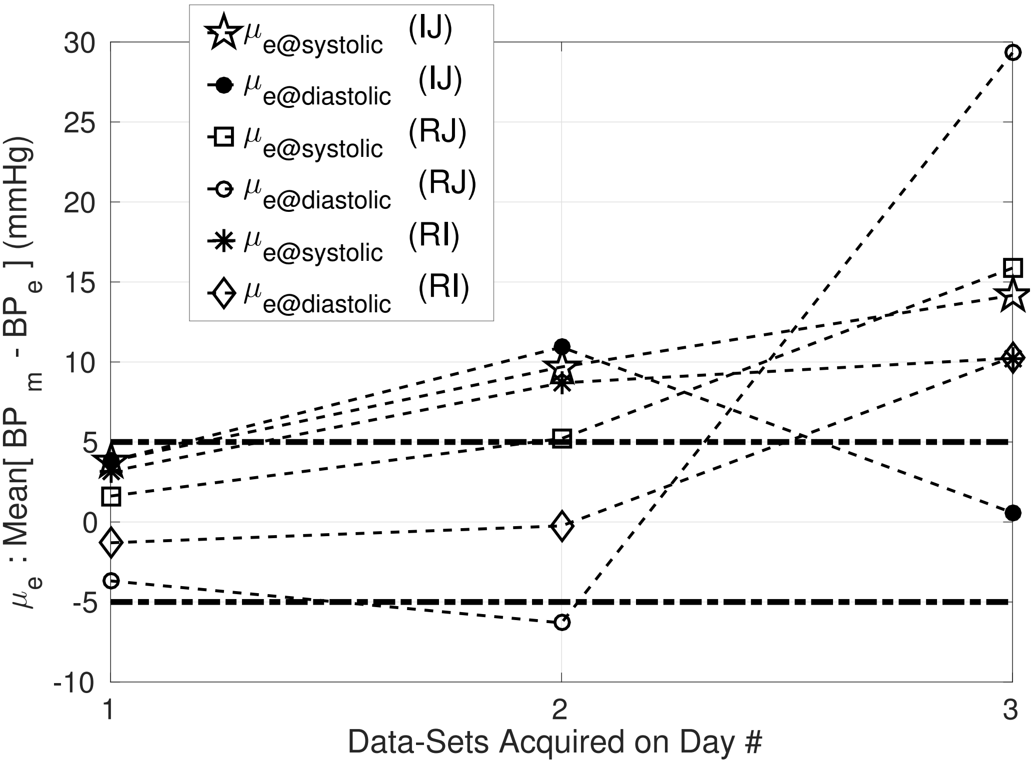

Figure 6.9: Estimation error evolution along days

Table 6.2: Performance table of the BP Models (eqs. 6.5 and 6.4) as estimators of Central Aortic Blood Pressure through the different Featured Times (FT). Model parameters were estimated through curve fitting routines using the discussed *Level-2* evaluation method.

Mode	***Evaluation Level-2***						
FT	**RJ-interval**		**RI-interval**		**IJ-interval**		
CABP	**S**	**D**	**S**	**D**	**S**	**D**	**Units**
r	0.14	0.04	0.3	-0.14	0.16	-0.27	-
m	0.04	0.01	0.09	-0.02	0.06	-0.02	-
y	113	80	106	83	103	84.6	mmHg
RMSE	9.6	6.2	7.1	5.9	5.0	8.2	mmHg
$A_{X_{FT}}$	6.15	-0.51	4.27	-0.18	-1.75	0.02	mmHg sp
$B_{X_{FT}}$	8.4	10.8	8.4	9.6	14.2	7.9	mmHg

the level-1 procedure, there was no statistical difference between BP_e and BP_m distributions functions for any of the studied BP variables, systolic ($p > 0.6$) and diastolic ($p > 0.3$), when different FT were considered (RI,RJ and IJ intervals). Nevertheless, although table 6.1 presents feasibility for the CABP estimation, and also for the three presented FT, calibrated constants $A_{S_{FT}}$, $B_{S_{FT}}$, $A_{D_{FT}}$ and $B_{D_{FT}}$ vary significantly along groups of data-sets. Parameter scattering of the PTTBM, measured in terms of sigma-over-mean (rows $\frac{\sigma}{\mu}(A_{X_{FT}})$ and $\frac{\sigma}{\mu}(B_{X_{FT}})$ in table 6.1), varies from 450 to 944 % for all over the $A_{X_{FT}}$ parameters, while from 64 to 524 % for the respective $B_{X_{FT}}$ counterpart. Scattering in parameters of the PTTBM can also be observed in fig. 6.8. Since parameters are resolved from curve fitting procedures over several grouped data-sets, with no additional constraints for the convergent solution, it is reasonable to expect some scatter on such best solutions for parameters. A more physical-assisted calibration approach might help reduce the scattering along with groups of data-sets.

On the other hand, when PTTBM was calibrated with the first group of data-sets, and then PTTBM attempted to estimate CABP along three days from calibration, CABP prediction presented poor performance. Negative and less than $r = 0.3$ Pearson correlations were obtained; almost zero slopes ($m \approx 0$) and intercepts larger than $y = 80mmHg$ resulted from linear regression analyses. Also, the two-sample Kolmogorov-Smirnov test rejected the null hypothesis of BP_e and BP_m being of the same distribution functions ($p < 0.001$) for the three considered FT cases. Last two rows on table 6.2 provides the calibration parameters ($A_{S_{FT}}$, $B_{S_{FT}}$, $A_{D_{FT}}$ and $B_{D_{FT}}$) used by the PTTBM to perform the CABP estimation. Aim to estimate CABP by the proposed method with a three-day calibration interval can not be achieved in the light of evidence found here. Nevertheless, fig. 6.9 shows that CABP estimations compliant with the AAMI bias requirements ($|\mu_e| < 5mmHg$) could be achieved by the proposed method by considering within-day calibration intervals.

6.4 Conclusion

The possibilities for estimating CABP from a proposed wearable device were investigated in this chapter. CABP estimation performance was assessed by using two levels of validation; that is, feasibility (Level-1) and prediction/examination capability (Level-2) on CABP estimation were reported. Investigation carried out in chapter 3 showed that CABP estimation from ECG and BCG is feasible, whereas findings in this chapter confirmed such results by using the proposed wearable device. The study used groups of data-sets (defined by CABP measurements and wearable acquisitions of ECG and BCG) from a healthy subject recorded along three days; favorable results were obtained when the method was calibrated and tested over the same group of data-sets (level-1 evaluation). In this context, extracted feature times from wearable acquired signals (intervals: RI, RJ, and IJ) might lead to three alternatives for estimating CABP from this proposed PTT-based methodology. The ability of the trained PTTBM to predict unseen CABP data was also evaluated (level-2 evaluation). CABP prediction from the proposed method showed poor performance when a three-day calibration interval was considered. Nevertheless, findings showed that CABP could be acceptably predicted employing daily calibrations.

6.4.1 Perspectives launched from this investigation

The findings presented in this chapter meant a first set of validations for the proposed methodology to estimate CABP from a wearable device. Validations within the chapter showed that CABP estimation might be feasible based on the level-1 type validation, but level-2 type validations showed that CABP estimations by using a beyond-day calibration interval are unfeasible. Therefore, next chapter validations are centered on such level-2 type evaluations but considering a shorter calibration interval, and also in a study involving more volunteers.

On the other side, the level-1 evaluation showed that the PTTBM calibrations based on tailoring the PTTBM through regression procedures might lead to parameters that fluctuate along with groups of data (even when data from the same subject was considered). Reducing the degree of freedom by including physical constraints in the curve fitting procedures might reduce the scatter of parameters in the PTTBM. Providing the PTTBM with the most physical considerations as possible would give more robustness to the method, and might provide better insights into the assessments of cardiovascular health. Development carried out in chapter 8 is centered on these concerns, where a novel PTTBM is proposed. Proposed PTTBM aims for estimating CABP from a fresh perspective based on central circulatory system modeling and, by using the proposed wearable acquisition conveniently since PTTBM leverages that wearable device was designed for capturing cardiovascular timing events with low delays.

Chapter 7

Wearable CABP Estimation: Final Validation

Rationale

Validations on the wearable version of the proposed method for estimating CABP (chapter 6) showed that the wearable approach could replicate the results that were achieved with off-the-shelf equipment, and thus, the method can be further validated by using the wearable device. In this chapter, the method validation is centered on the CABP estimation capability. The wearable acquisition of electrocardiogram (ECG) and ballistocardiogram (BCG) (chapter 4) was used to extract the three studied FTs (RI, RJ, and IJ intervals). Nine PTT based models (PTTBMs) proposed in the literature were applied to each FT as CABP estimating functions, and accordingly, the results were analyzed to check the suitability of these models (throughout the considered FTs) in order to predict CABP. PTTBMs were calibrated with data-sets acquired at baseline state, which were not considered for testing the PTTBM estimation performance, similar to the previously defined level-2 type procedure. Results showed that four of the nine tested models presented a proper agreement in estimating CABP through the acquired signals when considered (in the order of) an hour calibration interval after calibrated with baseline-state data. The PTTBM previously used (chapters 3 and 6) confirmed the fitting once again. Notwithstanding this, the present study revealed that a particular FT might lead to better CABP estimation from the proposed wearable device. The results were based on a trial with ten young, healthy volunteers who underwent different hemodynamic interventions, and, to our knowledge, this is the first time that CABP has been successfully estimated (predicted) from a wearable device. The chapter is organized as follows: trial procedures, acquisition details, and signal processing are summarized in section 7.1. Evaluated PTTBM and used FT are presented in section 7.2. Results and discussion are presented in sections 7.3 and 7.4, respectively; and, conclusions in section 7.5.

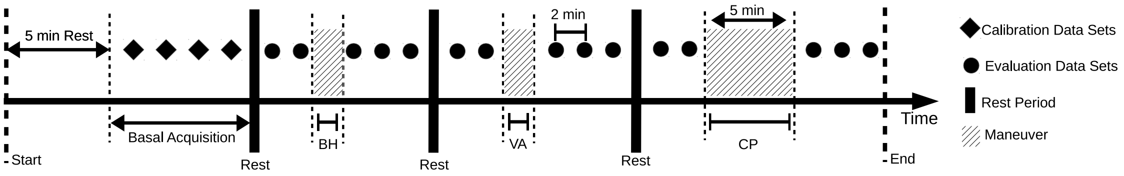

Figure 7.1: Acquisition procedure. Data-sets, as defined in 6.1.1, included simultaneous CABP snaptshot assessments and wearable ECG and BCG recordings. Dot and rhombus markers indicate a data-set collection event. Hatched boxes indicate a hemodynamic manoeuvre (BH: Breath Holding, VA: Valsalva, CP: Cold pressor)

7.1 Methods

7.1.1 Subjects

Ten young healthy volunteers (five females and five males) between 24 and 40 years old (mean 26 years, SD 7 years) were enrolled to participate in the study. The procedure was approved and supervised by the Medical Review Committee of the Biological Engineering Department. All individual participants included in the study provided written consent before experimentation, and the principles of the declaration of Helsinki were followed. During the measurements (unless stated otherwise), the room temperature was controlled at 24 °C.

7.1.2 Acquisition

Acquisition were performed by using SphygmoCor XCELL device and the custom wearable device (chapter 4) as presented in section 6.1.1

7.1.3 Protocol

Figure 7.1 summarises the whole protocol experienced by volunteers. A particular data-set, denoted with a marker (rhombus or dots in Fig. 7.1), includes pairs of ECG and BCG waveforms acquired by the wearable device and a CABP snapshot assessment with the SphygmoCor XCEL, as was defined in section 6.1.1 where considered ECG and BCG segments corresponded to the heartbeats during the sub-diastolic recording of a SphygmoCor assessment. For all assessments, data were acquired at the same sitting up straight position in order to lessen spurious responses induced by motion artifacts.

Participants were initially asked to rest at sitting up straight position to avoid corrupted BP readings by increased sympathetic activity. Then, around four to six data-sets were assessed after five minutes of that resting position to create a group of data-sets in basal-state. Such assessments are indicated with rhombus-shaped markers in Fig. 7.1. Then data was collected for three different hemodynamic maneuvers (indicated in Fig. 7.1 with hatched boxes). Each intervention was preceded by an initial baseline recording in which two assessments were acquired. Additionally, interventions were chosen to perturb BP by affecting cardiovascular parameters (stroke volume, total peripheral resistance, and heart rate) differently [42] [91]. In the first intervention, the subject underwent voluntary breath-holding (BH) until failure, BH was reported to cause BP perturbations [92] by affecting the heart rate, the cardiac output, and peripheral resistance [93] . The second intervention was carried out with a Valsalva maneuver (VA). Finally, each subject was asked to stay in a low-temperature room (14°C) for five minutes and returned to the controlled temperature room (24°C) to resume the acquisition, a procedure referred as cold pressor (CP) hereinafter.

7.1.4 Signal processing

Data-sets were grouped according to the maneuvers they came from (including the two basal previous-maneuver data-sets); thus, four groups of data-sets were created for each volunteer, these groups were, basal (GR_{BS}), breath-holding (GR_{BH}), Valsalva (GR_{VA}) and cold pressor (GR_{CP}). Then, the same signal processing as presented in the previous chapter was performed for each individual data-set at mentioned groups GR_{BS}, GR_{BH}, GR_{VA} and GR_{CP}. The signal processing is briefly reviewed.

Ensemble Averaging

Averaging technique was applied on the considered ECG and BCG signals segments (the 20s recorded segment within a data-set). Both signals, ECG and BCG, underwent the same averaging procedure, thus preventing a phase lag between them. This resulted in a representative waveform (for the ECG and the BCG) that lasts one cardiac cycle. Fig. 7.2a shows the averaging result for ECG and BCG waveforms on a particular data-set. FT extraction were performed on the averaged signals.

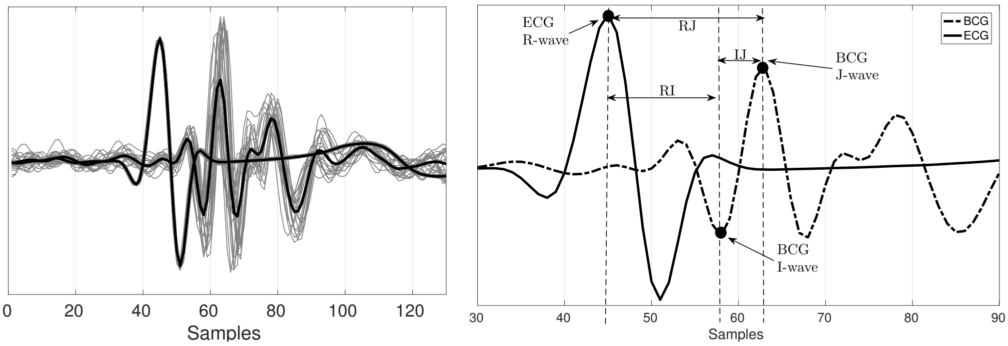

(a) Ensemble averaging (b) Feature time extraction

Figure 7.2: Signal processing over the physiological signals. (a) Example of ensemble averaging results. Acquired ECG and BCG signals (in grey) and averaged result in black. (b) Feature time extraction on averaged ECG and BCG heartbeats.

Feature Time Extraction

Averaged signals were used to extract the feature times (FT) that were used for the CABP estimation. The FTs considered in this chapter (as was for the previous chapter) were the intervals defined by the R-wave (ECG), J-wave (BCG) and I-wave (BCG) taken in pairs, i.e., R-I, R-J, and I-J intervals (RI, RJ, IJ from now on). Fig. 7.2b summarizes the FT extraction procedure over the averaged ECG and BCG waveforms included in a data-set. The procedure generated paired FTs and data-sets data, which were treated as an extended data-sets of paired data. Extended data-set included: the CABP snapshot assessment[systolic, diastolic], 20-sec of wearable signals recorded [ECG, BGC], and the respective FT extraction [RI, RJ, IJ].

7.1.5 Calibration of PTTBM parameters

A total of nine PTTBMs were considered to evaluate their ability to predict CABP readings after being calibrated. In section 7.2, the PTTBMs analyzed in this work are listed, which are expressed as a function of FT and model parameters. Accordingly, calibrated PTTBMs were obtained by adjusting such model parameters with regression procedures over the group of data-sets acquired at baseline state (see rhombus-shaped markers in Fig. 7.1), that were, data-sets on GR_{BS} . The CABP estimation capability of each calibrated model was evaluated on unseen CABP assessments (dot markers in Fig. 7.1), thats were, groups GR_{BH}, GR_{VA} and GR_{CP}. Additionally, the calibration data-sets (GR_{BS}) were not considered for testing the PTTBM estimation performance (see section 7.3).

7.1.6 Data analysis

Statistical Analysis

Agreement and association between the cuff-based assessment and the cuff-less, wearable, estimation were assessed by Bland–Altman (BA) analysis and Pearson correlation (r), respectively. Agreement analysis was performed, including the 95% confidence interval (CI) [94]. Association for the Advancement of Medical Instrumentation (AAMI) requirements was considered for the mean estimation error (μ) to be lower than 5 mmHg with a standard deviation of the error (σ) below 8 mmHg. Linear regression was used to gauge the association between estimated and measured BP readings.

7.2 PTT based models (PTTBM) for BP estimation

PTT-based models presented in this section are mainly based on the previously introduced Moens-Kortweg equation, eq. 7.1, which establishes that in an elastic tube (vessel) with laminar fluid (blood) flow, pulse wave propagation velocity (PWV) along the tube wall depends on fluid properties (ρ: density), and, tube geometry (h: thickness, r: radius) and elasticity modulus (E). Being the latter in turn, a BP-dependent quantity, which could be approximated by 7.2 at central elastic arteries [38].

$$PWV = \frac{D}{PTT} = \sqrt{\frac{Eh}{2\rho r}} \tag{7.1}$$

$$E(P) = E_0 e^{\alpha P} \tag{7.2}$$

where $\alpha = 0.017\, mmHg^{-1}$ and E_0, positive quantities, model the arterial stiffening depence with BP (referred as P in 7.2). The equations give the insight that BP and the propagation time (PTT) for a pressure pulse to travel along a predefined distance (D) on the arterial tree are inversely related. Several proposed models for this inverse relation are described.

PTTBM1: BP logarithmic in PTT

The first PTT-based model analysed is directly derived from by combining 7.1 and 7.2 as seen in [95].

$$BP = A \log(PTT) + B \tag{7.3}$$

Despite being popular and directly derived from main equations, low suitability for BP estimation it has been reported [96].

PTTBM2: BP Linear in PTT

By linearising the model in 7.3 a linear dependence is found.

$$BP = A.PTT + B \tag{7.4}$$

The model was reported to be applicable to several manoeuvres and under drug administration [97], and provided accurate BP estimations in [95] [97]

PTTBM3: BP Linear in PTT^{-1}

The linear PTT-based model in 7.5 explicitly states the expected inverse dependence between BP and PTT.

$$BP = \frac{A}{PTT} + B \tag{7.5}$$

The model was already introduced and used previously, and a derivation of this PTTBM could be found in [39], which is recommended for the BP estimation due to the trade-off between complexity (only two parameters needed) and accuracy (potential errors at low PTT). PTTBM3 was used in chapters 3 and 6 and, in [69] for the CABP estimation, and in [98] for the peripheral BP (PBP) estimation, proving the feasibility of the method in acquisitions during physical exercise.

PTTBM4: BP quadratic in PTT^{-1}

A quadratic model in PTT^{-1} 7.6 is proposed in [67] which is derived from energy balance considerations for the blood flow.

$$BP = \frac{A}{PTT^2} + B \tag{7.6}$$

PTTBM5: BP logarithmic and quadratic in PTT^{-1}

In [53] a novel PTTBM was proposed, which resulted in a nonlinear, two-term, PTT-dependence 7.7, 7.8. It is noteworthy that, PTTBM5 admits reasonably dispense with subject-dependent coefficients as used in [99]. Thus, calibration can be carried out with only one assessment/data-set (calibration provides the terms with zero-subscripts in 7.7 and 7.8).

$$DBP = MBP_0 + \frac{2}{\alpha}\log(\frac{PTT_0}{PTT}) - (PP_0/3)(\frac{PTT_0}{PTT})^2 \tag{7.7}$$

$$SBP = DBP + PP_0(\frac{PTT_0}{PTT})^2 \tag{7.8}$$

where, SBP, DBP and PP refers to systolic BP, diastolic BP and pusle pressure (PP= SBP - DBP), respectively

PTTBM6: BP logarithmic and quadratic in PTT^{-1}

This PTTBM keeps the dependence of PTTBM5, while considering parameters to be mathematically fitted instead of based on physiological considerations (as was the case in PTTBM5).

$$DBP = C_D + B_D\log(\frac{1}{PTT}) - \frac{A_D}{PTT^2} \tag{7.9}$$

$$SBP = DBP + \frac{A_S}{PTT^2} \tag{7.10}$$

PTT-based models Featuring Heart Rate

Since it is known that BP is strongly associated with heart rate (HR), and it is reported [100] that the inclusion of HR in PTTBMs may improve the accuracy of the BP estimation, some of the aforementioned PTTBMs are extended by including a HR dependency [101].

PTTBM7: PTTBM1 featuring HR

In [100] several PTTBMs with embedded HR are tested for the S-BP estimation, and 7.11 showed the best performance.

$$BP = A\log(PTT) + B\log(HR) + C \tag{7.11}$$

PTTBM8: PTTBM2 featuring HR

In [101] is proposed to include an HR term from 7.4, and results showed that a precision inside AAMI requirements was achieved when a calibration interval of one hour was considered.

$$BP = APTT + BHR + C \tag{7.12}$$

PTTBM9: PTTBM4 featuring HR

Finally, PTTBM4 was also embedded with HR.

$$BP = \frac{A}{PTT^2} + \frac{B}{HR^2} + C \tag{7.13}$$

PTT-based models Coefficients and FT-Inputs

Parameters A, B, C at PTTBMs are all subject-specific coefficients that are tailored from calibration procedures. The sign of the parameters resolved from the calibration must be consistent with the inverse relationship between PTT and BP.

Regarding the FT (noted as PTT in the previous model descriptions), although PTTBMs were derived from arterial pulse propagation time principles, some works have reported the convenience of including PEP in the cuff-less BP estimation. Thus, all PTTBMs were evaluated not only using PTT (IJ) as an input FT but also using the RJ-interval (i.e., PTT + PEP) and using the PEP (RI) as input FT. Therefore, PTTBM performance on CABP estimation is evaluated along the presented nine models with three FTs in the role of PTT: IJ, RJ, and RI, as defined in sec. 7.1.4, totaling 27 modeling alternatives to be evaluated.

7.3 Results

A total of ten subjects underwent the three mentioned hemodynamic interventions, generating N=185 data-sets to evaluate (along groups of data-sets GR_{BH}, GR_{VA} and GR_{CP}) the PTTBMs performance to predict CABP. Data-sets in GR_{BS}, used for calibration, were not included in the following evaluation in order to mimic the actual monitoring system application (evaluation level-2 procedure). Table 7.1 summarises the performance of the above discussed PTTBMs to track systolic and diastolic CABP varibles (S-CABP and D-CABP). The most promising PTTBMs were identified based on the following key figures of merit: mean (μ) and standard deviation (σ) of the estimation error and Pearson correlation (r).

The first four PTTBMs (PTTBM1 to PTTBM4, corresponding to 7.3-7.6, with RI as input FT, presented the best performances for S-CABP and D-CABP estimation, especially from a precision and association perspective. Such best performances are further analyzed on table 7.2 for S-CABP and D-CABP estimations, respectively. The following characteristics are evaluated: linear Regression (LR) parameters (slope (m) and intercept (y)), 95% confidence interval (CI) of the mean error, percentage of data-base with error within limits of agreement

Table 7.1: Estimation performance for Systolic CABP (S-CABP) and Diastolic CABP (D-CABP) along PTTBMs and FTs

		S-CABP Estimation			D-CABP Estimation		
PTTBM	FT	μ	σ	r	μ	σ	r
1	IJ	-2.5	9.2	0.70**	-2.6	11.4	0.64**
	RJ	-0.2	7.7	0.60**	1.0	8.2	0.62**
	RI	0.8	5.5	0.82**	1.3	6.8	0.77**
2	IJ	-2.7	10.9	0.68**	-2.8	12.8	0.61**
	RJ	0.1	7.4	0.63**	1.3	8.3	0.61**
	RI	0.9	5.5	0.82**	1.3	6.6	0.78**
3	IJ	-2.5	9.2	0.70**	-2.4	10.3	0.66**
	RJ	-0.7	8.4	0.56**	0.8	8.1	0.63**
	RI	0.7	5.5	0.81**	1.3	7.0	0.77**
4	IJ	-2.5	8.9	0.69**	-2.4	9.4	0.67**
	RJ	-1.1	9.5	0.49**	0.6	8.1	0.64**
	RI	0.5	5.7	0.81**	1.3	7.3	0.61**
5	IJ	-2.8	27.6	-0.2*	0.3	15.1	0.12^{NS}
	RJ	-0.2	15.7	0.22*	1.0	8.9	0.54**
	RI	0.7	15.6	0.44**	1.6	9.4	0.62**
6	IJ	9.9	64.1	0.09^{NS}	12.6	62.5	0.12^{NS}
	RJ	2.7	13.0	0.41**	3.7	9.9	0.57**
	RI	14.3	73.1	0.21*	14.8	79.1	0.25**
7	IJ	-1.5	6.8	0.76**	-3.5	12.0	0.64**
	RJ	1.1	8.1	0.59**	0.0	8.1	0.63**
	RI	3.8	9.6	0.64**	1.4	8.4	0.74**
8	IJ	-1.6	7.1	0.76**	-4.0	13.6	0.61**
	RJ	1.4	8.2	0.58**	0.2	8.1	0.62**
	RI	3.8	9.3	0.65**	1.4	8.3	0.75**
9	IJ	-1.7	7.0	0.71**	-2.9	10.0	0.67**
	RJ	0.3	8.7	0.55**	-0.5	8.2	0.62**
	RI	0.3	8.7	0.55**	1.6	9.1	0.72**
UNITS		mmHg		–	mmHg		–

^{NS} Not Significant * $p < 0.01$ ** $p < 0.001$**

(LOA) (defined as $\mu \pm 1.96\ \sigma$), root mean square error (RSME) and mean absolute difference (MAD) [17]. Finally, the strength of association between the axes of Bland-Altman (BA) plots (Pearson correlation on BA r_{BA}) was also evaluated to check for systematic error.

Table 7.2: Estimation performance for Systolic CABP (S-CABP) and Diastolic CABP (D-CABP) for the first four PTT-based models (PTTBM1 to PTTBM4) when RI interval is used as input feature time

	PTTBM	m	y	Confidence Interval μ		LOA	Error		r_{BA}
				CI-	CI+		MAD	RMSE	
S-CABP	1	0.81	19	0	1.5	96	4.4	5.5	0.02
	2	0.81	19	0	1.7	96	4.4	5.6	0.01
	3	0.80	20	-0.1	1.5	95	4.5	5.6	0.02
	4	0.80	21	-0.3	1.4	95	4.5	5.7	0.01
D-CABP	1	1	-1	0.3	2.3	93	5.2	6.9	-0.37
	2	1	-1	0.4	2.3	92	5.2	6.7	-0.36
	3	1	-1	0.3	2.3	93	5.3	7.1	-0.38
	4	1	-2	0.3	2.4	93	5.4	7.4	-0.41
UNITS		–	mmHg			%	mmHg		–

7.4 Discussion

The central investigation on this chapter was the validation and exploration of the proposed approach to estimate CABP from the presented wearable device; the findings, in turn, lead to the development of a feature time-based methodology to predict aortic BP variables from the proposed wearable device, which provided accurate CABP estimations after a simple calibration procedure with baseline-state data-sets. Noteworthy, this work tested the performance of some (previously reported and tested mostly for PBP estimation) PTT-based models to evaluate here their suitability for the CABP estimation. This approach might be more suitable since the main equations of the PTTBM derivations assumes an elastic artery district to be evaluated [8] [38], and this hypothesis might not be completely fulfilled as the considered arterial segments reach the periphery. This final validation, even though involved only a few volunteers, provides the relevant intermediary results for the development of the proposed approach for estimating CABP, which undoubtedly serves as an orientation for future efforts in order to achieve an improved wearable CABP monitoring device.

Even though most of the prior works have used the PTT-based method to estimate systolic BP [39], findings showed that a D-CABP estimation within AAMI requirements could be achieved by using this methodology. Nevertheless, consistent with these prior works, results showed better suitability of the methodology for S-CABP than for D-CABP estimation, especially from the accuracy and association perspectives. Accordingly, in many situations, uncorrelated systolic and diastolic behavior is expected, which would prevent systolic and diastolic variables from being estimated from the same FT [42]. Regarding PTTBMs and FTs, S-CABP and D-CABP estimations from PTTBM1 to PTTBM4 using RI as FT showed agreement, strong correlation, and a small mean difference between cuff-based and wearable devices. Otherwise, opposed to what has been reported in the literature [100] for the case of PBP, the inclusion of the HR term in PTTBM1, PTTBM2, and PTTBM4, with RI as FT, degraded the CABP prediction capability. The HR inclusion was beneficial only for the S-CABP estimation when using IJ (which corresponds to PTT in the aortic domain) as input FT. However, it should be noted that the calibration procedure plays a fundamental role in the estimations achieved and discussed here. This work aims to present results when a simple systematic calibration is performed by using only a few data-sets acquired at baseline state. Such kind of calibration is suitable for a final wearable product where calibrations could be periodically performed based on a few reference measurements.

Our findings show the beneficial contribution of RI for aortic BP estimation. Published evidence [52] reports that RI corresponds approximately with PEP. PEP, and thus RI, is an FT lacking any pulse transit time assessment. Therefore, this suggests that such estimations are based on principles that are not the ones that support the PTT-based method. We argue that it might be due to a significant dependence of the BP on the myocardial contractility at the aortic inlet region. This conjecture stems from the fact that such a region is directly exposed to forces exercised by the myocardium, and PEP has been reported to be a surrogate measure of myocardial contractility [102] [103]. This deserves further analysis, which is out of the scope of the study presented, however it will be revisited in chapter 8 .

In order to illustrate the performance of the four PTTBMs that showed better suitability for the CABP estimation, PTTBM2 (with RI as FT) was selected to be further analyzed. Figs. 7.3a-7.4b present LR and BA plots for CABP variables. The suitability of this method can be observed from the figures mentioned above. In Figs. 7.3a and 7.3b, the LR lines (continuous) are very close to the ideal identity lines (dashed). Moreover, only few data-sets are outside standard margins of error ($\mu \pm 1.96\sigma$) on BA analyses (Figs. 7.4a and 7.4b). Additionally, associations between BA axis magnitudes are shown with a continuous line at both BA analyses. The BA correlation shows a defined trend in the case of D-CABP, suggesting a slight, systematic, method error, which is consistent with the worse performance achieved in D-CABP estimation concerning the S-CABP estimation.

One of the critical aspects of the FT-based approaches is the calibration interval of the PTT-based models, i.e., the period after a calibration procedure in which the method is capable of accurately tracking BP (CABP in this work). A theoretical study [5] indicates that PTT-based methods might achieve a maximum calibration period of about one year; despite the PTT-based method might achieve seemingly high measurement errors due to random error components which intrinsically affect the method [5]. Such fluctuations are responsible for much smaller calibration intervals (in the order of seconds to minutes according to [5]), especially when accuracy is tested by using AAMI protocol. In [104] a method to evaluate the calibration interval of the (PTT-based) BP estimation accuracy is proposed. However, such method is not directly applicable to this study, because it relies on processing the information on a very frequent (beat-to-beat or similar) basis. In this case, a measure of calibration interval for the CABP measurement

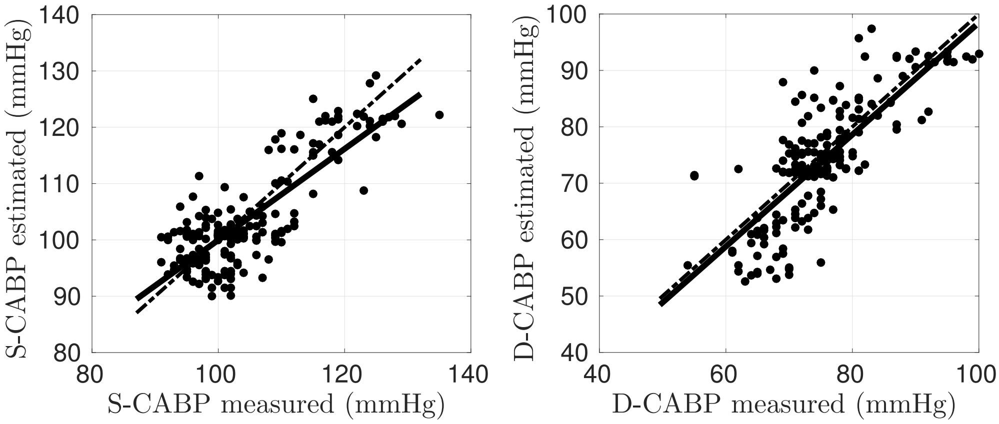

(a) LR for S-CABP Estimation (b) LR for D-CABP Estimation

Figure 7.3: CABP: Linear regressions (LR) plots for PTTBM2 with RI as a input FT

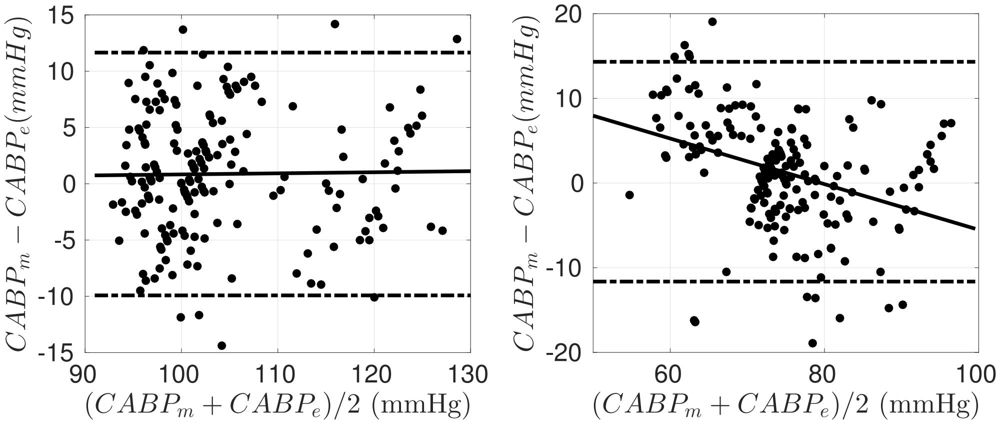

(a) BA for S-CABP Estimation (b) BA for D-CABP Estimation

Figure 7.4: Bland-Altman (BA) analysis for PTTBM2 with RI as a input FT

accuracy can be derived as follows. Unseen data-sets, acquired during 74 ± 20 minutes during all maneuvers, were estimated accurately within the scope of the AAMI requirements. Therefore, it can be considered that the proposed methodology, guarantees at least a mean calibration interval of about 74 min. Furthermore, by extrapolating the estimation error trend up to the acceptable accuracy limit (AAMI limits, 5 mmHg), a rough estimation for the calibration interval can be constructed, which, on average, may ensure accurate CABP estimations within two hours from a calibration. Further, such calibration interval may be conservative since accuracy assessed through AAMI protocol could be rigorous (for the PTT-based methods) in order to screen hypertension [5].

7.5 Conclusion

The presented investigation explored 27 alternatives (nine PTTBMs along three FTs) for the CABP estimation from the proposed wearable, ECG and BCG based methodology. Data were obtained from ten volunteers during three different hemodynamic interventions. The R-I interval emerged as the best surrogate for CABP estimation. Prior works establish that the R-I interval coincides approximately with the pre-ejection period. This suggests that a principle different from the traditional PTT-based method might be advantageous for central aortic BP assessment. Four PTTBMs proved to be suitable for CABP monitoring after a simple calibration procedure with baseline state data. These are: PTTBM1 (logarithmic in RI), PTTBM2 (linear in RI), PTTBM3 (linear in 1/RI) and PTTBM4 (quadratic in 1/RI). The calibration interval admitted at least one hour of accurate estimations compliant with AAMI requirements, which may be useful for applications requiring short term, continuous BP monitoring at central aortic domains.

Chapter 8

The Beginning.... at Last

Rationale

Results obtained in the validation chapters (6 and 7) showed that the proposed method might be capable of estimating central aortic blood pressure (CABP) by using the wearable device presented in chapter 4. Nonetheless, new questionings aroused during such validation stages.

- Chapter 7 showed that RI-interval, an FT lacking any pulse transit time assessment, served as the best surrogate for CABP. Thus, the CABP estimation is not based, in this case, on the PTT principle (as was initially intended).
    - Could it be that the principle used (CABP estimated through RI) can be leveraged by the PTT-method to obtain better CABP estimation?
- Results in chapter 7 showed better suitability of the methodology for systolic than for diastolic estimation. It is known that eventual systolic and diastolic miscorrelations may exist (see Fig. 8.1), which would prevent such both variables from being estimated from the same FT [42].
    - Is it possible to address such a miscorrelation issue (between aortic diastolic and systolic BP) and construct a better estimation for both variables?
- Regarding the parameter scattering (of PTT-based models, PTTBM) throughout calibrations observed in chapter 6, then:
    - How could the parameter scattering be reduced?
    - Could the used method be beneficiated by including more physical constraints on its implementation?
    - How could be incorporated more physical considerations to the proposed methodology to estimate CABP?

The concerns mentioned above were the inspiration for the creation of the material presented in this chapter, in-which, a novel PTTBM suitable for the CABP estimation is presented. This chapter presents some novel ideas to estimate CABP in this proof of concept material in-which the preliminary validations showed the novel PTTBM is promising to resolve some of the questions mentioned above. *The beginning* of the development of a novel PTTBM for the CABP estimation, based on the physical modeling of the central circulatory system, arouses in this thesis... *at last.*

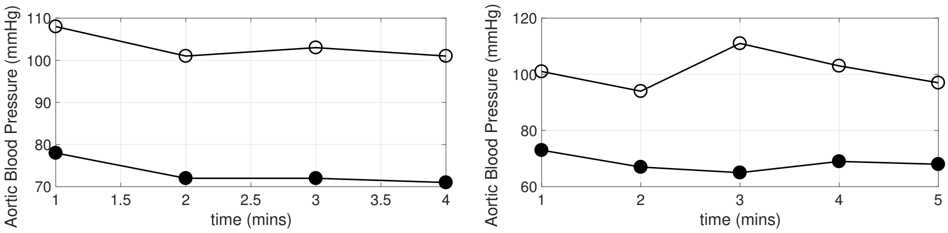

(a) sCBP and dCBP Correlated (b) sCBP and dCBP Uncorrelated

Figure 8.1: Correlated and miscorrelated evolutions of aortic systolic (sCBP: white circles) and diastolic (dCBP: black circles) blood pressures on the same subject

8.1 Introduction

Figure 8.2 shows the left ventricle (LV) pressure-volume loop diagrams (PV-Loops) as can be found in literature [105] [106]. PV-Loops fig. 8.2 include some quantities typically used to study the LV-function [105] [6] and LV-aorta coupling [107], such as end-systolic pressure-volume relationship (ESPVR), end-diastolic pressure-volume relationship (EDPVR), afterload, and aortic elastance (E_a). Notably, changes on the slope of curves of ESPVR and E_a are associated with changes in ventricular contractility [107] and aortic distensibility, respectively. PV-Loop on the left represents a baseline situation for the LV-aorta system from which such a system will be perturbed (to illustrate potential changes of CABP). The PV-Loop on the upper right shows the baseline system state after being suffering an increase in myocardial contractility. Baseline PV-Loop (light-gray trace) along with contractility-increased PV-Loop (dark-gray black trace) were superimposed in order to show the changes due to the perturbation. The increased contractility resulted in an increased afterload, which, in turn, lead to an increased CABP.

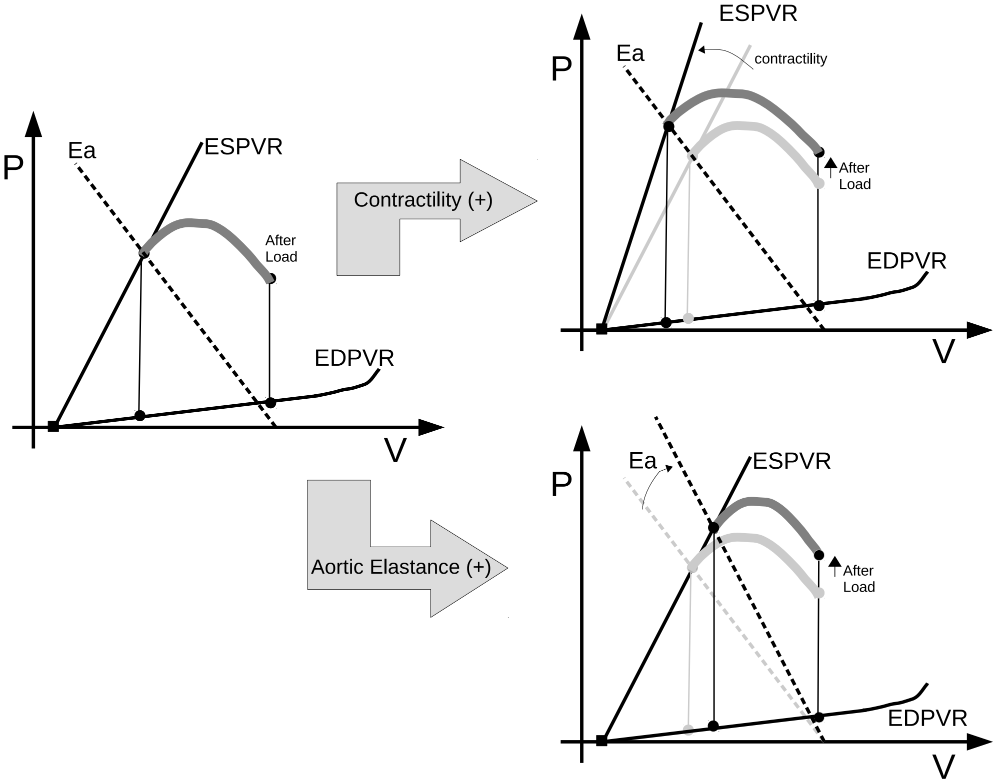

Figure 8.2: Left ventricle (LV) pressure-volume loop (PV-Loops) diagrams showing the effects that an increased myocardial contractility and aortic compliance lead to an increased afterload

On the other side, a similar analysis could be performed to the PV-Loop on the lower right, which shows the response of the system at a basal state (light-gray PV-Loop) against an increment on the aortic elastance. Perturbed system (dark-gray black PV-Loop) shows an increased afterload, which again, lead in an increased CABP.

Therefore, both, contractility and elastance, considered effects acting to the LV-Aorta system, affected directly the aortic blood pressure. On the other hand, the classical PTT-based methods based on exploiting the elastance-BP relationship, aim to estimate BP by using PTT as a surrogate which a prioiri would assess BP by screening only elastance changes. PTT estimation could lead to an insufficient mechanism to estimate BP.

The proposed PPTBM aims to exploit the two discussed effects to create a estimation of the CABP, by using information provided by indirect assessments of contractility and elastance. The contractility could be indirectly assessed by using the RI-interval (RI) since, RI coincides approximately with the pre-ejection period (PEP) [52] which has been reported of being a biomaker of the myocardial contractility. The elastance, on the other hand, could be assessed via PTT, likewise classical PTT methods, since, as was mentioned, such methods are based on exploiting the PTT-(arterial)Compliance-BP relationship.

The indirect blood pressure estimation

Figure 8.3 shows a scheme of the typical BP estimation by using PTT based models. Classic PTT-based approach is shown on the left, whereas the proposed approach on right.

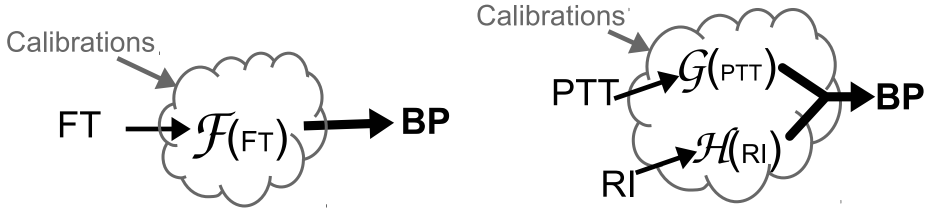

Figure 8.3: Scheme of an BP estimation through PTT-Method (left) and by the proposed method (right).

Classical PTT-based approaches for estimating BP have been based on using a particular featured time (FT such as PTT, PAT, PEP) and a function F (of such FT) in order to construct a BP estimation. Function F represents a PTT based model, which includes few parameters that are resolved through calibrations by fitting the PTTBM with BP data. Notably, the methods used in chapters 6 and 7 of this document have followed such an approach for estimating CABP. Furthermore, some methods have used PAT for estimating BP, such FT includes the PEP along with a PTT counterpart, and have received mixed reviews regarding the suitability of using such type of FT for estimating BP, even being a topic of controversy on the state-of-the-art [67] [59]. By collating such PAT-approaches against the ideas presented in this chapter, it seems to be feasible that such PAT-based BP estimation has shown accurate results since such BP estimation might be contractility-based rather than PTT-based as it is widely presumed [59]. In effect, results in chapter 7 showed that the best CABP estimations were achieved by a contractility-based (that is, RI-based) approach when compared against the results obtained by PTT-based along with PAT-based estimations. Nonetheless, when the PAT-based approach is used, both discussed mechanisms are merged into the FT, which may not be the best way to treat such FT as a PTTBM input in order to achieve accurate BP estimations.

As will be detailed later, the proposed PTT based model for estimating CABP aims to contemplate the two mentioned effects (that are, the BP dependence on contractility and elastance) in order to improve the CABP estimation. As will be shown, the required FTs (PTT and RI) will be served separately in different sections of the proposed PTTBM (into the functions G and H, respectively, at Fig. 8.3) in order to construct the BP estimation. Eventually, the proposed PTTBM requires being calibrated, which, similarly to the classic PTTBM calibrations, is also based on resolving internal parameters by fitting BP data. The development of the proposed PTTBM is presented in the next section.

8.2 Proposed CABP estimation model

8.2.1 Windkessel theory as development substrate

The framework for developing the proposed PTTBM is based on the Windkessel theory, which is a lumped modelling approach for describing the hemodynamics on the arterial system [108]. The formulation of the model described the heart and the systemic arterial system similarly to a hydraulic circuit. In this analogy (Fig. 8.4a), a water source (blood) is pumped through a pulsatile pumping (heart) to a chamber which is filled with water except for an air region. The pulsatile pumping compresses the air in the chamber, which serves as a cushioning reservoir or *windkessel* [6] and then, it pushes the water out of the chamber. Thus, a steady water flow is obtained at the back-end despite a pulsate water pumping at the front-end. This analogy resembles to the arterial-heart bio-mechanics, since the arterial tree acts as the mentioned windkessel in which pressure increases as blood is pumped into it, but the pumping in turn is damped by the elastic arteries (mainly the aorta) which stores blood during systole and expels it during diastole, thus resulting in a rather constant (steady) flow at very distal arteries.

Windkessel models are commonly used to relate the blood pressure and blood flow in the aorta (shown in fig 8.4b), by characterizing parameters that defines the hemodynamics. Particularly, the two-element windkessel model uses the following parameters:

- Arterial Compliance (C_a): refers to the compliant or extensible characteristic of the arteries. Even though the compliance of all individual arteries are lumped in this parameter, the largest arteries are responsible for this characteristic. The arterial compliance seen from the aortic root could be roughly estimated from the following equation

$$C_a \approx \frac{SV}{sCBP - dCBP} \tag{8.1}$$

where, SV refers to the stroke volume and, sCBP (dCBP) refers to the systolic (diastolic) central aortic blood pressure.

- Total vascular systemic resistance (R_a): Represents the resistance that opposes to the flow of blood along the arterial tree. Even though the smaller arteries at peripheral offers the largest resistances, this lumped parameter aim to condense all the individual resistances found along the arterial three.

  The total vascular systemic resistance seen from the aortic root could be roughly estimated from the following equation.

$$R_a \approx \frac{mCBP}{CO} \tag{8.2}$$

  where, CO refers to the cardiac output, $mCBP$ refers to the mean aortic blood pressure, and, venous pressure was neglected to achieve 8.2.

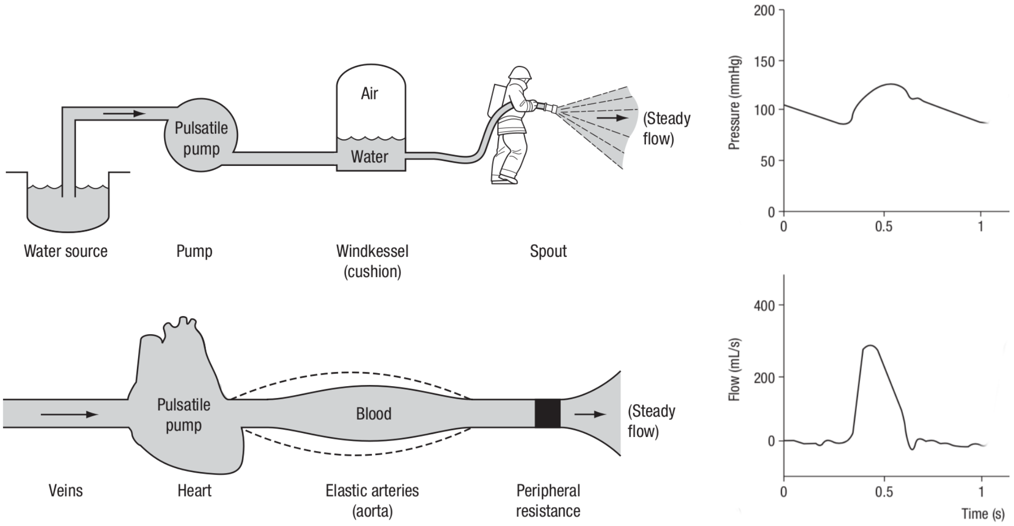

(a) Graphical interpretation

(b) Typical blood flow and pressure at ascending aorta

Figure 8.4: The Windkessel model. (a): Hemodynamics through windkessel theory and its hydraulic circuit analogy. The hydraulic circuit contains a water pump connected to a chamber filled with water except for a pocket of air. As it is pumped, the water compresses the air, which serves as a cushioning reservoir or "windkessel" and then pushes the water out of the chamber. Windkessel models the distensibility of the arteries, whereas the fire hose nozzle models the peripheral resistance. The circuit achieves steady-state water flow from a pulsatile pumped system. Constant flow is required by the fire-man end of the hydraulic chain. (b): Shows typical hemodynamics at the aorta root. Figures extracted from [6]

8.2.2 Electrical equivalent

The described hydraulic analogy for the windkessel effect, showed that the effect implements a low-pass-filtering between front-end pumped input and the steady flow at the back-end. Eventually, such analogy also admits an electrical circuit representation [108], which is constructed by using electric quantities and components in the role of the principal hemodynamic actors. That is, the electrical equivalent for the two-element windkessel model uses voltages and currents to represent blood pressures (in $mmHg$) and blood flows (in cm^3/s or mL/s), and, a capacitor (C_a) and a resistor (R_a) in the role of the arterial compliance (C_a in $cm^3/mmHg$) and total vascular systemic resistance (R_a in $mmHgs/cm^3$). The circuit shown in Fig. 8.5 is used in this chapter to study the hemodynamic near the aorta root, where a current driven two-element windkessel network is considered. That is, it uses a current source ($i(t)$) as input which mimics the blood flow ejected from the left ventricle into the aorta, and will be referred as central aortic blood flow (or $Flow$) in the next section. Thus, the time-varying voltage at the output node $v_a(t)$ mimics the central aortic BP waveform which will be the target quantity.

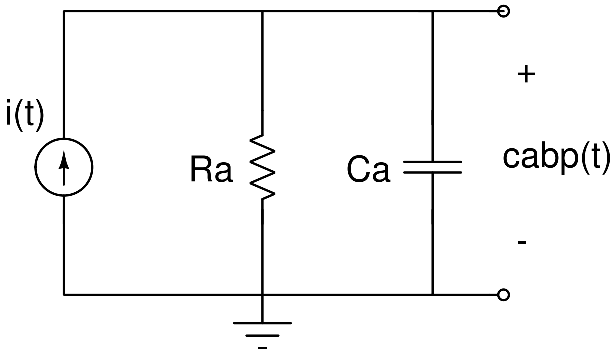

Figure 8.5: Windkessel electric equivalent model. Current source ($i(t)$) mimics the blood flow from the left ventricle ejection, the capacitor mimics the arterial compliance ($C_a = 1/E_a$), and, the resistance (R_a), the total vascular systemic resistance.

The proposed PTTBM developed in this chapter aims to find the electric components previously described, these are, R_a, C_a and $i(t)$, by processing the ECG and BCG signals acquired with the wearable device (chapter 3). Given that such three elements, along with the Windkessel substrate theory, establish an environment full of physiological meaning for the development of this proposed PTTBM, it is worth to mention that, it may be crucial that the FT acquisition (from ECG and BCG signals) preserves the physical meaning of such represented quantities. In effect, such concern was contemplated from the conception of the proposed wearable device, as presented in chapter 3, remaining so the consistency of the whole development presented within this thesis. Finally, the presented $i(t)$, C_a and R_a elements are proposed to be estimated as follows.

8.2.3 Estimation of the current source element ($i(t)$)

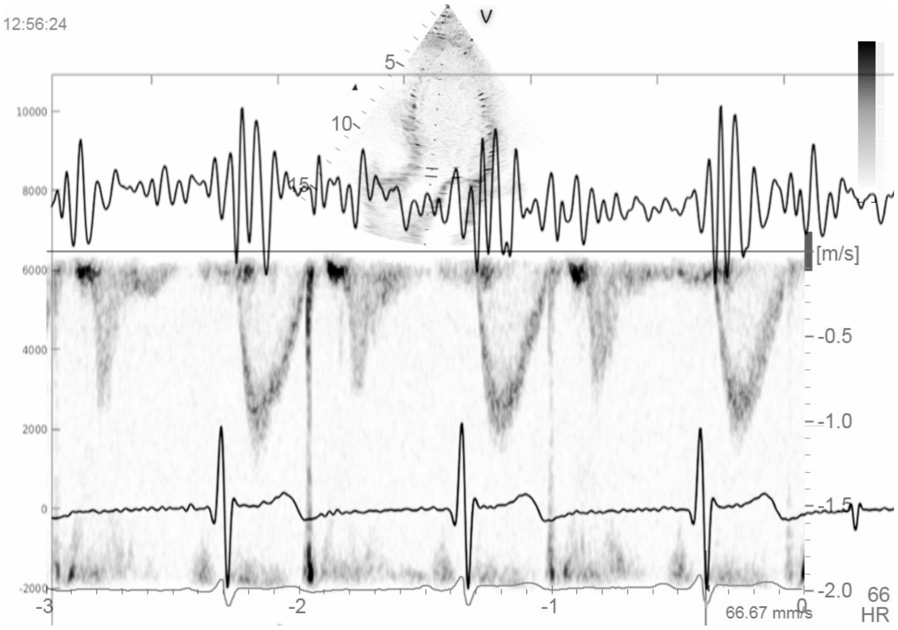

(a) Echo-Doppler ultrasound (General Electric, Vi-vidIq), and wearable ECG and BCG acquisitions.

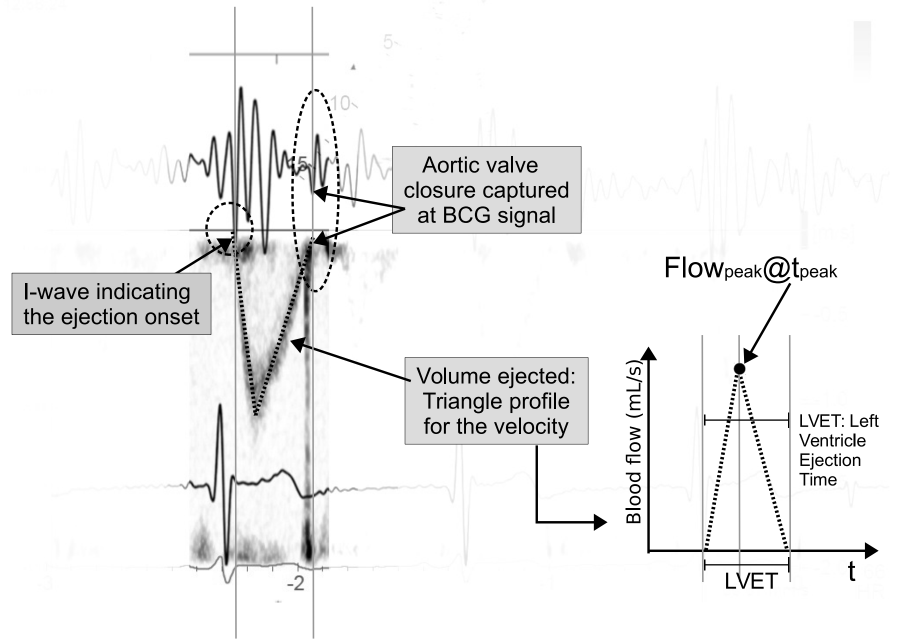

(b) Analysis of synchronized events acquired with the echo-Doppler and wearable ballisto-cardiogram. Blood jet velocity is approximated by a triangle [109]

Figure 8.6: Pulse wave Doppler signal at the left ventricle in a volunteer. Wearable electrocardiogram and ballistocardiogarm waveforms are superimposed in the figure

The central aortic blood flow profile was previously approximated by a triangular-shaped profile leading to accurate pulse wave velocity estimations [109]. Such approximation was used to estimate the profile of the current source element (representing, central aortic blood flow), which drives the two-element Windkessel model (fig. 8.5). Thus, the problem of finding an adequate current source element was reduced to find a proper base (b = LVET: LV ejection time) and height (h=$i(t)_{peak}$) of the mentioned triangle-shaped profile.

The base of the triangle-shaped blood flow was determined by leveraging from the parasitic coupling of the Seismo-cardiogram (SCG, considered as the dorso–ventral thoracic accelerations during the cardiac cycle) signal over the BCG waveform [110]. In effect, some SCG coupling on the proposed wearable BCG acquisition was detected, which was exploited by this method. The slight component of the SCG coupled on BCG allowed to estimate the aortic closure time (AC) [111], and thus the LVET was estimated as the time elapsed between the BCG I-wave and the AC (LVET $\approx$ AC - I-wave) [111] [52]. Figure 8.6a shows the simultaneous acquisition of the signals ECG and BCG by using the proposed wearable device presented in chapter 4, along with, a Doppler echo-cardiograph (General Electric, VividIq) sensing the LV blood flow activity. In effect, the expelled blood flow from LV into the aorta confirmed on a healthy volunteer, the expected triangle-shaped profile for the aortic blood flow given by the echo-Doppler image. Figure 8.6b summarizes the mentioned estimation for the base of the triangle-shaped blood flow (LVET), which was obtained by further processing the BCG signal [111] [52].

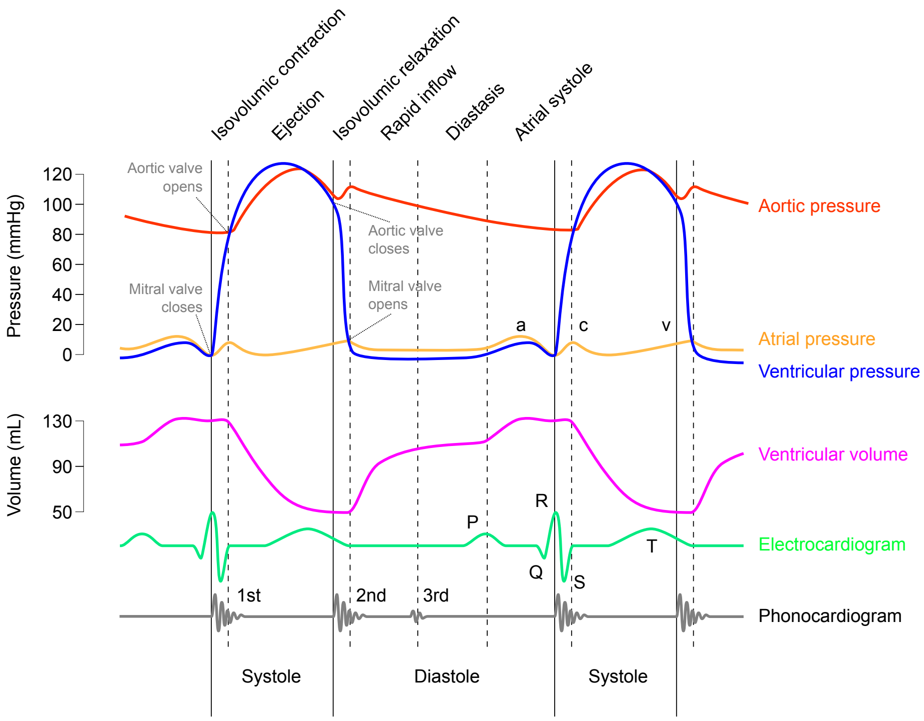

Figure 8.7: Wiggers diagram. Image extracted from [112] .

In order to find the peak of the triangle-shaped aortic flow ($Flow_{peak}$ on fig. 8.6b, or equivalently as a current element, $i(t)_{peak}$), the blood flow generation is further investigated/modeled. Figure 8.7 shows a typical Wiggers diagram [112] which compiles the time series of some physiological magnitudes during the cardiac cycle. Particularly, the aortic pressure and ventricular pressure are relevant for this work since such pressures are related the LV ejection. That is, when LV pressure exceeds aortic BP, aortic valve opens up and blood flow is established into the aorta from LV. The time variation of the LV pressure is given by the LV elastance variation (E(t)) for a constant (blood-filling) volume (iso-volumetric contraction stage).

Myocardium contraction is responsible for the elastance variation of the LV. In general, E(t) curve preserves a basic shape where each peak occurs near the end of the ejection phase regardless of the cardiovascular (CV) variability [113]. Accordingly, the E(t) peak value (E_{max}) refers to the previously introduced quantity end-systolic pressure-volume relationship (ESPVR) which, as mentioned is the conventional index to assess the heart contractility [107]. In [114] is proposed a periodic "double-Hill" function to give an analytical expression for the E(t) (8.3).

$$E(t) = \alpha E_{max} \left[\frac{\left(\frac{t}{\alpha_1 T}\right)^{m_1}}{\left(1 + \frac{t}{\alpha_1 T}\right)^{m_1}} \right] \left[\frac{1}{\left(1 + \frac{t}{\alpha_2 T}\right)^{m_2}} \right] + E_{min} \tag{8.3}$$

E(t) is written in terms of the cardiac period (T), a scaling factor (α) to ensure E_{max} happening, and, some dimensionless factors to model the contraction (α_1,m_1) and relaxation shapes (α_2,m_2) [115]; typical values for such values could be found in [114]. In this work is proposed to linearize the E(t) shape near the ejection onset, in which the LV pressure change rate could be estimated by $\partial P_{LV}/\partial t \approx (dCBP - Preload)/PEP$, therefore E(t) leads in eq. 8.4. Where, $Preload$ is considered as the end-diastolic LV pressure, EDV stands for the LV end-diastolic volume and, q_0 stands for the EDV by discounting the LV unstressed volume (V_{uns}), that is $q_0 = EDV - V_{uns}$. More generally, $q(t)$ is defined as the left ventricle blood filling volume but discounting the unstressed volume, $q(t) = LV_{vol}(t) - V_{uns}$.

$$E(t) \approx \frac{Preload}{EDV - V_{uns}} + \left(\frac{dCBP - Preload}{PEP\,(EDV - V_{uns})} \right) t = \frac{Preload}{q_0} + \left(\frac{P_0}{q_0\,PEP} \right) t \tag{8.4}$$

On the other hand, a pressure gradient is established across the aortic valve at the ejection onset, which induces the blood flow. The effective valve area, smaller than the cross-sectional areas of the LV or aortic root, represents a bottleneck for the blood flow (fig. 8.8a), and a pressure drop results across the valve, mainly at rapid ejection phase (as can be seen in fig.8.7 where aortic pressure during ejection is a bit lower than the ventricular pressure.). Therefore, by putting together the above mentioned effects, left ventricle and aortic valve will be electrically modelled with a time-variable capacitor [115] and a diode with a series resistance, respectively. Figure 8.8b shows the electrical equivalent circuit considered for the left ventricle and the systemic arterial system seen from the aortic root (R_a and

C_a); electrical voltages $v_{LV}(t)$ and $v_a(t)$ represent respectively the pressures at LV and aortic root (Volts as mmHg), and, the current $i(t)$ indicates the blood flow at aorta (Amps as mL/s). Appendix A shows the creation of this current driven Windkessel network system in order to simulate the BPs and Flows (as voltages and currents respectively) behaviour in an Electronic Design Automation (EDA) tool.

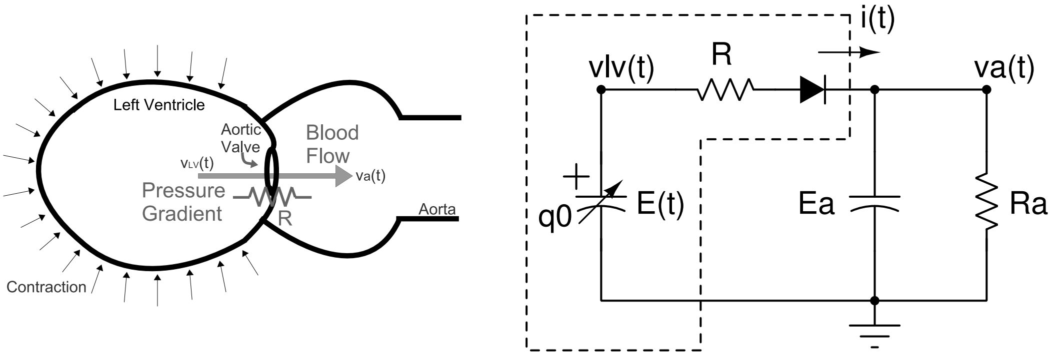

(a) Flow through aortic valve - Sketch

(b) Blood flow modeled at aortic root

Figure 8.8: Physical interpretation of the aortic valve resistance (R). The small valve area generates a bottleneck for the blood flow (fig. 8.8a), which is modeled by an ideal diode with a series resistance (fig. 8.8b). The flow depends on the resistance to the flow (R) along with the applied pressure gradient [116]. A variable capacitor models the left ventricle contraction. Pressures and blood flow are represented by voltage and currents (respectively) in the electrical representation. Where, $v_{LV}(t)$ and $v_a(t)$ refer to the left ventricle and the central aortic blood pressure, respectively, $i(t)$ refers to the aortic blood flow and, q_0 is the end-diastolic volume by discounting the LV unstressed volume. Elements in the dashed box are responsible for the blood flow into the vascular system. Aortic compliance (1/Ea) and total vascular systemic resistance (Ra) are represented by a capacitor and resistor, respectively.

The equations of the presented CV system at the onset of the ejection are:

$$v_{LV} = E(t)\left(q_0 - \int_0^t i(t)dt\right) \tag{8.5}$$

$$i(t) = \frac{v_a}{R_a} + \frac{1}{E_a}\frac{\partial v_a}{\partial t} \tag{8.6}$$

$$v_{LV} - v_a = Ri(t) \tag{8.7}$$

Where, 8.5, 8.6 and 8.7 constitutes a set coupled ordinary differential equations. In order to identify the maximum relative value for i(t), 8.7 is differentiated and equaled to zero (8.8).

$$R\frac{\partial i}{\partial t} = \frac{\partial v_{LV}}{\partial t} - \frac{\partial v_a}{\partial t} = 0 \tag{8.8}$$

$$\longrightarrow \frac{\partial i}{\partial t} = \frac{\partial v_{LV}}{\partial t} - \frac{\partial v_a}{\partial t} = 0 \tag{8.9}$$

Despite being considered a linearized expression for E(t) (eq. 8.4), it still can not achieve a compact closed-form expression for the solution of the differential equation in 8.9, which is the goal of this section. In order to come by with a compact solution for the problem of 8.8, some approximations were further considered. For instance, since systemic arterial impedance comprise a capacitive-resistive bank, the maximum of blood flow (current) advances the maximum of blood pressure (voltage). Therefore, near the slope-zero region for i(t) (that is, the region of interest), it was considered that capacitors nodes are being charged/discharged at approximately at constant current, and thus implies voltages variations with an almost constant slope. Additionally, the current across resistive components was neglected during such transient. Thus, by trying an approximately constant solution for i(t)≈ (I_t) in the system defined by 8.5- 8.7, results in 8.10.

$$RI_t \approx \left[\frac{Preload}{q_0} + \left(\frac{P_0}{PEPq_0}\right)t\right][q_0 - I_t t] - [dCBP + I_t E_a t] \tag{8.10}$$

the system returned an approximated expression 8.11 for i(t) (by solving 8.10 for I_t).

$$i(t) \approx I_t = \frac{\left(\frac{P_0}{PEP}\right)t}{R + (E_a + E_0)t + \frac{P_0}{PEPq_0}t^2} \tag{8.11}$$

Then, by using I_t (approximation of $i(t)$) on 8.5 and 8.7, an approximation[1] for $v_{LV}(t)$ and $v_a(t)$ could be also constructed as showed in the following expressions:

$$v_{LV}(t) \approx V_{LVt} = \left[\frac{Preload}{q_0} + \left(\frac{P_0}{PEPq_0}\right)t\right][q_0 - I_t t] \tag{8.12}$$

$$v_a(t) \approx V_{at} = [dCBP + I_t E_a t] \tag{8.13}$$

Then, the problem 8.8 was evaluated by differentiating 8.12 and 8.13, and, by considering an approximately constant value for I_t as was previously used (that is, near enough the sought $i(t)_{peak}$ region, where $i(t)$ presents the slope zero condition, it would be valid to try a constant solution I_t as rough approximation of $i(t)$)

$$\frac{\partial v_{LV}}{\partial t} - \frac{\partial v_a}{\partial t} = 0 \longrightarrow \frac{P_0}{PEP} = (E_0 + E_a)I_t + 2\frac{P_0}{PEPq_0}I_t t \tag{8.14}$$

Also, by considering a dominant denominator root (DDR: $\tau_1 >> \tau_2$) structure for I_t, and then linearizing (LIN) it in the region of interest (REG) nearby to the maximum extreme.

---

[1] Electrical magnitudes in capital letters with t-subscript stand for an approximation of such magnitude written in lowercase. For instance, I_t represents an approximation of $i(t)$

$$I_t = \frac{q_0 t}{t^2 + (\tau_1 + \tau_2)t + \tau_2\,\tau_1} \overset{\text{DDR}}{\approx} \frac{q_0 t}{t^2 + \tau_1 t + \tau_2\,\tau_1} \overset{\text{REG}}{\approx} \frac{q_0}{(t + \tau_1)} \overset{\text{LIN}}{\approx} \frac{q_0}{\tau_1}\left(1 - \frac{t}{\tau_1}\right) \tag{8.15}$$

$$\tau_1 = PEP(E_0 + E_a)q_0/P_0 \tag{8.16}$$

$$\tau_2 = R/(E_a + E_0) \tag{8.17}$$

$$\frac{\partial v_{LV}}{\partial t} - \frac{\partial v_a}{\partial t} = 0 \longrightarrow \begin{cases} t_{peak} \approx \tau_1/2 \\ I_{peak} \approx \frac{2(E_0+E_a)q_0P_0}{4P_0R+3q_0PEP(E_0+E_a)^2} \end{cases} \tag{8.18}$$

As shown in fig. 8.9b, the approximation obtained for $i(t)$ (I_t) underestimated the blood flow peak ($i(t)_{peak}$) by an 18%. Eventually, an underestimation on $i(t)_{peak}$ was expected since $v_a(t)$ was overestimated by its respective approximation V_{at} which led to an underestimated $i(t)$, see Figs. 8.9. Then, a parametric analysis in PEP, performed by the EDA tool (used as a differential-equation solver), showed that this under-estimation (in the blood flow peak) remained approximately constant by sweeping PEP around 50 % its nominal value (fig. 8.10a), considered sweep has a physiological sense according to the expected fluctuations of PEP in a human CV system. Figure 8.10b shows the $i(t)_{peak}$ swept in PEP variable, superimposed with the approximated solution for blood flow peak increased in an 18 % ($1.18 * I_t$). The relative error of this latter estimation was also included in fig. 8.10b, showing that a bounded relative error (6 %) could be archived by the proposed approximation along the considered swept range of PEP.

Finally, regarding the construction of a triangle-shaped aortic blood flow. Flow peak, that is, $Flow_{peak}$ or $i(t)_{peak}$, was used to estimate the height of such flow through the equation 8.19. That is, 8.19 includes the maximum of the approximated expression for $i(t)$ (I_t in eq. 8.18) and the following factors: the adjustment factor ($k_{adj} = 1.18$), and, k_{ej} which represents a dimensionless factor with a nominal value of *one*. k_{ej} will be one of the parameters to be tailored through calibration procedures on the proposed PTT-based estimation model. On the other hand, t_{peak} in 8.20 was used as an estimation for the time where blood flow peak occurs (relative to the onset of the aortic flow, where $Flow_{onset} \approx$ BCG I-wave [52]).

$$i(t)_{peak} = 1.18\,k_{ej}\,\frac{2(E_0 + E_a)q_0P_0}{4P_0R + 3q_0PEP(E_0 + E_a)^2} \tag{8.19}$$

$$t_{peak} \approx \tau_1/2 = 1/2\,PEP(E_0 + E_a)q_0/P_0 \tag{8.20}$$

8.2.4 Estimations of the two-elements Windkessel parameters

Aortic Compliance

Aortic compliance (C_a) element at the Windkessel network was derived from the Bramwell-Hill equation [9] that was introduced in chapter 2. The Bramwell-Hill

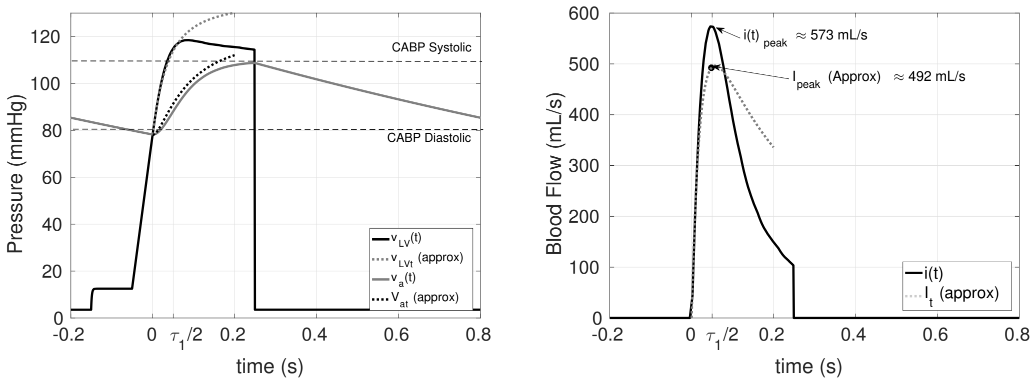

(a) Pressures near the aortic valve (b) Blood flow at aortic valve

Figure 8.9: Transient simulations for the hemodynamics near the aortic valve. The current source driven two-element Windkessel network was simulated from the electronic dual circuit by using CADENCE EDA tools. The proposed simulated electronic circuit can be found in appendix A, where node voltages and currents represent blood pressures and flows, respectively. Continuous traces represent the result from the EDA transient simulation, while dashed lines are the estimations from the math presented in this section. Estimation traces start at the onset of the aortic valve opening.

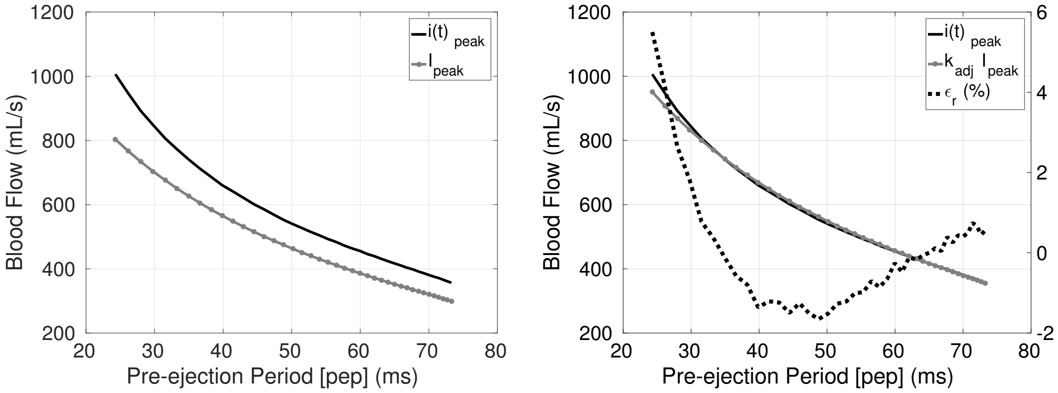

(a) Parametric analysis in PEP for $Flow_{peak}$ (b) $Flow_{peak}$ offset compensation

Figure 8.10: Parametric analysis performed in the transient simulation described in 8.9. Peak of the blood flow ($Flow_{peak}$ or $i(t)_{peak}$) was swept in the Pre-ejection period (PEP) variable. Both, simulation ($i(t)_{peak}$ in black) and estimation (I_{peak}) through the presented math (gray) curves showed approximately the same shape, excepting an gain error of about 18% (fig. 8.10a). Systematic gain error is compensated in fig. 8.10b, by multiplying $Flow_{peak}$ estimation by k_{adj} (=1.18). The relative error in the (gain) corrected $Flow_{peak}$ estimation (dashed line) is less than 5%.

equation in 8.21 determines the propagation speed (PWV) of a pressure pulse travelling along an artery by using the cross sectional arterial compliance along with other cardiovascular parameters.

$$PWV = \sqrt{\frac{A}{\rho C_{as}}} \tag{8.21}$$

where, (if an aortic segment is considered).

$$A: \quad \text{Aortic cross-sectional area} \tag{8.22}$$

$$C_{as} = \frac{\partial A}{\partial P}: \quad \text{Aortic cross-sectional compliance} \tag{8.23}$$

$$\rho: \quad \text{Blood density} \tag{8.24}$$

$$PWV: \quad \text{Pulse wave velocity at aorta} \tag{8.25}$$

Moreover, if PWV were assessed by measuring the pulse transit time (PTT) throughout an aortic distance L. Then, the Bramwell-Hill equation in 8.21 leads to 8.26.

$$\longrightarrow C_{as} = \frac{A}{\rho(\frac{L}{PTT})^2} \tag{8.26}$$

Equation 8.26 links the cross-sectional compliance (C_{as}) with the PTT, which would determine C_{as} from a PTT assessment if CV parameters ρ, L, and A were available. Eventually, some limitations exist on this approach for estimating aortic compliance (C_a) that should be noted. Firstly, parameters ρ, L, and A are unknowns, which should be found some-how in order to use 8.26. Then, parameters C_a and C_{as} refers to different quantities to characterize the aortic distensibility, since they differently refer to volumetric and cross-sectional quantities, respectively. This work considered that the sectional compliance (C_{as}) was proportional to the required aortic compliance (C_a) by an adequate subject-specific longitude factor (l_0) as shown in 8.27.

$$C_a = l_0 C_{as} = \frac{l_0 A}{\rho(\frac{L}{PTT})^2} \tag{8.27}$$

Then, the aortic compliance was estimated by the following equation.

$$\longrightarrow C_a = k_c \left(\frac{l_0 \frac{A_i + A_a}{2}}{\rho L^2} \right) PTT^2 \tag{8.28}$$

As was considered for the current source element, k_c represents a dimensionless parameter to be tailored from the calibrations procedures. The parameter is intended to provide an aortic compliance (C_a) estimation from the wearable assessed PTT. Regarding the unknowns ρ, L, and A (the latter considered as the average of sectional areas of the aorta at the root (A_i) and the arch (A_a)); typical cardiovascular magnitudes will be used for resolving such unknowns in 8.28. Even though the unknowns are subject-dependant parameters, the eventual errors produced by this approximation are intended to be masked out inside the adjustment parameter k_c. Further, all subject-dependant unknowns on the other considered elements (current source $i(t)$ and systemic arterial resistance R_a) were treated in the same way, that is, being resolved by using typical quantities, in order to provide a biasing point for the Ca, R_a and $i(t)$ elements being estimated by only using the acquired FT. Equation 8.29 shows the biasing magnitudes considered for the compliance element, where, the average ascending aorta cross-section $(A_i + A_a)$, aortic root-to-arch distance (L), and typical blood density were extracted from table (8.3). As considered for the k_{ej}, the seed/nominal value for tailoring k_c (eq. 8.29) was set as *one*.

$$\frac{l_0\frac{A_i+A_a}{2}}{\rho L^2} \approx \frac{(100cm)(6.8cm^2+5.07cm^2)/2}{(1060kg/m^3)(12cm)^2} = 5.18k\frac{cm^3}{mmHgs^2} \tag{8.29}$$

Arterial Resistance

Blood pressure regulation mechanism is provided by the baroreflex activity, which gives feedback to the central nervous system about the hemodynamic status. By manipulating the cardiac output and, mainly, the vascular resistance, the BP is maintained inside the target values [8]. Total systemic arterial resistance is the only hemodynamic parameter unavailable by any measurement of the proposed approach. Nevertheless, given that arterial resistance is responsible for fast regulation of BP, R_a was considered proportional to the cardiac period (T) because of a T enlargement might decrease BP; and empirically, R_a presented better adjustments when considered inversely-related with PEP.

$$R = k_r\left(\frac{PEP_{nom}}{T_{nom}}\right)\frac{T}{PEP} \tag{8.30}$$

As was considered for the other parameters, k_r represents a dimensionless quantity, manually adjusted to fit in equation 8.30 with a unitary value. Parameters with *nom* subscripts stands for nominal values, which can be found in table 8.3.

8.3 Methods

Methods to evaluate the proposed PTTBM were based on the ones presented in chapter 6; for instance, the data and its manipulation procedure was as described in section 6.1, with a difference in the feature extraction. Figure 8.11a shows the feature extraction (over the averaged ECG and BCG signals) used in this chapter. The most significant peak on BCG waveform during the recoil of ECG T-wave was considered as an estimation of the aortic valve closure event (AC), and, the time elapsed between I-wave and AC (on BCG waveform) was included as one of the extracted FTs (as long as, RI, IJ and RJ intervals); such FT was used as a surrogate of the left ventricle ejection time (LVET) (fig. 8.11a).

An estimation of the blood flow jet velocity at the aorta was constructed from the extracted FTs by using the proposed methodology (8.2.2); systemic arterial resistance (R_a), and aortic compliance (C_a) were also estimated. Then, the CABP waveform was constructed from blood flow, R_a, and C_a by using the Euler method

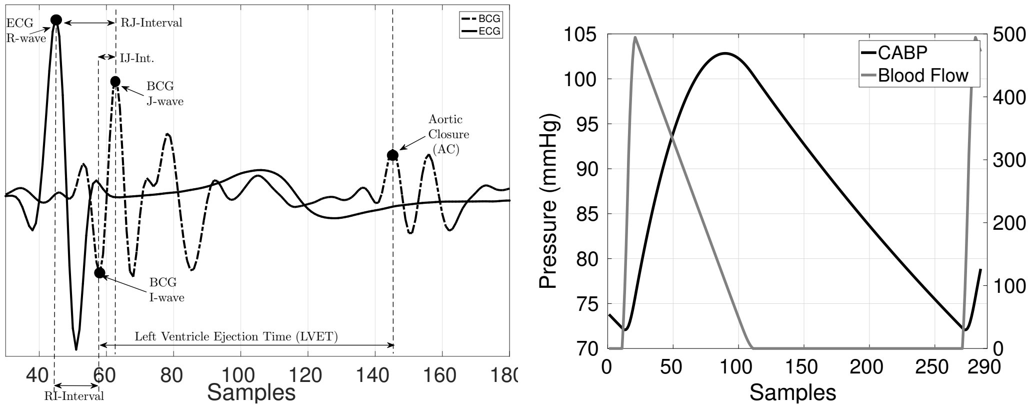

(a) Feature time extraction on averaged ECG and BCG heartbeats

(b) CABP and aortic Flow estimated by the PTTBM

Figure 8.11: Feature extraction over the averaged ECG and BCG signals measured in a volunteer. Hemodynamics estimated from the extracted feature times and the proposed pulse transit time based model (PTTBM).

(see Fig. 8.11b). This procedure was used for both; for tailoring the model constants k_c, k_{ej} and k_r from CABP and FTs; and, for estimating CABP from FTs. Noteworthy, the latter estimation added a further step since the model uses diastolic CABP ($P_0 = dCBP - Preload$) as an input parameter, being the diastolic CABP the output solution. This issue was resolved by iterating the output solution on the PTTBM, way back to the input, until the error on subsequent dCBP estimations was neglectable $(norm_2\,[\epsilon_{dCBP}] < 1\,mmHg)$

8.4 Results

8.4.1 Qualitative results

One of the main features of the proposed CABP estimation model is the dealing with the reported problem [42] of the eventual systolic and diastolic un-correlations (see Fig. 8.1) through minimal fluctuations on model parameters. For instance, Fig. 8.12 shows level-1 evaluations for the proposed estimation model when different hemodynamic maneuvers are carried out. Figure 8.12a shows a constant pulse pressure during the acquisition, and thus, diastolic and systolic CABP maintain a direct correlation. Then, during an acquisition by increasing the room temperature, systolic BP kept almost constant while diastolic CABP decreased slowly (Fig. 8.12b). Valsalva maneuver (Fig. 8.12c) showed an almost constant diastolic BP, while systolic BP abruptly increased at the third data-set. Finally, during the cold pressor maneuver (Fig. 8.12d), pulse pressure gently increased, and diastolic CABP fluctuated following an almost sine curve. The proposed CABP estimation model reasonably tracked different hemodynamic behaviors while parameter scattering remained within the 10 % from parameters tailored at baseline.

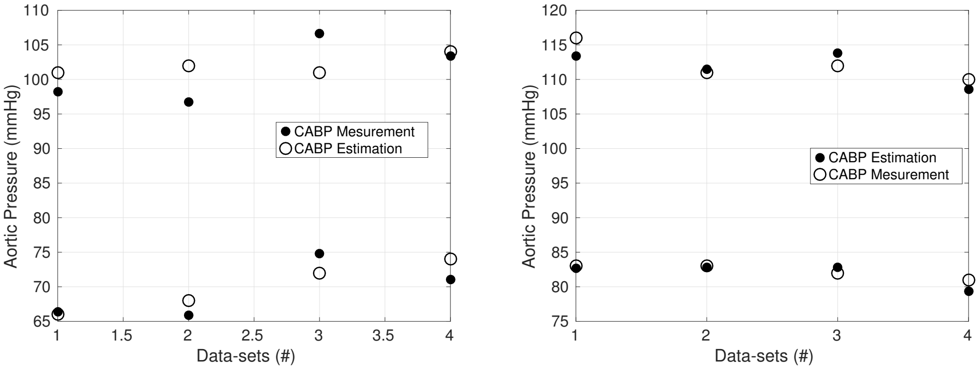

(a) Basal (b) Increasing Temperature

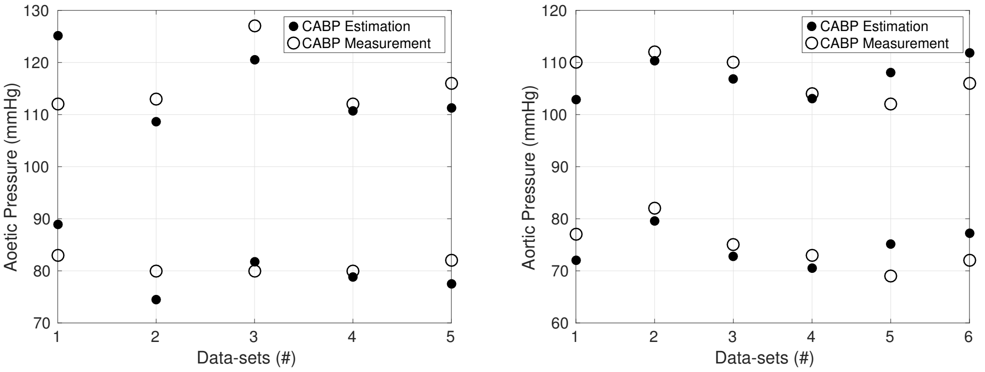

(c) Valsalva (d) Cold Pressor

Figure 8.12: Central aortic (systolic and diastolic) blood pressure fluctuations due to different types of acquisitions (baseline, Hot-room, Valsalva, cold pressor) experienced by a volunteer. White dots are the cuff-device CABP assessments whiles black dots are the wearable CABP estimation by using the PTTBM presented in this chapter.

8.4.2 Level-1 validation

The level-1 evaluation of the proposed method was assessed to study the spread of the tailored parameters across different groups of data-sets. Table 8.1 shows the parameters tailored along the eleven groups of data-sets presented in section 6.1, which were assessed during three days of observations over one subject, and, by involving hemodynamic maneuvers.

Table 8.2 summarizes the performance of the presented method considering the level-1 evaluation scheme; additionally, a previous evaluated BP estimation (linear on PEP^{-1}) was also included to contrast the performances. The figure of merit (FOMs) on the tables are: Correlation (r), slope (m), and intercept (y) from linear regression plots (Measurements vs. Estimation), and root-mean-square error (RMSE). Additionally, in order to show a compact measure for assessing to the parameter scattering, $\frac{\sigma}{\mu}(paramater)$ is used as the standard deviation of the parameter over the mean value of the parameter along the eleven trials, as was

Group of Data-sets	**kc**	**kej**	**kr**
1	0.83	1.00	1.00
2	0.87	1.00	0.99
3	0.91	0.97	0.97
4	0.83	0.97	0.96
5	0.85	0.99	0.99
6	0.87	1.01	1.01
7	0.88	0.98	0.97
8	0.90	1.05	1.05
9	0.82	1.02	1.02
10	0.74	1.03	1.03
11	0.64	1.10	1.11

Table 8.1: Parameters of the proposed model tailored along eleven groups of data-sets which were assessed during three days of observations, and, involved hemodynamic maneuvers (see sec. 6.1).

Mode	***Evaluation Level-1***				
FT	**RI-interval**		**Proposed**		
CABP	**S**	**D**	**S**	**D**	**Units**
r	0.88*	0.87*	0.99*	0.5*	-
m	0.78	0.75	0.76	0.75	-
y	25	19	25	19	mmHg
RMSE	2.2	2.4	8	7	mmHg
$\frac{\sigma}{\mu}(A_{X_{FT}})$	887	430	-		%
$\frac{\sigma}{\mu}(B_{X_{FT}})$	64	187	-		%
$\frac{\sigma}{\mu}(k_c)$	-		9.6		%
$\frac{\sigma}{\mu}(k_{ej})$	-		3.9		%
$\frac{\sigma}{\mu}(k_r)$	-		4.3		%

Table 8.2: Performance table on the estimation of Central Aortic Blood Pressure from the previously studied CABP estimation model (inverse-on-RI model) and the proposed in this chapter. Model constants are estimated through curve fitting routines using the discussed *Level-1* evaluation method (6.1.4)

introduced in chapter 6, where, if the method had absolute time stability over the three days, such introduced FOM would be zero. Fig. 8.13 shows the evolution of PTTBM parameters along different groups of data-sets for the PEP-based estimation model (table 8.13a) and the proposed in this chapter (table 8.13b). Scatter on parameters is written as a relative scatter (error) from the parameters resolved from the first group of data-sets; thus, defined scatter at GR_1 is zero.

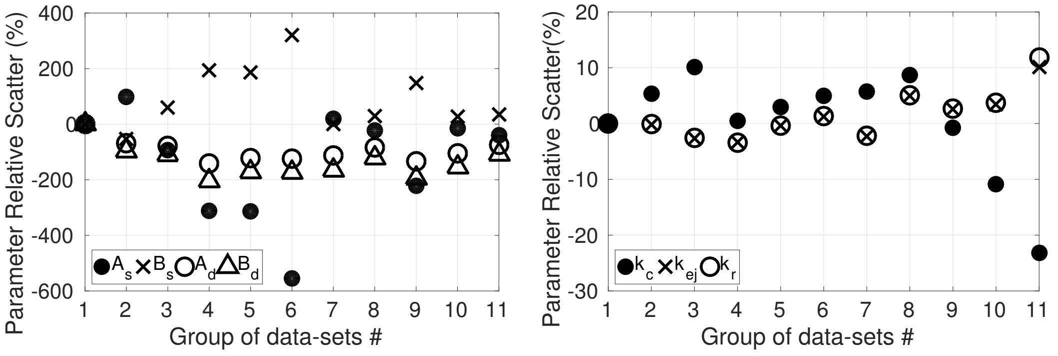

(a) CABP estimation from RI (b) CABP estimation from proposed PTTBM

Figure 8.13: Scattering of parameters of the used in CABP-PTTBM: evolution along groups of data-sets acquired during three days of intermittent assessment on one volunteer

8.5 Discussion

This chapter aims to present an original method to estimate CABP from ECG and BCG acquisitions. The main contribution of the presented CABP estimation method was the stability of the involved parameter across groups of data-sets since considered data-sets were acquired several days apart from each other. Scatter on k_c remained inside 20 % from initial calibration whilst scatter remained within the 10% for parameters k_{ej} and k_r. Furthermore, stability on tailored parameters occurred near the unity for all parameters ($k_c = 0.83 \pm 0.08$, $k_{ej} = 1.01 \pm 0.039$ and $k_r = 1.01 \pm 0.043$), which was their expected values from the theoretical considerations employed. This fact acknowledges the compliance of the methods coexisting in the conception of this idea; for example, the instrumentation section took care of the phase lags on acquired waveforms, which would lead to inaccuracies in the estimation of myocardial contraction.

Nevertheless, regarding the CABP estimation, the method suffers from inaccuracies, which currently induces an out of AAMI specification performance, specifically, when the variance of the estimation error variance is considered. CABP estimation inaccuracies were noted during the preparation of the methodology, mainly due to the intrinsic difficulty that the method involves. For instance, in order to mention few of them:

- Aortic closure (AC): given that AC estimation was provided from a parasitic coupling of SCG on the BCG signal, it was expected and noticed a poor quality of the AC event to be captured on the BCG signal. Additionally, since the AC event is relatively far away from the R-wave, it was noticed that in several cases, the average ensemble procedure (which in turn was needed for the BCG) smashed the wave used as AC event indicator. It was pretty easy to pick a wrong BCG-wave for the AC estimation in such cases, which leads directly to a CABP inaccuracy. Capturing an accurate AC timing reference means a quite challenging signal processing problem which exceeded the scope of this thesis.

- Systemic aortic resistance (R_a): Such a parameter represents the bottleneck of the method. As previously mentioned, R_a is the only hemodynamic parameter unavailable by any measurement performed by the designed hardware. In some cases 8.30 might provide a reasonable estimation of R_a, specially when baroreflex loop controls R_a, but in many others, 8.30 might be not enough, for example if R_a is settled chemically [8] or fluctuates due the temperature.

- Bias quantities: Several unavailable CV quantities were used to estimate the elements of the model; mainly, peak blood flow estimation required several of such quantities. The approach used typical CV magnitudes (table 8.3) in order to provide a biasing point for the element to be estimated from the available quantities (PEP in this case). Nevertheless, it is widely acknowledged that such biasing parameters fluctuate on a beat-to-beat basis, which results in an unpredictable CABP fluctuation.

- Compliance estimation: PTT estimation from the BCG signal was based on reported evidence signaling that aortic PTT could be assessed by measuring head-to-foot acceleration recoils due to aortic blood flow [52]. Nevertheless, SCG coupling on the BCG signal might corrupt the PTT acquisition, which, once again, leads directly to inaccuracies on CABP estimations. Accordingly, k_c was the parameter that suffered the most substantial scattering across data-sets.

The presence of errors on the CABP estimation was responsible for the poor RMSE ($\approx 7-8\ mmHg$) achieved, where some of them showed inaccuracies in the order of 20 mmHg. Nevertheless, a near to zero mean of the estimation requirement was achieved by the method; further work should be center in reducing the variance of the error. Finally, despite the presence of such energy for the estimation error, the curve fitting routines lead to stable tailored parameters along the time. This might mean the conception of a novel method to estimate CABP, which features a robust convergence of its parameters.

8.6 Conclusions

This chapter aims to present novel ideas to estimate CABP, which is promising to resolve the (previously reported) parameter-stability problem (Chapter 6), that is, the significant scattering observed on PTTBM parameter along different calibrations, which may affect the classic PTT-based method. Nevertheless, the proposed methodology suffers from inaccuracies that prevent it from estimating CABP accurately and continuously in the meantime. Some of the accuracy issues were identified and reported, and its mitigation is part of future work. The method is entirely based on CV physiological modeling, and results showed a robust convergence of the involved parameters, even carrying inaccuracies on the CABP estimation, and proposed parameters besides presenting robust, and stable convergence, they were compliant with the proposed physiological considerations.

8.7 Typical cardiovascular magnitudes

Table 8.3: Typical cardiovascular magnitudes expressed according to their type group (Type), full name (Magnitude), abbreviation used in the text (Abb) and, minimum (Min), typical (Typ), and maximum (Max) reference values, with their respective units (Units). There is also a column with the corresponding references indicating where each magnitude was from (Ref).

Type	**Magnitude**	**Abb**	**Min**	**Typ**	**Max**	**Units**	**Ref**
Cardiac Timing	Heart Rate	HR		60	220	bpm	[8]
	Pre-Ejection Period	PEP		50		ms	
	Left Ventricular Ejection	LVET		300		ms	
	Pulse transit [root–arch]	PTT		20		ms	
Velocities	pulse wave velocity			6.5		m/s	
Areas	Aortic Valve	AVA	0.7	3	4	cm^2	[117]
	Aortic Root	Ai		6.8		cm^2	[52]
	Aortic Arch	Aa		5.07		cm^2	[52]
	Thoracic Aorta	At		3.94		cm^2	[52]
	Abdominal Aorta	Ab		1.25		cm^2	[52]
	Capillary cross-sect.	Acap		1000		cm^2	[8]
	Vena cava cross-sect.	Acav		7		cm^2	[8]
Distance	Aortic: root-arch	L		12		cm	[52]
Pressures	Central BP systolic	sCBP		115		mmHg	
	Central BP diastolic	dCBP		70		mmHg	
	Preload	P_{reload}		12.5		mmHg	&
Volumes	Stroke volume			75	120	cm^3	[8]
	LV Volume @ ED	EDV		125		cm^3	
	LV Volume @ ES	ESV		50			
	Unstressed vol.	V_{uns}		20		cm^3	[114]
Blood Properties	Blood Density	ρ		1060		kg/m^3	
	Blood Viscosity			2.76		mPa s	
Resistances	Aortic Valve	AVR	38m	45m	0.225	mmHg s /cm^3	[117]
	Systemic vascular	R		1.2		mmHg s/ cm^3	[8]
Compliances	Aortic (cross-sect.)	C_{as}		0.018		cm^2/mmHg	8.26
	Aortic	C_a		1.82		cm^3/mmHg	PP/SV
Elastance	LV end-diastolic PVR	EDPVR		0.1			P_{reload}/EDV
	LV end-systolic PVR	ESPVR		3.46			P_0/ESV
	Aortic (cross-sect.)	Eas		56.6		mmHg/cm^2	C_{as}^{-1}
	Aortic	Ea		0.55		mmHg /cm^3	C_a^{-1}

Chapter 9

Conclusions

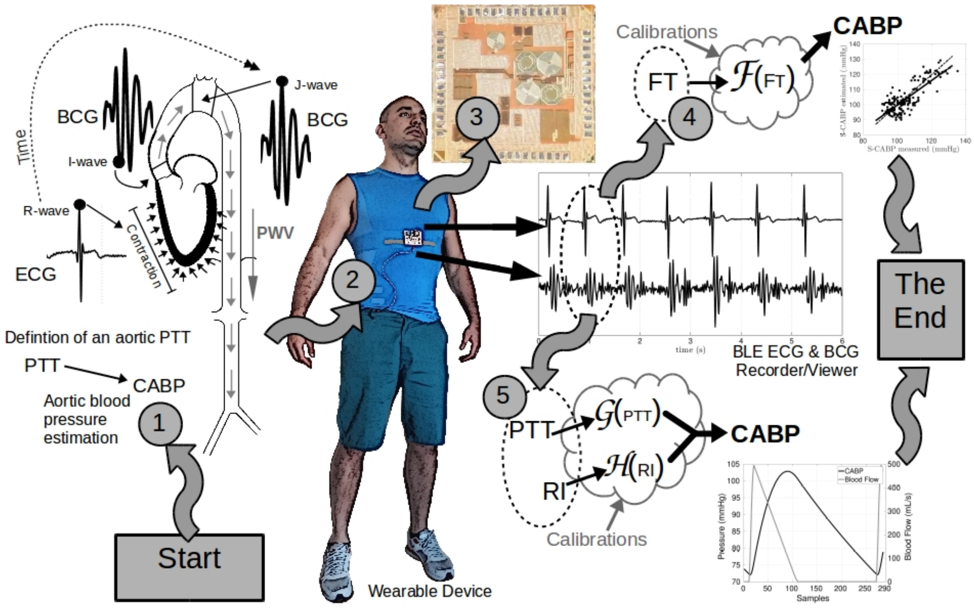

Figure 9.1: Conceptual map of the presented thesis divided in zones. Zone-1: Foundations of the proposed method for the wearable estimation of aortic blood pressure (CABP). Zone-2: Conception of a wearable device for electrocardiogram (ECG) and ballistocardiogram (BCG) recording and visualization. Zone-3: Integration of the proposed method for the analog conditioning of ECG and BCG signals. Zone-4: Validations on the wearable CABP estimation by using available in-the-literature estimation models (PTTBM). Zone-5: Proposition of a novel PTTBM for estimating CABP that exploits the information extracted from the proposed wearable device.

Conception of working zones

Figure 9.1 shows the conceptual map of the presented thesis in-which the investigation was divided in working-zones.

- *Zone-1:* Started by seeking a method for the wearable blood pressure estimation and the pulse transit time (PTT) method aroused as one of the most prominent due to the cuff-less and continuous characteristics. Since the method foundations indicate that it is mainly exploitable at elastic arteries, it was procured the nearby of the aortic root as the vascular zone for developing a proposed approach for estimating BP based on PTT-method. An aortic PTT could be estimated from electrocardiogram (ECG) and ballistocardiogram (BCG) signals, which accordingly is used for estimating aortic blood pressure (CABP).
- *Zone-2:* Denotes the instrumentation section of the presented thesis and the design of the wearable device used for monitoring and recording ECG and BCG waveforms wirelessly. The design features a novel approach for conditioning the physiological signals suitable for the PTT assessment.
- *Zone-3:* Migration of the wearable device into the integrated circuit (IC) technology. Ultra-low-power IC implementation of the core block for the analog filtering of the ECG and BCG signals.
- Zone-4: Chapters 6 and 7 are grouped up in this zone that showed the validations on the wearable CABP estimation. BP estimation models (PTTBM) available in the literature were used for constructing CABP variables from feature times (FT) extracted from wearable signals.
- Zone-5: A PTTBM for estimating CABP is proposed at the end of the thesis. Such development provides this thesis with an entirely original path from the ECG and the BCG acquisition up to the CABP estimation.

Conclusions and contribution throughout working zones

Working Zone-1

The first main contribution of this thesis was the reaffirmation of the PTT-method to be used for estimating CABP by proposing a methodology based on the assessment of an aortic PTT. Investigation on chapter 3 showed that continuous CABP estimation might be feasible through the proposed ECG-BCG-based PTT. Even though the conception of the PTT was refining throughout the thesis, chapter 3 foundations remained until the end of the document. State-of-the-art results support that an aortic PTT can be estimated by measuring longitudinal (head-to-foot) body accelerations as timing references, and, the work proposed such PTT for collating against central BP, rather than peripheral BP (PBP) as typically found in the literature. In effect, chapter 3 results showed that a better association with CABP (regarding PBP) could be achieved by the method; which in turn, is consistent with the PTT theory since it is developed mainly for elastic arteries, and also, both, PTT and CABP are referred to the same aortic district. Additionally, it is convenient since CABP might be a better variable for assessing cardiovascular health. That is, it has been reported that CABP might offer an incremental prediction capability of cardiovascular risk over peripheral BP.

Working Zone-2

The development of an adequate acquisition methodology for the PTT computation meant another significant contribution of the thesis. Before the conception of the ideas to threaten the phase lags on PTT acquisition, it was noticed that different amounts of PTT were reported from different research groups (even when the same arterial path to compute PTT was considered). It was understood that there was a need for improvement in this sense for the PTT computation. Original hardware and software methodologies were developed to minimize the phase lag problem, and further, the proposed solution can be exploited by other developers for the PTT acquisition no matter the nature of the PTT considered. On the analog side, the proposed approach aims to exploit the under-damped filtering in order to maximize the region with a small phase shift over the narrow filter bandwidth; whereas, on the digital side, a low-order (N=16) finite impulse response filter design was proposed. Simulations and measurements show that a negligible spurious timing error of less than 2 ms can be achieved. Furthermore, a wearable device was conceived on the frame of this thesis; such design implied the integration of the proposed analog hardware with the Bluetooth technology in a compact device to be attached to a training shirt to provide unnoticed monitoring. Measurements on the wearable device showed the effectiveness of the proposed methodology on a real application.

Working Zone-3

Another significant contribution of this thesis remained on the miniaturization of the hardware section of the proposed PTT-acquisition methodology. Notably, the fabricated design aims to provide a highly miniaturized solution for the low-delay narrow-band ECG and BCG conditioning, as presented in chapter 4 (working Zone-2) for the proper PTT acquisition. Material presented was centralized on presenting a proposed second-order filter that produces the required (under-damped) bandwidth limitation characteristic. Such an approach might be challenging to implement with IC technologies due to the process variability, the large time-constant required for filtering, and the ultra-low-power (ULP) characteristic required for autonomy. The design of the proposed filter required efficient solutions for the on-chip generation of pico-ampered currents, voltage dividers, and tuning methodologies for setting correctly the filtering parameters, which were shown as corollary contributions of the thesis.

Working Zone-4

This work zone studied the interactions between the different state-of-the-art physiological modeling and proposed hardware/method. In this context, it was shown that results achieved with off-the-shelf equipment could be replicated by using the proposed wearable device. Additionally, experimentally explored twenty-seven alternatives, nine PTTBM along three FT (intervals, R-I, R-J, and I-J), for the CABP estimation from the proposed wearable ECG-BCG-based methodology. Data were evaluated from ten volunteers during three different hemodynamic interventions. We found that aortic BP could be accurately estimated through the presented methodology by using four of the explored alternatives, whereas the R-I interval emerged as the best surrogate for the aortic BP estimation. Furthermore, a principle different from the traditional PTT-based method arose as a more advantageous method for central aortic BP assessment in the light of evidence reported in this work zone, and, to our knowledge, this is the first time that CABP has been successfully estimated from a wearable device.

Working Zone-5

The final significant contribution of this thesis meant the last chain-link in the process to come by an utterly original method to estimate CABP. A novel PTTBM to estimate CABP was proposed by using a current-driven two-element Windkesel network constructed from features extracted of the proposed hardware. The initial validations of the PTTBM were presented, showing that it is promising to resolve some issues observed during the CABP estimation when classic PTTBMs were used (physiological disconnection at calibration stages, parameter-instability across calibrated PTTBMs). The proposed methodology still suffers from inaccuracies that prevent it from estimating CABP in the meantime, but despite the inaccuracies, the method could be exploited to screen hypertension in the short-term. Some of the accuracy issues were identified and reported, and its mitigation is part of future work. The method is entirely based on cardiovascular physiological modeling, and results showed a robust convergence of the defined parameters.

Appendix A

- Proposed PTT-Based model in CADENCE

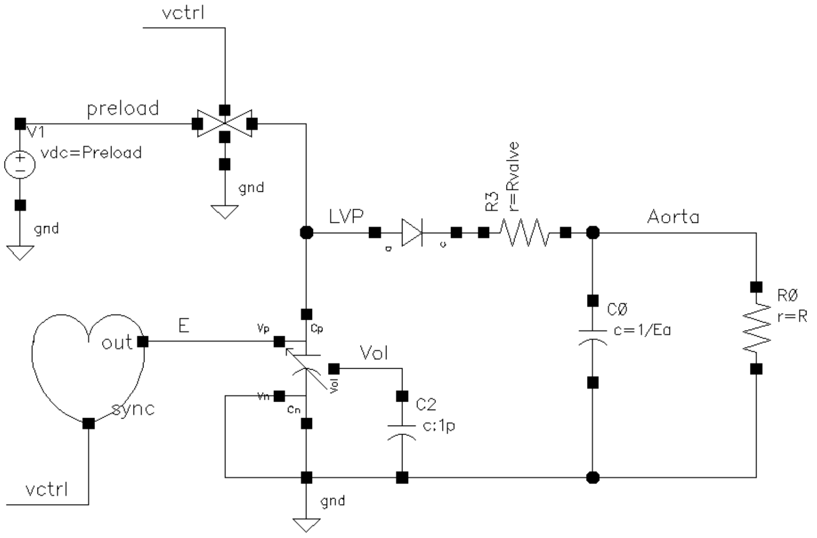

Figure A.1: Adaptation of the proposed PTT-based model to run in CADENCE EDA simulator

Figure A.1 shows the schematic constructed in the CADENCE EDA tool environment to perform transient simulations on the proposed CABP estimation model based on a current driven two-element Windkessel network. Left ventricle is modeled by a voltage controlled capacitor (VCCap) element where; $V_p - V_n$ is the input voltage that controls the capacitance seen between nodes $C_p - C_n$. The Left Ventricle Volume can be assessed in node Vol. The changes of VCCap capacitance (or elastance ($E(t)$)) are driven by the heart-shaped-block, which acts as voltage waveform source where elastance is read as a voltage in node *out*. The block also provides the synchronization signal to fill the LV when relaxed. Such blocks, along with ideal switch and diode, were programmed in velilogA language, as shown in Fig. A.2. Analoglib provided the resistances and capacitance to model Aortic valve resistance (R_{valve}), total systemic vascular resistance seen from aorta (R_0), and aortic compliance (C_0, $c = 1/E_a$, E_a: Aortic Elastance).

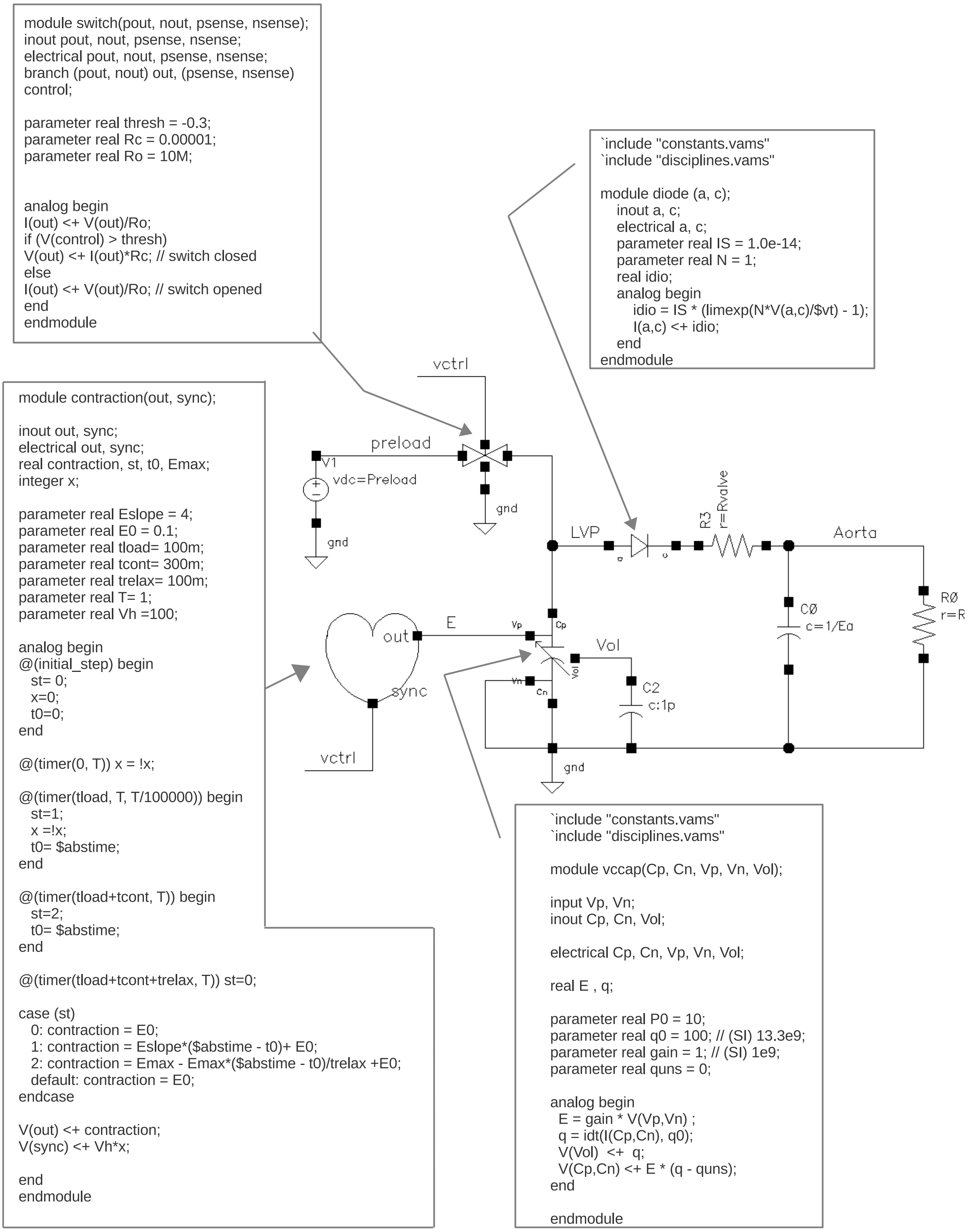

```
module switch(pout, nout, psense, nsense);
inout pout, nout, psense, nsense;
electrical pout, nout, psense, nsense;
branch (pout, nout) out, (psense, nsense)
control;

parameter real thresh = -0.3;
parameter real Rc = 0.00001;
parameter real Ro = 10M;


analog begin
I(out) <+ V(out)/Ro;
if (V(control) > thresh)
V(out) <+ I(out)*Rc; // switch closed
else
I(out) <+ V(out)/Ro; // switch opened
end
endmodule
```

```
`include "constants.vams"
`include "disciplines.vams"

module diode (a, c);
   inout a, c;
   electrical a, c;
   parameter real IS = 1.0e-14;
   parameter real N = 1;
   real idio;
   analog begin
      idio = IS * (limexp(N*V(a,c)/$vt) - 1);
      I(a,c) <+ idio;
   end
endmodule
```

```
module contraction(out, sync);

inout out, sync;
electrical out, sync;
real contraction, st, t0, Emax;
integer x;

parameter real Eslope = 4;
parameter real E0 = 0.1;
parameter real tload= 100m;
parameter real tcont= 300m;
parameter real trelax= 100m;
parameter real T= 1;
parameter real Vh =100;

analog begin
@(initial_step) begin
   st= 0;
   x=0;
   t0=0;
end

@(timer(0, T)) x = !x;

@(timer(tload, T, T/100000)) begin
   st=1;
   x =!x;
   t0= $abstime;
end

@(timer(tload+tcont, T)) begin
   st=2;
   t0= $abstime;
end

@(timer(tload+tcont+trelax, T)) st=0;

case (st)
   0: contraction = E0;
   1: contraction = Eslope*($abstime - t0)+ E0;
   2: contraction = Emax - Emax*($abstime - t0)/trelax +E0;
   default: contraction = E0;
endcase

V(out) <+ contraction;
V(sync) <+ Vh*x;

end
endmodule
```

```
`include "constants.vams"
`include "disciplines.vams"

module vccap(Cp, Cn, Vp, Vn, Vol);

input Vp, Vn;
inout Cp, Cn, Vol;

electrical Cp, Cn, Vp, Vn, Vol;

real E , q;

parameter real P0 = 10;
parameter real q0 = 100; // (SI) 13.3e9;
parameter real gain = 1; // (SI) 1e9;
parameter real quns = 0;

analog begin
  E = gain * V(Vp,Vn) ;
  q = idt(I(Cp,Cn), q0);
  V(Vol)  <+  q;
  V(Cp,Cn) <+ E * (q - quns);
end

endmodule
```

Figure A.2: Proposed PTT-based model in CADENCE simulator with VerilogA modules

Bibliography

[1] Katherine T Mills, Joshua D Bundy, Tanika N Kelly, Jennifer E Reed, Patricia M Kearney, Kristi Reynolds, Jing Chen, and Jiang He. Abstract 32: Global burden and control of hypertension in 2010: Analysis of population-based studies from 89 countries. *Circulation*, 131(suppl_1):A32–A32, 2015.

[2] Christodoulos Stefanadis, Katerina Baou, Konstantinos Aznaouridis, Charalambos Vlachopoulos, Michael F. O'Rourke, and Michel E. Safar. Prediction of cardiovascular events and all-cause mortality with central haemodynamics: a systematic review and meta-analysis. *European Heart Journal*, 31(15):1865–1871, 03 2010.

[3] J. E. Sharman and S. Laurent. Central blood pressure in the management of hypertension: soon reaching the goal? *Journal Of Human Hypertension*, 27:405 EP –, Mar 2013. Review.

[4] Riccardo Pini, M. Chiara Cavallini, Vittorio Palmieri, Niccolò Marchionni, Mauro Di Bari, Richard B. Devereux, Giulio Masotti, and Mary J. Roman. Central but not brachial blood pressure predicts cardiovascular events in an unselected geriatric population. *Journal of the American College of Cardiology*, 51(25):2432–2439, 2008.

[5] Ramakrishna Mukkamala and Jin-Oh Hahn. Toward ubiquitous blood pressure monitoring via pulse transit time: Predictions on maximum calibration period and acceptable error limits. *IEEE Transactions on Biomedical Engineering*, 65(6):1410–1420, 2017.

[6] Charalambos Vlachopoulos, Michael O'Rourke, and Wilmer W Nichols. *McDonald's blood flow in arteries: theoretical, experimental and clinical principles*. CRC press, 2011.

[7] Yanina Zócalo and Daniel Bia. Presión aórtica central y parámetros clínicos derivados de la onda del pulso: evaluación no invasiva en la práctica clínica importancia clínica y análisis de las bases metodológicas de los equipos disponibles para su evaluación. *Revista Uruguaya de Cardiología*, 29(2):215–230, 2014.

[8] Josep Maria Solà i Carlós. *Continuous non-invasive blood pressure estimation*. PhD thesis, ETH Zurich, 2011.

[9] Nicolaas Westerhof, Nikolaos Stergiopulos, and Mark IM Noble. *Snapshots of hemodynamics: an aid for clinical research and graduate education.* Springer Science & Business Media, 2010.

[10] B. Koeppen B. Stanton. *Berne and Levy physiology.* ELSEVIER, 2018.

[11] Ricardo Armentano and Luis Kun. Multidisciplinary, holistic and patient specific approach to follow up elderly adults. *Health and Technology*, 4(2):95–100, 2014.

[12] Alessandra Corradetti. Ambulatory blood pressure monitoring in pregnancy. 2011.

[13] J. M. Roberts, G. Pearson, J. Cutler, and M. Lindheimer. Summary of the nhlbi working group on research on hypertension during pregnancy. 2003.

[14] Khalid S Khan, Daniel Wojdyla, Lale Say, A Metin Gülmezoglu, and Paul FA Van Look. Who analysis of causes of maternal death: a systematic review. *The lancet*, 367(9516):1066–1074, 2006.

[15] Jason Waugh, Paul Bosio, Marwan Habiba, Trudy Boyce, Andrew Shennan, and Aidan Halligan. Home monitoring of blood pressure in pregnancy at high risk of pre-eclampsia. *European Journal of Obstetrics & Gynecology and Reproductive Biology*, 99(1):109–111, 2001.

[16] Gianni Bellomo, Pier Luca Narducci, Francesco Rondoni, Giovanni Pastorelli, Gabriela Stangoni, Giulio Angeli, and Paolo Verdecchia. Prognostic value of 24-hour blood pressure in pregnancy. *Obstetrical & Gynecological Survey*, 55(4):196–198, 2000.

[17] X. Ding, N. Zhao, G. Yang, R. I. Pettigrew, B. Lo, F. Miao, Y. Li, J. Liu, and Y. Zhang. Continuous blood pressure measurement from invasive to unobtrusive: Celebration of 200th birth anniversary of Carl Ludwig. *IEEE Journal of Biomedical and Health Informatics*, 20(6):1455–1465, Nov 2016.

[18] Simon M Thom, Kennedy Cruickshank, Alice Stanton, David Collier, Alun D Hughes, and H Thurston. Differential impact of blood pressure–lowering drugs on central aortic pressure and clinical outcomes. *Circulation*, 113:1213–1225, 2006.

[19] Paolo Salvi, Giuseppe Lio, Carlos Labat, Enrico Ricci, Bruno Pannier, and Athanase Benetos. Validation of a new non-invasive portable tonometer for determining arterial pressure wave and pulse wave velocity: the pulsepen device. *Journal of hypertension*, 22(12):2285–2293, 2004.

[20] Motoaki Sugawara, Kiyomi Niki, Nobuyuki Ohte, Takashi Okada, and Akimitsu Harada. Clinical usefulness of wave intensity analysis. *Medical & Biological Engineering & Computing*, 47(2):197–206, Feb 2009.

[21] M. Butlin, A. Qasem, and A. P. Avolio. Estimation of central aortic pressure waveform features derived from the brachial cuff volume displacement waveform. In *2012 Annual International Conference of the IEEE Engineering in Medicine and Biology Society*, pages 2591–2594, Aug 2012.

[22] Thomas Weber, Siegfried Wassertheurer, Martin Rammer, Edwin Maurer, Bernhard Hametner, Christopher C. Mayer, Johannes Kropf, and Bernd Eber. Validation of a brachial cuff-based method for estimating central systolic blood pressure. *Hypertension*, 58(5):825–832, 2011.

[23] Zahra Ghasemi, Jong Chan Lee, Chang-Sei Kim, Hao-Min Cheng, Shih-Hsien Sung, Chen-Huan Chen, Ramakrishna Mukkamala, and Jin-Oh Hahn. Estimation of cardiovascular risk predictors from non-invasively measured diametric pulse volume waveforms via multiple measurement information fusion. *Scientific reports*, 8(1):10433, 2018.

[24] Keerthana Natarajan, Hao-Min Cheng, Jiankun Liu, Mingwu Gao, Shih-Hsien Sung, Chen-Huan Chen, Jin-Oh Hahn, and Ramakrishna Mukkamala. Central blood pressure monitoring via a standard automatic arm cuff. *Scientific reports*, 7(1):14441, 2017.

[25] Chloe M Park, Olga Korolkova, Justin E Davies, Kim H Parker, Jennifer H Siggers, Katherine March, Therese Tillin, Nish Chaturvedi, and Alun D Hughes. Arterial pressure: agreement between a brachial cuff-based device and radial tonometry. *Journal of hypertension*, 32(4):865, 2014.

[26] James E Sharman, Richard Lim, Ahmad M Qasem, Jeff S Coombes, Malcolm I Burgess, Jeff Franco, Paul Garrahy, Ian B Wilkinson, and Thomas H Marwick. Validation of a generalized transfer function to noninvasively derive central blood pressure during exercise. *Hypertension*, 47(6):1203–1208, 2006.

[27] David J. Holland, Julian W. Sacre, Sarah J. McFarlane, Jeffrey S. Coombes, and James E. Sharman. Pulse Wave Analysis Is a Reproducible Technique for Measuring Central Blood Pressure During Hemodynamic Perturbations Induced by Exercise. *American Journal of Hypertension*, 21(10):1100–1106, 10 2008.

[28] AtCor Medical SphygmoCor XCELL web site. `http://atcormedical.com/healthcare-professionals/products/`. Accessed: 2019-03-14.

[29] Francisco Morales-Acuna, Brycen Ratcliffe, Caleb Harrison, Sierra Crowe, Evan Bockover, Robert Pawlak, and Alvaro N. Gurovich. Comparison between cuff-based and radial tonometry exercise-induced central blood pressure. *European Journal of Applied Physiology*, 119(4):901–911, Apr 2019.

[30] M.-H. Hwang, J.-K. Yoo, H.-K. Kim, C.-L. Hwang, K. Mackay, O. Hemstreet, W. W. Nichols, and D. D. Christou. Validity and reliability of aortic pulse wave velocity and augmentation index determined by the new cuff-based

sphygmocor xcel. *Journal Of Human Hypertension*, 28:475 EP –, Jan 2014. Original Article.

[31] Weijie Lim, James Faulkner, Danielle Lambrick, and Lee Stoner. Reliability of oscillometric central blood pressure responses to submaximal exercise. *Journal of hypertension*, 34(6):1084–1090, 2016.

[32] James E. Sharman, Martin G. Schultz, Xiaoqing Peng, Walter P. Abhayaratna, and Michael Stowasser. Comparison of Central Blood Pressure Estimated by a Cuff-Based Device With Radial Tonometry. *American Journal of Hypertension*, 29(10):1173–1178, 06 2016.

[33] Atcor medical - sphigmocor xcel. `https://atcormedical.com/products/sphygmocor-xcel/`.

[34] Josep Sola, Martin Proenca, and Olivier Chetelat. Wearable PWV technologies to measure blood pressure: eliminating brachial cuffs. In *Engineering in Medicine and Biology Society (EMBC), 2013 35th Annual International Conference of the IEEE*, pages 4098–4101. IEEE, 2013.

[35] Y. Zheng, B. P. Yan, Y. Zhang, C. M. Yu, and C. C. Y. Poon. Wearable cuff-less ptt-based system for overnight blood pressure monitoring. In *2013 35th Annual International Conference of the IEEE Engineering in Medicine and Biology Society (EMBC)*, pages 6103–6106, July 2013.

[36] E. S. Winokur, D. D. He, and C. G. Sodini. A wearable vital signs monitor at the ear for continuous heart rate and pulse transit time measurements. In *2012 Annual International Conference of the IEEE Engineering in Medicine and Biology Society*, pages 2724–2727, Aug 2012.

[37] G.J. Langewouters, K.H. Wesseling, and W.J.A. Goedhard. The static elastic properties of 45 human thoracic and 20 abdominal aortas in vitro and the parameters of a new model. *Journal of Biomechanics*, 17(6):425 – 435, 1984.

[38] D.J. Hughes, C.F. Babbs, L.A. Geddes, and J.D. Bourland. Measurements of young's modulus of elasticity of the canine aorta with ultrasound. *Ultrasonic Imaging*, 1(4):356 – 367, 1979.

[39] R. Mukkamala, J. Hahn, O. T. Inan, L. K. Mestha, C. Kim, H. Töreyin, and S. Kyal. Toward ubiquitous blood pressure monitoring via pulse transit time: Theory and practice. *IEEE Transactions on Biomedical Engineering*, 62(8):1879–1901, Aug 2015.

[40] Christer Ahlstrom, Anders Johansson, Fredrik Uhlin, Toste Länne, and Per Ask. Noninvasive investigation of blood pressure changes using the pulse wave transit time: a novel approach in the monitoring of hemodialysis patients. *Journal of Artificial Organs*, 8(3):192–197, 2005.

[41] Heiko Gesche, Detlef Grosskurth, Gert Küchler, and Andreas Patzak. Continuous blood pressure measurement by using the pulse transit time: comparison to a cuff-based method. *European Journal of Applied Physiology*, 112(1):309–315, 2012.

[42] Peyman Yousefian, Sungtae Shin, Azin Mousavi, Chang-Sei Kim, Ramakrishna Mukkamala, Dae-Geun Jang, Byung-Hoon Ko, Jongwook Lee, Ui Kun Kwon, Youn Ho Kim, et al. Data mining investigation of the association between a limb ballistocardiogram and blood pressure. *Physiological measurement*, 39(7):075009, 2018.

[43] R. A. Payne, C. N. Symeonides, D. J. Webb, and S. R. J. Maxwell. Pulse transit time measured from the ecg: an unreliable marker of beat-to-beat blood pressure. *Journal of Applied Physiology*, 100(1):136–141, 2006. PMID: 16141378.

[44] Non-invasive sphygmomanometers—part 2: Clinical validation of automated manometer type, iso 81060-2:2009, 2009.

[45] H. Lin, W. Xu, N. Guan, D. Ji, Y. Wei, and W. Yi. Noninvasive and continuous blood pressure monitoring using wearable body sensor networks. *IEEE Intelligent Systems*, 30(6):38–48, Nov 2015.

[46] Samyeul Noh, Chiyul Yoon, E Hyun, Hee Nam Yoon, TJ Chung, KS Park, and HC Kim. Ferroelectret film-based patch-type sensor for continuous blood pressure monitoring. *Electronics Letters*, 50(3):143–144, 2014.

[47] D. D. He, E. S. Winokur, T. Heldt, and C. G. Sodini. The ear as a location for wearable vital signs monitoring. In *2010 Annual International Conference of the IEEE Engineering in Medicine and Biology*, pages 6389–6392, Aug 2010.

[48] William R Scarborough, Samuel A Talbot, John R Braunstein, Maurice B Rappaport, William Dock, Wf Hamilton, John E Smith, John L Nickerson, and Isaac Starr. Proposals for ballistocardiographic nomenclature and conventions: revised and extended report of committee on ballistocardiographic terminology. *Circulation*, 14(3):435–450, 1956.

[49] Vincent de Lalla, Marvin A. Epstein, and Herbert R. Brown. Analysis of h wave of ballistocardiogram. *Circulation*, 2(5):765–769, 1950.

[50] Eduardo Pinheiro, Octavian Postolache, and Pedro Girão. Theory and developments in an unobtrusive cardiovascular system representation: ballistocardiography. *The open biomedical engineering journal*, 4:201, 2010.

[51] David Da He, Eric S Winokur, and Charles G Sodini. An ear-worn vital signs monitor. *Biomedical Engineering, IEEE Transactions on*, 62(11):2547–2552, 2015.

[52] Chang-Sei Kim, Stephanie L Ober, M Sean McMurtry, Barry A Finegan, Omer T Inan, Ramakrishna Mukkamala, and Jin-Oh Hahn. Ballistocardiogram: Mechanism and potential for unobtrusive cardiovascular health monitoring. *Scientific reports*, 6:31297, 2016.

[53] C. C. Y. Poon and Y. T. Zhang. Cuff-less and noninvasive measurements of arterial blood pressure by pulse transit time. In *2005 IEEE Engineering in Medicine and Biology 27th Annual Conference*, pages 5877–5880, Jan 2005.

[54] Yang Wang, Zhiwen Liu, and Shaodong Ma. Cuff-less blood pressure measurement from dual-channel photoplethysmographic signals via peripheral pulse transit time with singular spectrum analysis. *Physiological Measurement*, 39(2):025010, feb 2018.

[55] Z. Tang, T. Tamura, M. Sekine, M. Huang, W. Chen, M. Yoshida, K. Sakatani, H. Kobayashi, and S. Kanaya. A chair–based unobtrusive cuffless blood pressure monitoring system based on pulse arrival time. *IEEE Journal of Biomedical and Health Informatics*, 21(5):1194–1205, Sep. 2017.

[56] Jae Hyuk Shin, Kang Moo Lee, and Kwang Suk Park. Non-constrained monitoring of systolic blood pressure on a weighing scale. *Physiological Measurement*, 30(7):679–693, jun 2009.

[57] P. M. Nabeel, J. Joseph, and M. Sivaprakasam. Magnetic plethysmograph transducers for local blood pulse wave velocity measurement. In *2014 36th Annual International Conference of the IEEE Engineering in Medicine and Biology Society*, pages 1953–1956, Aug 2014.

[58] N. P M, J. Joseph, and M. Sivaprakasam. A magnetic plethysmograph probe for local pulse wave velocity measurement. *IEEE Transactions on Biomedical Circuits and Systems*, 11(5):1065–1076, Oct 2017.

[59] J. Muehlsteff, X. L. Aubert, and M. Schuett. Cuffless estimation of systolic blood pressure for short effort bicycle tests: The prominent role of the pre-ejection period. In *2006 International Conference of the IEEE Engineering in Medicine and Biology Society*, pages 5088–5092, Aug 2006.

[60] Mico Yee Man Wong, Emma Pickwell-MacPherson, Yuan Ting Zhang, and Jack CY Cheng. The effects of pre-ejection period on post-exercise systolic blood pressure estimation using the pulse arrival time technique. *European journal of applied physiology*, 111(1):135–144, 2011.

[61] Stephanie L-O Martin, Andrew M Carek, Chang-Sei Kim, Hazar Ashouri, Omer T Inan, Jin-Oh Hahn, and Ramakrishna Mukkamala. Weighing scale-based pulse transit time is a superior marker of blood pressure than conventional pulse arrival time. *Scientific reports*, 6:39273, 2016.

[62] Hazar Ashouri, Lara Orlandic, and Omer T. Inan. Unobtrusive estimation of cardiac contractility and stroke volume changes using ballistocardiogram measurements on a high bandwidth force plate. *Sensors*, 16(6), 2016.

[63] A. O. Bicen, N. Z. Gurel, A. Dorier, and O. T. Inan. Improved pre-ejection period estimation from ballistocardiogram and electrocardiogram signals by fusing multiple timing interval features. *IEEE Sensors Journal*, 17(13):4172–4180, July 2017.

[64] J. Solà, M. Proença, D. Ferrario, J. Porchet, A. Falhi, O. Grossenbacher, Y. Allemann, S. F. Rimoldi, and C. Sartori. Noninvasive and nonocclusive blood pressure estimation via a chest sensor. *IEEE Transactions on Biomedical Engineering*, 60(12):3505–3513, Dec 2013.

[65] Josep Solà, Andy Adler, Arnoldo Santos, Gerardo Tusman, Fernando Suárez Sipmann, and Stephan H Bohm. Non-invasive monitoring of central blood pressure by electrical impedance tomography: first experimental evidence. *Medical & biological engineering & computing*, 49(4):409, 2011.

[66] S. Puke, T. Suzuki, K. Nakayama, H. Tanaka, and S. Minami. Blood pressure estimation from pulse wave velocity measured on the chest. In *2013 35th Annual International Conference of the IEEE Engineering in Medicine and Biology Society (EMBC)*, pages 6107–6110, July 2013.

[67] Parry Fung, G. Dumont, C. Ries, C. Mott, and M. Ansermino. Continuous noninvasive blood pressure measurement by pulse transit time. In *The 26th Annual International Conference of the IEEE Engineering in Medicine and Biology Society*, volume 1, pages 738–741, Sept 2004.

[68] H. Gholamhosseini, J. Biswas, H. Zhang, M. Jayachandran, and M. M. Baig. Cuff-less, non-invasive and continuous blood pressure monitoring using indirect methods. In *Industrial Electronics and Applications (ICIEA), 2015 IEEE 10th Conference on*, pages 233–237, June 2015.

[69] Germán Fierro, Fernando Silveira, and Ricardo Armentano. Central blood pressure monitoring method oriented to wearable devices. *Health and Technology*, 6(3):197–204, 2016.

[70] Simon Hellerstein. Synthesis of all-pass delay equalizers. *IRE Transactions on Circuit Theory*, 8(3):215–222, 1961.

[71] P Keerthan, Ritesh Kumar, and KJ Vinoy. A novel all-pass network implementation for improved group delay performance. *IEEE Microwave and Wireless Components Letters*, 26(10):804–806, 2016.

[72] S. Kadambe, R. Murray, and G. F. Boudreaux-Bartels. Wavelet transform-based qrs complex detector. *IEEE Transactions on Biomedical Engineering*, 46(7):838–848, July 1999.

[73] N. V. Thakor, J. G. Webster, and W. J. Tompkins. Estimation of qrs complex power spectra for design of a qrs filter. *IEEE Transactions on Biomedical Engineering*, BME-31(11):702–706, Nov 1984.

[74] Satu Rajala, Teemu Ahmaniemi, Harri Lindholm, Kiti Müller, and Tapio Taipalus. A chair based ballistocardiogram time interval measurement with cardiovascular provocations. In *2018 40th Annual International Conference of the IEEE Engineering in Medicine and Biology Society (EMBC)*, pages 5685–5688. IEEE, 2018.

[75] B. Linares-Barranco and T. Serrano-Gotarredona. On the design and characterization of femtoampere current-mode circuits. *IEEE Journal of Solid-State Circuits*, 38(8):1353–1363, Aug 2003.

[76] J. M. Carrillo, J. F. Duque-Carrillo, and G. Torelli. 1-v continuously tunable cmos bulk-driven transconductor for gm-c filters. In *2008 IEEE International Symposium on Circuits and Systems*, pages 896–899, May 2008.

[77] E. Rodriguez-Villegas, A. Yufera, and A. Rueda. A 1.25-v micropower gm-c filter based on fgmos transistors operating in weak inversion. *IEEE Journal of Solid-State Circuits*, 39(1):100–111, Jan 2004.

[78] Z. Zhu and W. Bai. A 0.5-v 1.3- μW analog front-end cmos circuit. *IEEE Transactions on Circuits and Systems II: Express Briefs*, 63(6):523–527, June 2016.

[79] A. Arnaud, R. Fiorelli, and C. Galup-Montoro. Nanowatt, sub-ns otas, with sub-10-mv input offset, using series-parallel current mirrors. *IEEE Journal of Solid-State Circuits*, 41(9):2009–2018, Sep. 2006.

[80] A. Veeravalli, E. Sanchez-Sinencio, and J. Silva-Martinez. Transconductance amplifier structures with very small transconductances: a comparative design approach. *IEEE Journal of Solid-State Circuits*, 37(6):770–775, June 2002.

[81] C. Yehoshuva, R. Rakhi, D. Anto, and S. Kaurati. 0.5 v, ultra low power multi standard gm-c filter for biomedical applications. In *2016 IEEE International Conference on Recent Trends in Electronics, Information Communication Technology (RTEICT)*, pages 165–169, May 2016.

[82] S. Naik, S. Bale, T. R. Dessai, G. Kamat, and Vasantha M.H. 0.5v, 225nw, 100 hz low pass filter in 0.18µm cmos process. In *2015 IEEE International Advance Computing Conference (IACC)*, pages 590–593, June 2015.

[83] Saleha Bano, Ghous Bakhsh Narejo, and S. M. Usman Ali Shah. Low voltage low power single ended operational transconductance amplifier for low frequency applications. *Wireless Personal Communications*, 106(4):1875–1884, Jun 2019.

[84] F. Krummenacher and N. Joehl. A 4-mhz cmos continuous-time filter with on-chip automatic tuning. *IEEE Journal of Solid-State Circuits*, 23(3):750–758, June 1988.

[85] G. Fierro, A. Rodriguez, F. Olivera, P. Aguirre, and F. Silveira. Ultra low power automatic tuning for gm-c filters. In *2010 Argentine School of Micro-Nanoelectronics, Technology and Applications (EAMTA)*, pages 103–106, Oct 2010.

[86] Kenneth Laker and Willy Sansen. Design of analog integrated circuits and systems. page 847, 1994.

[87] G. Fierro, F. Silveira, and R. Armentano. Low group delay signal conditioning for wearable central blood pressure monitoring device. In *2017 39th Annual International Conference of the IEEE Engineering in Medicine and Biology Society (EMBC)*, pages 3285–3288, July 2017.

[88] Behzad Razavi. *Design of Analog CMOS Integrated Circuits*. 2000.

[89] C. S. Kim, A. M. Carek, O. Inan, R. Mukkamala, and J. O. Hahn. Ballistocardiogram-based approach to cuff-less blood pressure monitoring: Proof-of-concept and potential challenges. *IEEE Transactions on Biomedical Engineering*, PP(99):1–1, 2018.

[90] Vance W. Berger and YanYan Zhou. *Kolmogorov–Smirnov Test: Overview*. American Cancer Society, 2014.

[91] CJ Porth, VS Bamrah, FE Tristani, and JJ Smith. The valsalva maneuver: mechanisms and clinical implications. *Heart lung : the journal of critical care*, 13(5):507—518, September 1984.

[92] F Lemaître, F Bernier, I Petit, N Renard, B Gardette, and F Joulia. Heart rate responses during a breath-holding competition in well-trained divers. *International journal of sports medicine*, 26(06):409–413, 2005.

[93] Albinas Grunovas, Eugenijus Trinkunas, Alfonsas Buliuolis, Eurelija Venskaityte, Jonas Poderys, and Kristina Poderiene. Cardiovascular response to breath-holding explained by changes of the indices and their dynamic interactions. *Biological Systems: Open Access*, 5(1):1–8, 2016.

[94] J. Martin Bland and Douglas G. Altman. Statistical methods for assessing agreement between two methods of clinical measurement. *International Journal of Nursing Studies*, 47(8):931 – 936, 2010.

[95] W. Chen, T. Kobayashi, S. Ichikawa, Y. Takeuchi, and T. Togawa. Continuous estimation of systolic blood pressure using the pulse arrival time and intermittent calibration. *Medical and Biological Engineering and Computing*, 38(5):569–574, Sep 2000.

[96] J. Proença, J. Muehlsteff, X. Aubert, and P. Carvalho. Is pulse transit time a good indicator of blood pressure changes during short physical exercise in a young population? In *2010 Annual International Conference of the IEEE Engineering in Medicine and Biology*, pages 598–601, Aug 2010.

[97] Mico Yee-Man Wong, Carmen Chung-Yan Poon, and Yuan-Ting Zhang. An evaluation of the cuffless blood pressure estimation based on pulse transit time technique: a half year study on normotensive subjects. *Cardiovascular Engineering*, 9(1):32–38, 2009.

[98] Michela Mase, Walter Mattei, Roberta Cucino, Luca Faes, and Giandomenico Nollo. Feasibility of cuff-free measurement of systolic and diastolic arterial blood pressure. *Journal of electrocardiology*, 44(2):201–207, 2011.

[99] Xiaorong Ding, Yuanting Zhang, and Hon Ki Tsang. Impact of heart disease and calibration interval on accuracy of pulse transit time–based blood pressure estimation. *Physiological measurement*, 37(2):227, 2016.

[100] Qingxue Zhang, Dian Zhou, and Xuan Zeng. Highly wearable cuff-less blood pressure and heart rate monitoring with single-arm electrocardiogram and photoplethysmogram signals. *Biomedical engineering online*, 16(1):23, 2017.

[101] Federico S Cattivelli and Harinath Garudadri. Noninvasive cuffless estimation of blood pressure from pulse arrival time and heart rate with adaptive calibration. In *2009 Sixth international workshop on wearable and implantable body sensor networks*, pages 114–119. IEEE, 2009.

[102] Mozziyar Etemadi, Omer T Inan, Laurent Giovangrandi, and Gregory TA Kovacs. Rapid assessment of cardiac contractility on a home bathroom scale. *IEEE transactions on information technology in biomedicine*, 15(6):864–869, 2011.

[103] Ari Lindqvist, K Pihlajamäki, J Jalonen, V Laaksonen, and J Alihanka. Static-charge-sensitive bed ballistocardiography in cardiovascular monitoring. *Clinical Physiology*, 16(1):23–30, 1996.

[104] B. M. McCarthy, C. J. Vaughan, B. O'Flynn, A. Mathewson, and C. Ó Mathúna. An examination of calibration intervals required for accurately tracking blood pressure using pulse transit time algorithms. *Journal Of Human Hypertension*, 27:744 EP –, May 2013. Original Article.

[105] V. Burt B. Hamrell. *Cardiovascular Physiology: A Text and E-Resource for Active Learning.* Taylor Francis Group, 2018.

[106] A. Guyton J. Hall. *Textbook of Medical Physiology.* ELSEVIER, 2011.

[107] Michael F. O'Rourke Edward D. Frohlich Michel E. Safar. *Blood Pressure and Arterial Wall Mechanics in Cardiovascular Diseases.* Springer, 2014.

[108] Nico Westerhof, Jan-Willem Lankhaar, and Berend E. Westerhof. The arterial windkessel. *Medical & Biological Engineering & Computing*, 47(2):131–141, Feb 2009.

[109] Ahmed Qasem and Alberto Avolio. Determination of aortic pulse wave velocity from waveform decomposition of the central aortic pressure pulse. *Hypertension*, 51(2):188–195, 2008.

[110] O. T. Inan, P. Migeotte, K. Park, M. Etemadi, K. Tavakolian, R. Casanella, J. Zanetti, J. Tank, I. Funtova, G. K. Prisk, and M. Di Rienzo. Ballistocardiography and seismocardiography: A review of recent advances. *IEEE Journal of Biomedical and Health Informatics*, 19(4):1414–1427, July 2015.

[111] Ghufran Shafiq, Sivanagaraja Tatinati, Wei Tech Ang, and Kalyana C Veluvolu. Automatic identification of systolic time intervals in seismocardiogram. *Scientific reports*, 6:37524, 2016.

[112] Wiggers diagram at wikipedia. `https://en.wikipedia.org/wiki/Wiggers_diagram`.

[113] Hiroyuki Suga, Kiichi Sagawa, and Artin A. Shoukas. Load independence of the instantaneous pressure-volume ratio of the canine left ventricle and effects of epinephrine and heart rate on the ratio. *Circulation Research*, 32(3):314–322, 1973.

[114] N Stergiopulos, J J Meister, and N Westerhof. Determinants of stroke volume and systolic and diastolic aortic pressure. *The American Journal Of Physiology*, 270(6 Pt 2):H2050 – H2059, 1996.

[115] Belén Casas, Jonas Lantz, Federica Viola, Gunnar Cedersund, Ann F. Bolger, Carl-Johan Carlhäll, Matts Karlsson, and Tino Ebbers. Bridging the gap between measurements and modelling: a cardiovascular functional avatar. *Scientific Reports*, 7(1):6214, 2017.

[116] Sheikh Mohammad Shavik, Zhenxiang Jiang, Seungik Baek, and Lik Chuan Lee. High spatial resolution multi-organ finite element modeling of ventricular-arterial coupling. *Frontiers in physiology*, 9:119, 2018.

[117] Jeffrey G Kegel, Bennett D Schalet, William J Corin, and Abdulmassih S Iskandrian. Simplified method for calculating aortic valve resistance: Correlation with valve area and standard formula. *Catheterization and cardiovascular diagnosis*, 30(1):15–21, 1993.

This page was intentionally left blank.

List of Tables

List of Figures

This is the last page.
Thanks
`http://iie.fing.edu.uy/`